Politecnico di Milano

Dipartimento di Ingegneria Civile & Ambientale

Scuola di Ingegneria Civile, Ambientale e Territoriale

Master of Science Thesis

NUMERICAL INVESTIGATION OF TURBULENT FLOW IN PIPE BENDS

Supervisor:
Dr. Gianandrea Vittorio Messa

Dario Fumagalli 920645

Academic Year 2019-2020

Contents

List of Figures

Acknowledgements

Desidero ringraziare tutti coloro che in questi cinque anni di studi presso il Politecnico di Milano hanno contribuito a sostenermi nel non sempre facile percorso universitario.

Ringrazio Elena e Matteo i miei genitori, i quali hanno sempre creduto in me, ai quali riconosco tutti gli sforzi fatti per aiutarmi, quando in momenti molto intensi di studio hanno fatto l'impossibile per incoraggiarmi. Ricordo con molto affetto tutti i pranzi preparati la mattina presto da mia madre. Ringrazio le mie carissime pro Zia e Nonna che mi hanno ospitato numerose volte per un pranzo veloce tra le lezioni della mattina e del pomeriggio, e di tutto l'affetto che hanno sempre manifestato quando mi hanno ospitano a dormire a casa loro, per farmi guadagnare qualche ora di sonno in più. Ringrazio mia sorella Chiara che mi ha aiutato a lanciare le simulazioni sul suo computer per svolgere questa tesi nei tempi previstio.

Desidero ringraziare i miei amici Andrea e Lorenzo che sono sempre stati presenti anche quando il tempo per vedersi era molto poco. Ringrazio tutti i compagni di corso Laura, Marco, Martina, Chiara, Alessandro, Carlo, Luca, Giacomo, Alfonso, Ricardo, Francisco ed Elizabeth che hanno indimenticabilmente arricchito con la loro simpatia questi cinque anni. Ognuno di loro è stato gentilissimo ad aiutarmi nell'arduo percorso universitario. Insieme abbiamo imparato a lavorare sinergicamente nei progetti di gruppo valorizzando e condividendo le competenze di ciascuno, così come abbiamo collaborato a preparare gli esami. Ho ricevuto molto aiuto e vi ringrazio tantissimo, avete tutti contribuito in parte al mio successo.

Desidero ringraziare tutti gli altri amici con i quali ho trascorso pochi, ma piacevoli momenti di svago dall'intenso impegno universitario. Grazie a Massimo, Federico, Carlo, Silvia, Giulian e Daniele.

In ultimo, ringrazio i miei Professori del Liceo, i quali con molta pro-

fessionalità e affetto mi hanno fornito delle ottime basi per poter agevolmente studiare Ingegneria. Grazie Professoressa Zamarioli, con la quale ho migliorato tantissimo il mio inglese. Grazie Professoresse Calvano e Comperini che mi hanno trasmesso la passione per lo studio della fisica e della matematica. Grazie alla Professoressa Benevento per avermi fornito tutte le nozioni riguardanti la chimica e biologia che sono state utilissime. Altrettanto ringrazio il Professor Alberghina che mi ha fatto apprezzare molto la programmazione e le nozioni di informatica che si sono rivelate essere molto di aiuto.

Introduction

Pipe bends are present in a wide variety of engineering systems, ranging from the piping systems of industrial plants and heat exchangers to biological systems relying on transportation of gases and liquids in "pipe-like" veins, arteries, and capillaries, such as the respiratory and cardiovascular systems in mammals. In each of the aforementioned cases, some parts of the piping system are curved, either to adapt to the geometry, due to the technical constraints of the system, or to redirect the flow.

The turbulent flow inside a pipe bend is extremely complex. As reported in the review paper by Kalpakli Vester et al. [5], *curved pipes are commonly associated with strong secondary flow* (Fig.1) *and increased pressure losses that are due to an instability set up by the centrifugal forces acting on the fluid as it passes through the bend.* The complexity of the physical phenomenon has an obvious impact to model it using Computational Fluid Dynamic models based on the Reynolds-Averaging Navier-Stokes (RANS) approach.

Objective of this M.Sc. thesis is to assess the capability of RANS models based on the eddy-viscosity assumption to predict the essential features of turbulent flows in pipe bends. Compared with alternative approaches, these models are perhaps the most simplistic, but they do have the clear advantage of formal simplicity and low computational cost. For these reasons, they particularly attractive for engineering simulations. Understanding which type of information (and with which degree of accuracy) can be obtained using eddy-viscosity models is an essential step before looking at even more complex physical phenomena that can occur inside of these geometries, such as the transport of solids and the structural damage due to interactions between the travelling particles and the pipe walls. The thesis is divided in four chapters, followed by the conclusions.

The first chapter starts with the identification of the relevant geometrical and fluid dynamic parameters governing the turbulent flow inside a pipe bend. Afterwards, the reasons why the secondary flow occurs are explained, and the pressure field in the bend is explained. Finally, a review of the previous experimental investigations concerning turbulent pipe bend flows is

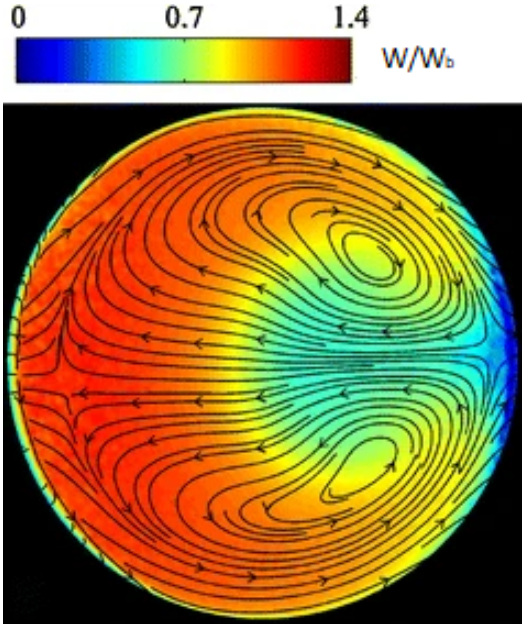

Figure 1: Color plot of local streamwise velocity W, normalized by the bulk velocity W_b and iso-lines of secondary flows inside a pipe bend (From [4])

carried out, focusing the attention on those concerning bends with either 90° or 180° angles.

The second chapter focuses on Computational Fluid Dynamics (CFD) as an approach to investigate turbulent pipe bend flows. Starting from the instantaneous Navier-Stokes equations for incompressible flows of Newtonian fluids, the Reynolds Averaged Navier-Stokes equations (RANS) are obtained. In order to be solved, the RANS must be coupled with other equations that model the Reynolds stresses tensor: here the attention was focused on five turbulence models based on the eddy viscosity assumption of Boussinesq (standard $k-\varepsilon$, RNG $k-\varepsilon$, Relizable $k-\varepsilon$, $k-\omega$, and SST $k-\omega$). Then, the methodological procedure and the best practices in CFD are reported, analyzing the key aspects of the pre-processing, processing and post-processing phases of a CFD simulation. At the end of the chapter, the-state-of-the-art review of relevant numerical investigations of pipe bend flows using RANS-based models is presented.

The third chapter focuses on the simulation of the experimental tests carried out by Sudo et al. [9] regarind the flow of air in a 180° bend. The numerical simulations, carried out with the PHOENICS 2018 code, were initially run using the standard $k-\varepsilon$ turbulence model. After a brief introduction on the PHOENICS code, analyses were made to ensure that the flow is fully developed at the entrance of the bend, in compliance with the experimental

conditions, and to demonstrate the convergence and grid-independence of the solution. The numerical results of pressure, velocity, turbulence intensity and secondary flow intensity are compared with the experimental results. Finally, a sensitivity analyses was made to assess the influence of the turbulence model (standard $k-\varepsilon$, RNG $k-\varepsilon$, Relizable $k-\varepsilon$, $k-\omega$, and SST $k-\omega$), and select the one which procures the best agreement with the experiments, which was found to be RNG $k-\varepsilon$.

In the fourth chapter, the validation was extended to two other cases, both referring to a 90° bend, whose correspondent experimental results were reported in the first chapter (Enayet et al. [3] and Sudo et al. [8]). On the grounds of the achievements of the third chapter, the simulations are carried out with the RNG $K-\varepsilon$ turbulence model. The numerical predictions of the mean velocity, mean pressure, and turbulence variables are qualitatively compared with the measurements available.

Chapter 1

Fluid dynamic behaviour of turbulent pipe bend flows and previous experimental investigations

1.1 Significant parameters of pipe bend flows

The geometry of a circular pipe bend is defined by the following parameters, depicted in Fig. 1.1. Firstly, the diameter of the pipe, denoted as D , or, alternatively, its radius $R = D/2$. Secondly, the curvature radius, Rc, defined as the distance from the center of curvature to the center-line of the pipe is the radius of the bend. Thirdly, the angle of the curve denoted by Φ individuates the comprehensive extent of the bend. Frequently, R and Rc are combined into the dimensionless curvature ratio $\gamma = R/R_c$, which is within the limits $0 \leq \gamma \leq 1$, where, for a straight pipe, $\gamma = 0$, and, for a sharp bend, $\gamma = 1$. Let's now discuss the fluid dynamic parameters characterizing a pipe bend flow. An incompressible, isothermal flow field is represented by a vector velocity field and a scalar pressure field, both function of three spatial coordinates and one time coordinate. The components of the velocity vector, $\vec{v}$, along the three spatial directions are here referred to as u, v, and w, respectively. In the case of turbulent flows, a widely used approach consists in expressing u, v, w as the sum of their Reynolds averages (U, V, W), which are function of space only, and the fluctuations u', v', w', function of time and space. The same for the pressure p that can be measured as the sum of the Reynolds average P and the fluctuating component p' so $p = P + p'$. This will be further explained in paragraph 2.1.2.

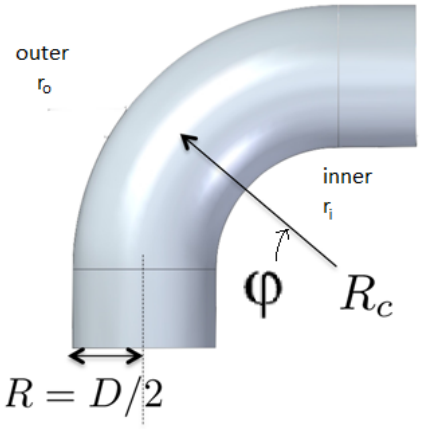

Figure 1.1: Geometrical Features: curvature radius R_c, pipe radius R, pipe diemeter D. Reference to the inner side of the bend r_i and the outer side r_o

An other variable used when using isotropic turbulence models is the *Root mean square velocity* defined as $uRMS = 1/3(u'^2 + v'^2 + w'^2)^{1/2}$.

In the Cartesian reference system, the space points and the velocity components are defined along three fixed perpendicular axes x, y and z (Fig. 1.2a); it is frequently unsuitable to describe the flow in a bend pipe with such a reference system. In fact, when examining the variable of interest alongside the pipe curvilinear abscissa the cylindrical or the toroidal coordinate systems best individuate the points of the domain. A more suitable refer-

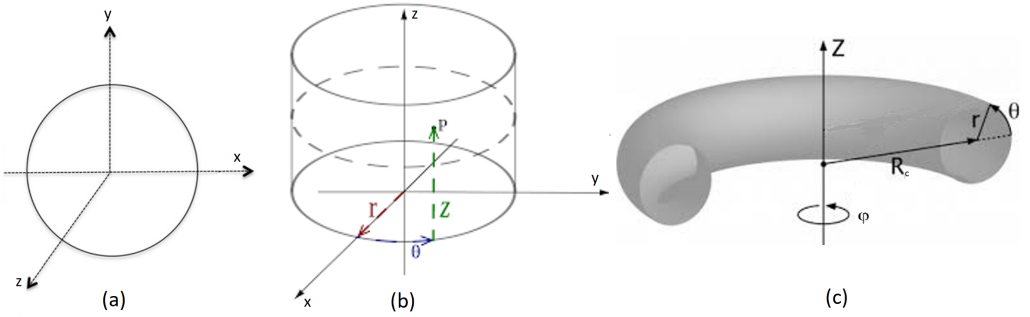

Figure 1.2: Reference systems employed: "a" Cartesian reference system; "b" Cylindrical-polar reference system; "c" Toroidal reference system.

ence system for dealing with straight pipes with circular cross-section is the cylindrical-polar one (Fig. 1.2b), where r represent the radial coordinate, θ the azimuthal coordinate, and z is the axial coordinate. Finally, an effective reference system for circular pipe bends is the toroidal one, which is like a cylindrical-polar system in which the axial coordinate z is replaced by the

angle φ (Fig. 1.2c)

All pipes object of the study consist in initial and final straight segments or tangents that forerun and follow the bend (Fig. 3.10). For this reason it's necessary to use an hybrid reference system that in the straight part of the duct employs a cylindric-polar coordinates and in the bend toroidal ones. This hybrid reference system is used for the numerical analysis on the software PHOENICS and is denominated "Body-fitted", exactly as the name suggests it fits to the local geometry of the physical domain. Note that, from this point onward, $u = U + u'$, $v = V + v'$, and $w = W + w'$ will denote the velocity components along the three spatial directions identified by the coordinate system used. Therefore, depending on the reference system in each context, the meaning of each velocity component will be clear.

Two dimensionless scalar parameters are introduced to characterize the fluid dynamic behaviour of a pipe bend flow. The former, used to distinguish the flow regime (laminar, transitional, turbulent) is the bulk Reynolds number, defined as:

$$\mathrm{Re} = \rho W_b D/\mu \tag{1.1}$$

where ρ is the fluid density, W_b is the bulk velocity, and μ is the dynamic viscosity of the fluid. The latter, relevant in the laminar flow regime only, is the Dean number, which takes into account the effects of both the Reynolds number and the curvature.

$$\mathrm{De} = \sqrt{\gamma}\mathrm{Re} \tag{1.2}$$

Moving on to the parameters associated with pressure, a dimensionless variable frequently encountered in the literature is the pressure coefficient, defined as

$$C_p = \frac{p - p_{\mathrm{ref}}}{\rho W_b^2/2} \tag{1.3}$$

where p_{ref} is the reference pressure chosen in a specific point of the domain. Any time the C_p is calculated an arbitrary choice of p_{ref} can be made according to the availability of the pressure data or the convenience.

A parameter used to asses the magnitude of secondary flow presence in a section is I_s. This adimensional parameter sums the squares of the cross-section velocities U and V so that to take into account only the magnitude of the secondary flow and not the direction since the squares are always positive. This sum is normalized by the half area of the section in which

the computation is carried out and the square of the bulk velocity W_b. The mathematical expression of I_s is shown below:

$$I_s = \frac{8}{\pi D^2 W_b^2} \int_{-\pi/2}^{\pi/2} \int_0^R \left(U^2 + V^2\right) r \mathrm{d}r\mathrm{d}\theta \tag{1.4}$$

A parameter extremely useful for the assessment of the turbulence intensity in a whole half section of the pipe is k_a. This adimensional parameter sums the squares of the three Reynolds' stresses $\rho u'^2$ $\rho v'^2$ $\rho w'^2$. This sum is normalized by the half area of the section in which the computation is carried out and the square of the bulk velocity W_b and the ρ. The mathematical expression of k_a is shown below:

$$k_a = \frac{8}{\pi D^2 W_b^2} \int_{-\pi/2}^{\pi/2} \int_0^R \frac{1}{2}(u'^2 + v'^2 + w'^2) r \mathrm{d}r\mathrm{d}\theta \tag{1.5}$$

1.2 Features of turbulent flows in pipe bends

1.2.1 Secondary flow patterns

In some fluid dynamic processes, it is possible to identify a relatively minor flow which is superimposed on the primary flow. Such "minor flow" is called "secondary flow". Generally, it is easy to distinguish the primary and the secondary flows, since the former is predicted using simple analytical techniques and represent closely the macroscopic flow pattern, whereas the latter is of lower magnitude of velocities and has different direction from the principal flow.

The secondary flow occurring inside a pipe bend is of interest in the present thesis. In any curved pipe, the centrifugal force acting on the fluid elements is only partially balanced by a lateral pressure gradient. As a result, a mass flux generates in the central part of the cross-section, which, owing to the mass conservation principle, is balanced by a flux in the opposite direction close to the lateral walls of the cross section. These transverse movement is the secondary flow superposed to the primary one. Such behaviour is observed in either laminar of turbulent flow conditions.

A lot of theoretical work concerns the case of fully-developed flow inside a pipe bend with infinite length, which, for instance, occurs inside a helicoidal pipe of infinite length 1.3. In this situation, the flow is the same for any cross section, and there is no dependence upon the streamwise coordinate.

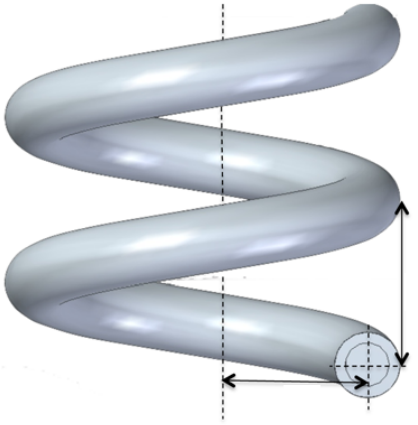

Figure 1.3: Helix

In his pioneering study, Dean demonstrated analytically that, in the case of fully-developed laminar flow in a pipe bend, the secondary flow pattern consists of two counter-rotating vortexes, and the flow in the center plane is directed to the outer wall. Things are more complex in the case of interest in this thesis, that is, a pipe bend with finite angular extension (e.g., 90° or 180°) installed between two straight pipes. In this case, the flow is developing inside the bend and downstream of it and, therefore, the primary and secondary flow patterns will vary along the streamwise direction. Even the direction of the secondary flow might change inside the bend and downstream of it. The example reported in Paragraph 1.3.7 will go into details of the secondary flow occurring in a $\Phi = 90°$ bend.

1.2.2 Pressure field inside a pipe bend

Figure 1.4, allows assessing the topology of the pressure field inside a 90° bend installed between two straight pipes. As already mentioned, a radial pressure gradient occurs, with a raise of pressure towards the outer side, r_o, and a decrease on the opposite side, r_i. Since the radial pressure gradient does not fully balance the centrifugal force, secondary flow occurs. As a result, an abrupt drop of pressure occurs along the streamwise direction. Studies demonstrate that the localized pressure loss is to be considered coupled to the appearance of the secondary flow. Such abrupt pressure drop, in fact, represents a concentrated loss of energy, which is consumed by the secondary flow itself.

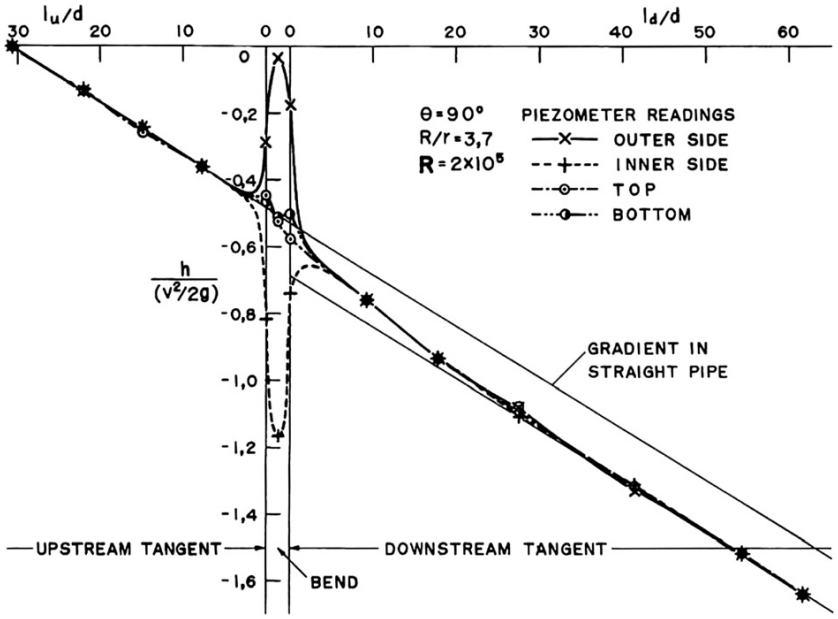

Figure 1.4: Pressure distribution along pipeline containing a $\Phi = 90°$ bend $\gamma = 0.27$, where lu and ld denote the pipe lengths upstream and downstream the bend, respectively adimentionalized with the diameter d. The Reynolds number is here denoted as $\mathbf{R}$, whereas R is the curvature radius and r is the pipe radius. By Vester et al. [5]

1.2.3 Notes on the laminar-turbulent transition

The presence of a curvature in a pipe does not only influence the distribution of pressure, as explained, in the previous paragraph but it can also have in impact on the flow regime. Although the present thesis focuses on turbulent flows only, for the sake of completeness, essential information on laminar and transitional pipe bend flows will be provided.

Several studies were made to investigate the flow regime inside helicoidal pipes of considerable length, thus capable to produce fully-developed bend flow. In this condition, a constant streamwise pressure gradient occurs and, therefore, a bend friction factor can be defined in analogy to straight pipe flows. Many authors used bend friction factor- bulk Reynolds number diagrams to state whether a fully-developed bend flow is laminar or turbulent. There is evidence that secondary flow increases flow resistance in a bend pipe. This was argued as the reason why the onset of turbulence in curved pipes takes place at a higher Reynolds number compared to straight pipes. In fact, is was estimated [5] that the critical Reynolds number for a curved tube could double when compared to the one for a straight pipe (which is typically equal to $Re^* = 2000$).

Sreenivasan and Strykowski , mentioned in the paper of Vester et al.

[5], performed a test using a coiled pipe and were able to observe how the turbulent flow entering from a straight into the curved pipe became laminar and then was turning back to its turbulent state after exiting the coil, see Fig. 1.5. The authors also noticed that the transition from laminar towards turbulent state is smother in curved pipes in regards to the abrupt change taking place in straight pipes.

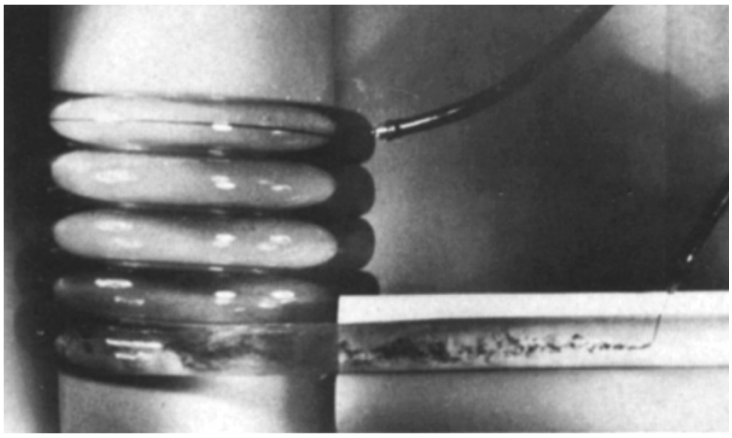

Figure 1.5: Laminarization in coiled pipes. By Vester et al. [5]

1.3 Review of previous experimental studies on turbulent pipe bend flows

This paragraph aims at summarizing the experimental works found in the literature regarding turbulent flows in bends of finite length installed between straight pipes. The experimental setups differ in terms of pipe diameter, curvature radius (hence, curvature ratio, γ), bend angle, inlet bulk-mean velocity, lengths of upstream and dowstream pipes, kind of fluid used for experiments such as air or water sometimes with solid particles. Attention was restricted to the researchers in which velocity measurements were provided. This was achieved by employing techniques such as Laser Doppler velocimetry LDV, hot-wire anemometer, or simply, Pitot tubes. In some cases, pressure measurements were also provided, as obtained using pressure taps installed at some locations over the bend walls. The experiments are summarized in Table 1.1. In the first column are cited the authors that performed the experiments. In the second it's indicated the Raynolds number, the third column presents the curvature ratio γ the fourth column presents the extent of the bend Φ, the fifth column presents the length of the in-

let tangent of the pipe in units of diameters, the sixth column presents the length of the downstream tangent of the pipe in unites of diameter, the seventh column describes whether the flow in the inlet tangent reaches the fully developed state "Fully Developed" (F. D.) "Developing" (D.), and the last column presents some of the measured quantities by the authors. The symbol P_{tot} stands for the total pressure. represent the static pressure,

Author and year	Re [-]	γ [-]	Φ[°]	I	E	I. C.	Quantities
Adler 1934 [5]	2-12·10^3	0.01 0.02	90				W
Rowe 1970 [5]	2.4·10^5	0.042	180	69D		F. D.	P_{tot}
Enayet 1982 [3]	4.3·10^4	0.17	90	5D	10D	D.	W, w', P_{tot}
Azzola 1986 [5]	5.7-11·10^4	0.15	180	54.7D	54.7D	F.D.	W, V, w',v'
Anwer 1989 [5]	5·10^4	0.077	180	96D	96D	F.D.	W,U,V w',u',v'
Al Rafai 1990 [11]	3,4·10^4	0.07 0.14	90	24D 69D	69D 7D	F.D.	W,U, w'
Sudo 1998 [8]	6·10^4	0.25	90	100D	40D	F.D.	W,U,V w',u',v' P_{tot}
Sudo 2000 [9]	6·10^4	0.25	180	100D	40D	F.D.	W,U,V w',u',v' P_{tot}

Table 1.1: Summary of main experiments

The experimental studies listed in Table 1.1 will be now described with more details.

1.3.1 Adler [5]

The very first study on turbulent flow in curved pipes was carried out by Adler, who measured the locally-averaged streamwise velocity for bulk Reynolds numbers in the range $Re = 2 - 12 \cdot 10^3$. The author was already able to infer the existence of secondary flow in the bend, since he noticed that the streamwise velocity becomes higher close to the inner wall at an angle $\varphi = 30°$ downstream the bend inlet section, in correspondence of the formation of the cross-sectional vortexes.

1.3.2 Rowe (from [5])

The author used Pitot tubes to measure the total pressure P_{tot} in a 180° pipe bend with curvature ratio $\gamma = 0.042$. The flow was in the turbulent regime with $Re = 2.4 \cdot 10^5$. The flow entering the bend was assessed to be fully developed. This study agrees with the findings of Sudo et al. in regard to the first appearance of the secondary motion that becomes strong enough to be well detectable at $\varphi = 30°$. According to the experimenter,

the secondary flow weakens until reaching a constant value at $\varphi = 90°$, and velocity distribution pattern does not significantly change from $\varphi = 90°$ until $\varphi = 180°$. As a result, he claimed that the secondary flow motion has a fully developed state starting from a $\varphi = 90°$. The author also noticed that, after 61D downstream the curved pipe, the flow was not recovered by the influence of the bend.

1.3.3 Enayet et al. [3]

Enayet et al. studied the turbulent flow in a Φ =90° bend with curvature ratio $\gamma = 0.17$, this case will be of interest in the paragraph 4.2 when numerical results are compared with experimental one. The test was carried out with water with a bulk velocity $W_b = 0.92$m/s corresponding to a bulk Reynolds number of $Re = 4.3 \cdot 10^4$. Velocity measurement were carried out with LDV for three $\varphi = 30°, 60°, 75°$ and two sections downstream the bend, as shown in Fig. 1.7.

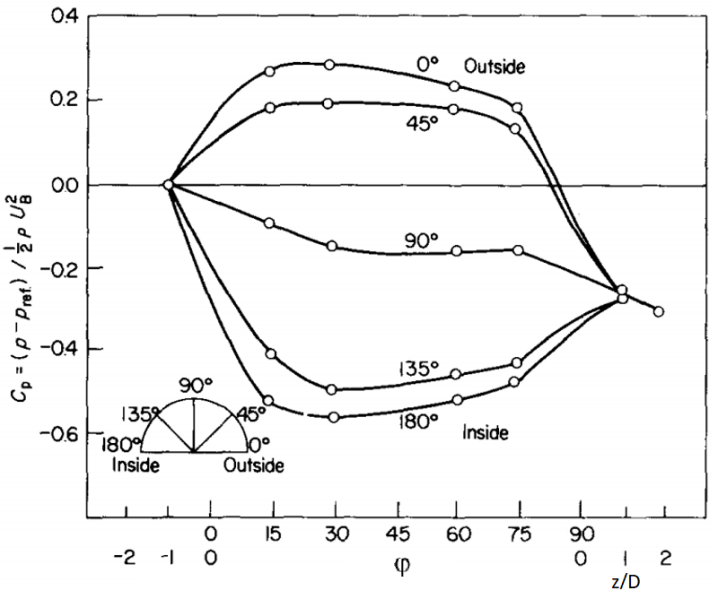

Figure 1.6: Wall static pressure measured by Enayet et al. [3]

Measurements of the wall static pressure variation were carried out throughout the bend, not surprisingly, the authors found a negative streamwise pressure gradient at r_o and a positive streamwise pressure gradient at r_i as visible in Fig. 1.6. They also estimated that the negative gradient in the r_i position is twice bigger than the negative one at ($\varphi = 15°$). The streamwise pressure

gradients then becomes very small (in absolute term) up to $\varphi = 75°$ and, afterwards, the modifications to the pressure field induced by the bend start is to disappear.

Concerning the velocity, at $\varphi = 30°$, the longitudinal component reaches its pick close the inner wall r_i (Fig. 1.7a). Conversely, at $\varphi = 90°$ section the highest velocity is shifted toward the outer wall (Fig. 1.7e) this shift is operated by the secondary flow present in the bend.

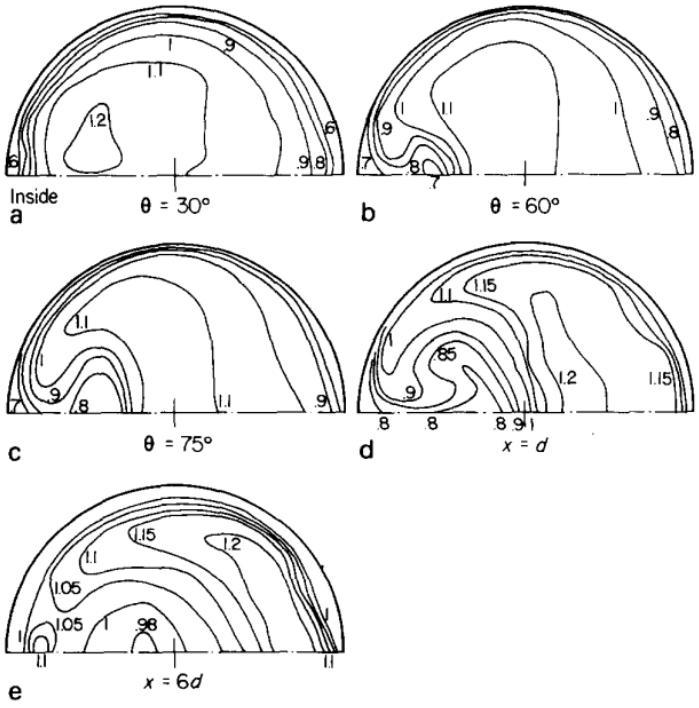

Figure 1.7: (a-c) Contours of mean velocity W/W_b in the bend.
(d-e) Contours of mean velocity W/W_b downstream the bend at z=D and z=6D, where "z" longitudinal coordinate is called "x" by Enayet et al. [3]

1.3.4 Azzola et al. [1]

Azzola et al. [1] performed experiments on a $\Phi = 180°$ bend with $\gamma = 0.15$ over a range of Reynolds number $Re = 5.7 - 11 \cdot 10^4$. They used water at 20°C for the experiment with a bulk velocity of approximately $W_b = 1.29$m/s. The authors measured, using LDV, the longitudinal and circumferential velocity components W w' V v' expressed them in a toroidal reference system. The author provided a comprehensive evolution of the flow in the bend displaying secondary flow in cross-section's plane using vectors and contour plots of

the normalized longitudinal velocity W/W_b, these results are reported for 6 different sections in Fig.1.8. The authors also investigated the phenomenon with the aid of numerical simulations choosing as the turbulence model the standard $k - \varepsilon$ model. Their results were somewhat acceptable, there was agreement between numerical and experimental data (Fig.s 2.2 and 2.3) . This will be further discussed in paragraph 2.3.

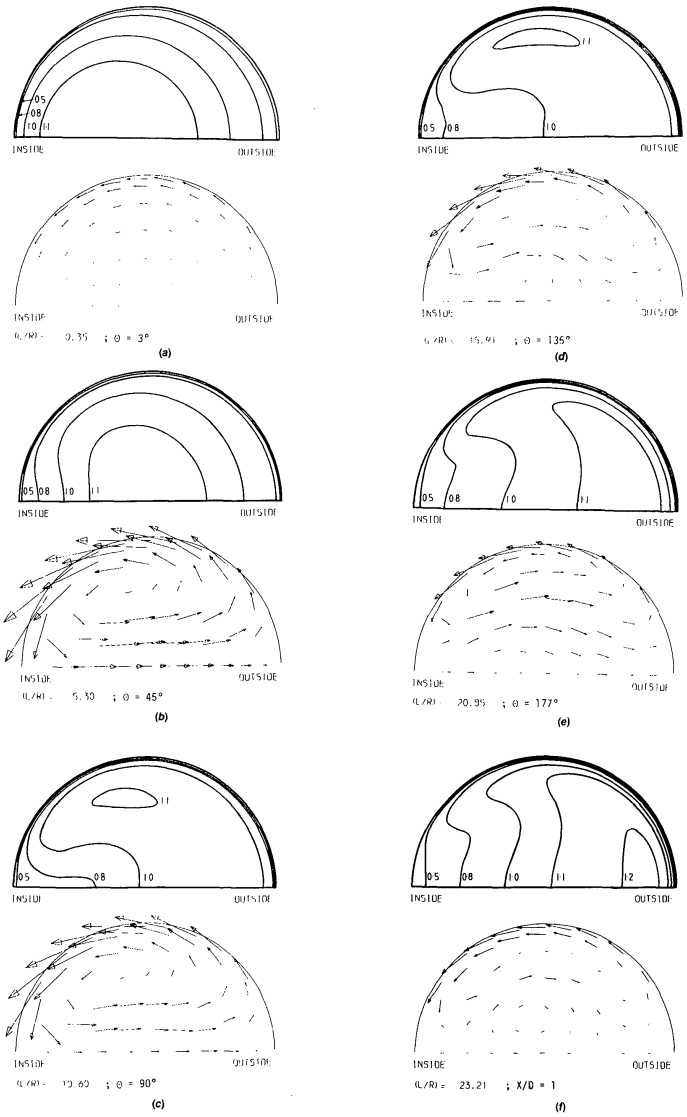

Figure 1.8: Experimental results of normalized longitudinal velocity W/W_b on the top and in plane vector velocities on the bottom for sections: "a" $\varphi = 3°$; "b" $\varphi = 45°$; "c" $\varphi = 90°$; "d" $\varphi = 135°$; "e" $\varphi = 177°$; "f" $z/D = 1$. (From Azzola et al. [1])

1.3.5 Anwer et al. (from [5])

Anwer et al. and Anwer and So. performed experimentson a case with $\Phi = 180°$ with $Re = 5 \cdot 10^4$ and $\gamma = 0.077$ and they estimated the locally averaged velocity components and Reynolds stresses employing a hot-wire and wall-static pressure devices. Their purpose was to detect the influence that the bend has on the flow upstream and downstream the bend. The measurements where performed at several streamwise locations upstream and downstream the bend in the locations (z/D= -18; -1; 1; 6; 10; 18; 30; and 49) where the negative and positive signs have the exact same meaning used in paragraph 1.3.7 and individuates upstream sections. They observed that 18D upstream the bend the flow was fully developed. Whereas 1D upstream the bend the streamwise velocity stops being axial-symmetric so the flow quit being fully developed, this due to the influence of the bend's presence. Complementary, the authors found that 18D downstream the bend the flow hasn't recovered to the fully developed state yet.

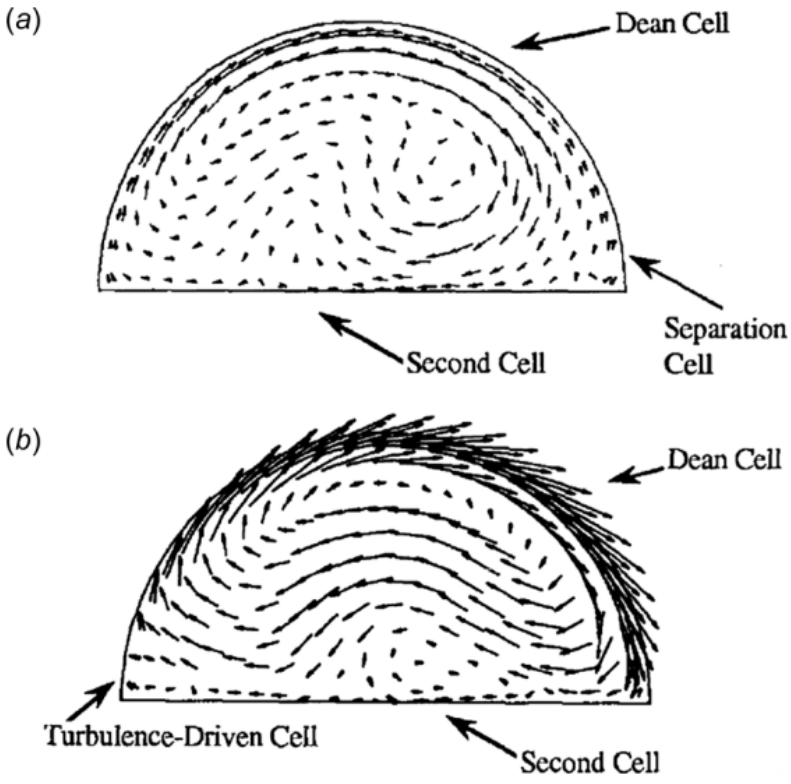

Figure 1.9: Turbulent cell in the bend pipe

The authors also performed a numerical simulations employing the $k - \varepsilon$

standard turbulence model and they found a different secondary flow pattern that starts to take place about between $\varphi = 67°$ and $\varphi = 112°$. They speculated the existence of a additional cell other than the usual Dean-like vortexes. The small cell visible in Fig. 1.9 has a limited existence approximately in half bend pipe, in fact, its presence decays 1D downstream the curvature.

1.3.6 Al Rafai et al.[11]

Al-Rafai et al. investigated the turbulent flow through curved pipes $\Phi = 90°$ injecting air in the pipe with a bulk velocity W_b =11.616 m/s. The pipe has a $D = 43$mm, two bends, a first straight tangent of 1.04m followed by the first curve with $R_c = 0.58$m, then a straight tangent of 3m afterward a second bend of $\Phi = 90°$ with a $R_c = 0.29$m and a downstream straight tangent of 0.3 m as in Fig. 1.10

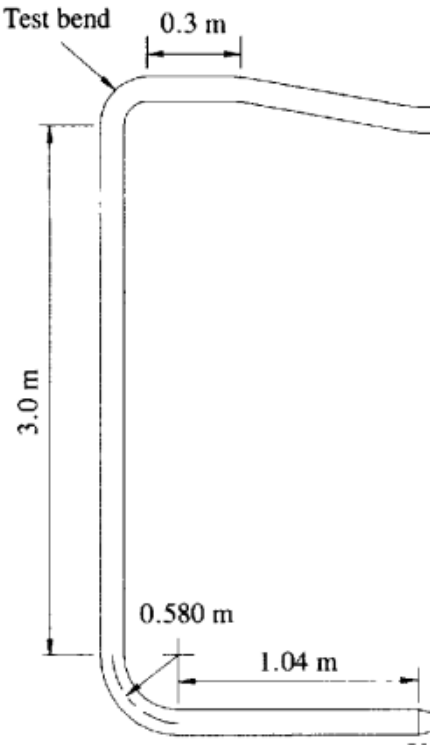

Figure 1.10: Configuration of the experimental simulation cunducted by Al Rafai et al.[11]

The experiment was carried out with a $Re = 3.4 \cdot 10^4$ and γ equal to either 0.07 and 0.14. The authors employed a LDV to perform the measurements

of $uRMS$, U, V, W. They measured these quantities at cross-stream section alongside the bend in seven position: $\varphi = 0°,\ 15°,\ 30°,\ 45°,\ 60°,\ 75°,\ 90°$. Some of the measurements performed in the two bends of the $uRMS/W_b$ are displayed in Fig. 1.11.

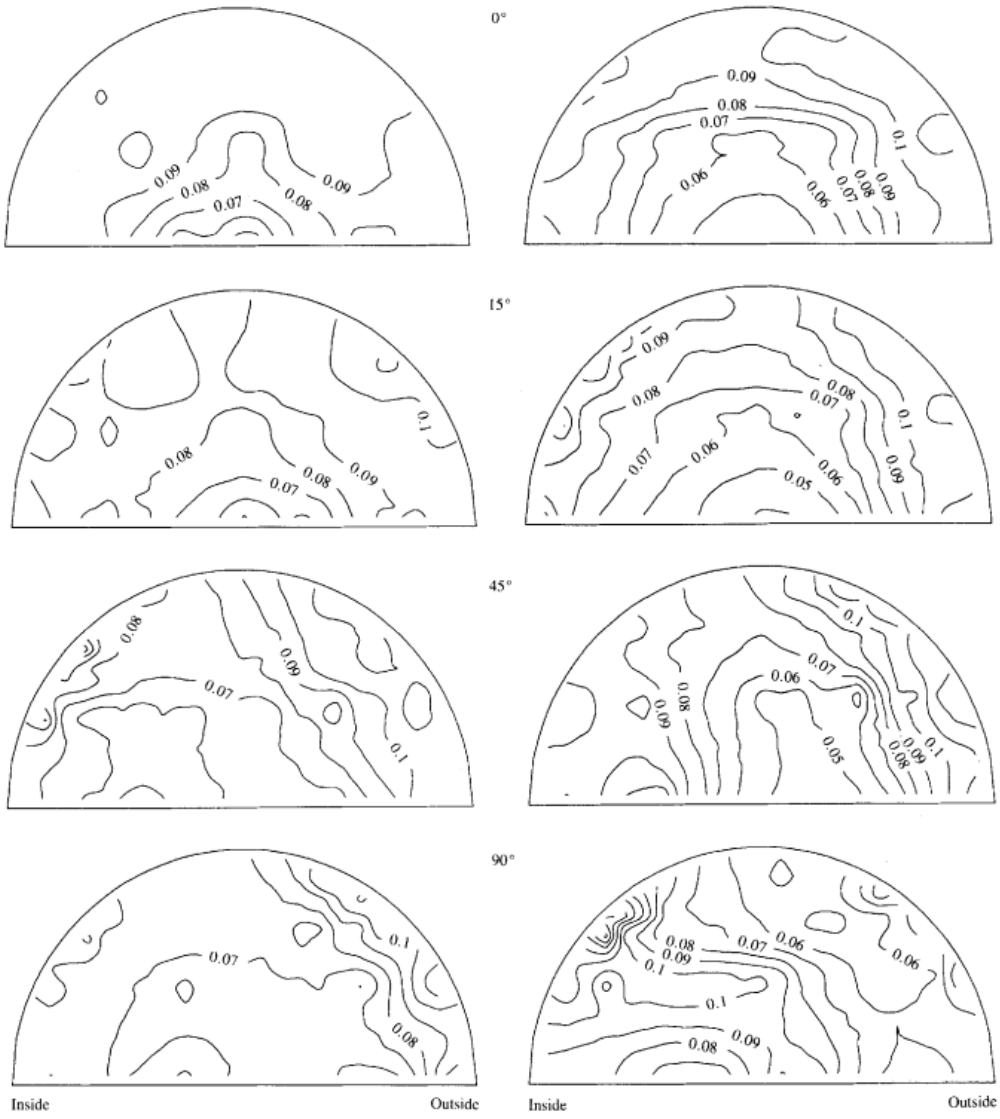

Figure 1.11: Contour lines of the normalised $uRMS/W_b$ for the first bend with $R_c = 0.58$m (left) and the second bend with $R_c = 0.29$m (right) for $\varphi = 0°,\ 15°,\ 45°,\ 90°$ by Al Rafai et al.[11]

1.3.7 Sudo et al. $\Phi = 90°$ [8]

Sudo and co-workers conducted experiments to investigate the secondary flow phenomenon in a $\Phi = 90°$ bent pipe. Their experimental apparatus is shown schematically in Fig. 1.12. The authors claimed that the formation

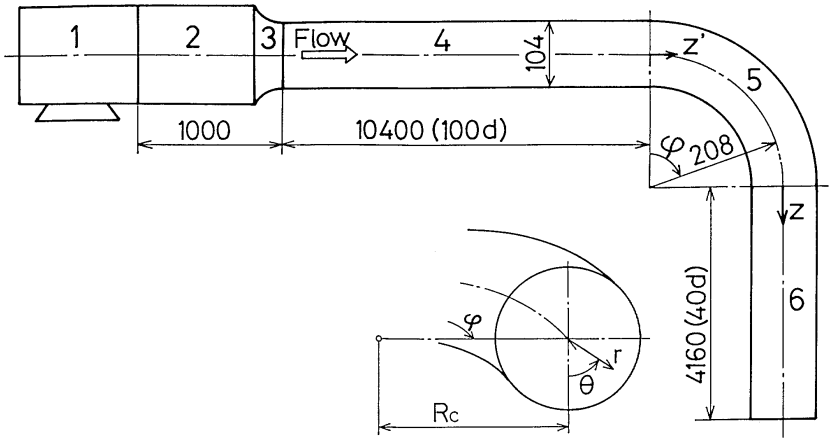

Figure 1.12: Schematic diagram of test pipe and coordinate system. 1) Fan; 2) settling chamber; 3) contraction; 4) upstream tangent; 5) $\Phi = 90°$; 6) downstream tangent; Note that Sudo et al. [8] uses the letter "d" to individuate the diameter of the pipe generally denoted ad D.

of secondary flow requires the angle of the bend to be larger than $\varphi = 30°$. As already reported in Table 1.1, the curvature radius is $R_c = 208$ mm, the upstream and downstream straight segments of the pipe are respectively of 10.4m (100 pipe diameters, enough to ensure fully-developed flow) and 4.16 m (40 pipe diameters). A settling chamber was used for stabilizing the air flux, and it was followed by a contraction that brings the section to an inner diameter $D = 2R = 104$ mm (note that Sudo et al. [8] refer to the diameter with the letter "d" instead of "D"). The curvature ratio of the bend is therefore $\gamma = 0.25$. The experiment is performed with air with bulk mean velocity $W_b = 8.7$ m/s, resulting in $Re = 60000$, which indicates a turbulent flow regime. The coordinate system used by the experimenters to identify the measurement points was combined cylindrical-polar (for the straight pipes) and toroidal (for the bend). The streamwise coordinate was identified by the negative distance from the bend inlet section in the upstream pipe, called z', the angle φ inside the bend, and the positive distance from the bend outlet section in the downstream pipe, called z. Preliminary measurements were obtained at $\varphi = 60°$ in the bend, as well as at $z/D = -1$ and $z/D = 5$ in the upstream and downstream tangents, to evaluate the symmetry of the flow. These measurements have confirmed that the flow is perfectly

symmetric. This will be exploited in the numerical simulations, as it will be discussed in Chapter 3. Hence, the velocity measurements were collected over half of the cross section of the pipe, according to the grid shown in Fig. 1.13. Additionally, a nonuniform grid size is used to better detect the flow behaviour close to the wall. In fact, Δr is small near the wall and gradually larger elsewhere.

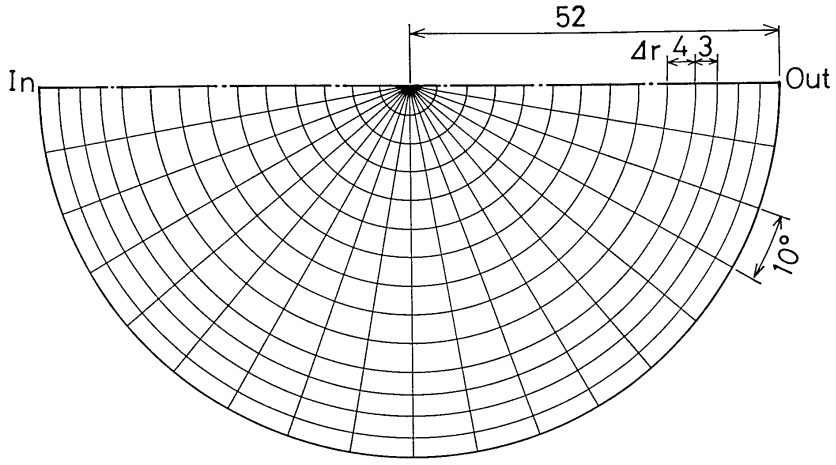

Figure 1.13: Half Mesh Grid. (From Sudo et al. [8])

Pressure and velocity data were provided for different sections upstream, inside, and downstream the bend.

In Fig. 1.14, the wall static pressure at various axial locations is plotted as a function of the coordinates z'/D upstream the bend, φ inside the bend, and z/D downstream of the bend. In the vertical axis, reference was made to the pressure coefficient C_p. defined in Eq. (1.3).

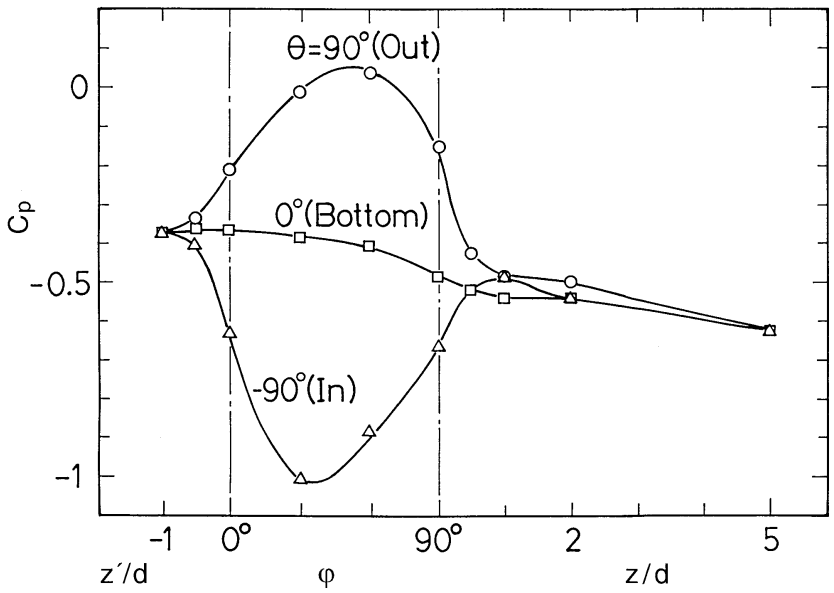

Figure 1.14: Longitudinal distribution of wall static pressure. (From Sudo et al. [8])

Isotach lines of the longitudinal mean velocity and secondary flow patterns are reported in Fig. 1.15 for several section, individuated, once again, by the longitudinal coordinates z'/D, φ, and z/D. Note that, since the flow is symmetrical, what happens in the lower section happens specularly in the upper one too.

At $z'/D = -1$, the flow doesn't perceive the presence of the bend, as confirmed by the fact that the contours are concentric circles and the flow remains fully developed. At the inlet plane of the bend, $\varphi = 0°$, near the inner wall the fluid is slightly accelerating due to the initially favourable longitudinal pressure gradient in that region (Fig. 1.14). On the other hand, the fluid close to r_o is decelerated according to the initially unfavourable pressure gradient. This is the context where the secondary flow takes place. In fact, the pressure distribution induces a weak secondary flow from r_o towards r_i in the whole cross section. At $\varphi = 30°$, the secondary flow makes its first clear appearance thanks to the action of the centrifugal force that compresses the fluid in the r_o region of the cross section. The set up of two counter-rotating vortexes with an outward circulation might be perceived in Fig. 1.15c, and it appears similar to the pattern already shown in Fig. 1. At $\varphi = 60°$ (Fig. 1.15d), the faster fluid initially near the inner region r_i is shifted by the secondary flow towards the outer wall r_o. Similarly, the slower fluid that was initially in the r_o part is conveyed towards the inner wall side r_i by means of the secondary flow. Simultaneously, the pressure starts raising close the inner wall in the longitudinal direction (Fig. 1.14) and, thus, the

fluid near the inner wall starts decelerating.

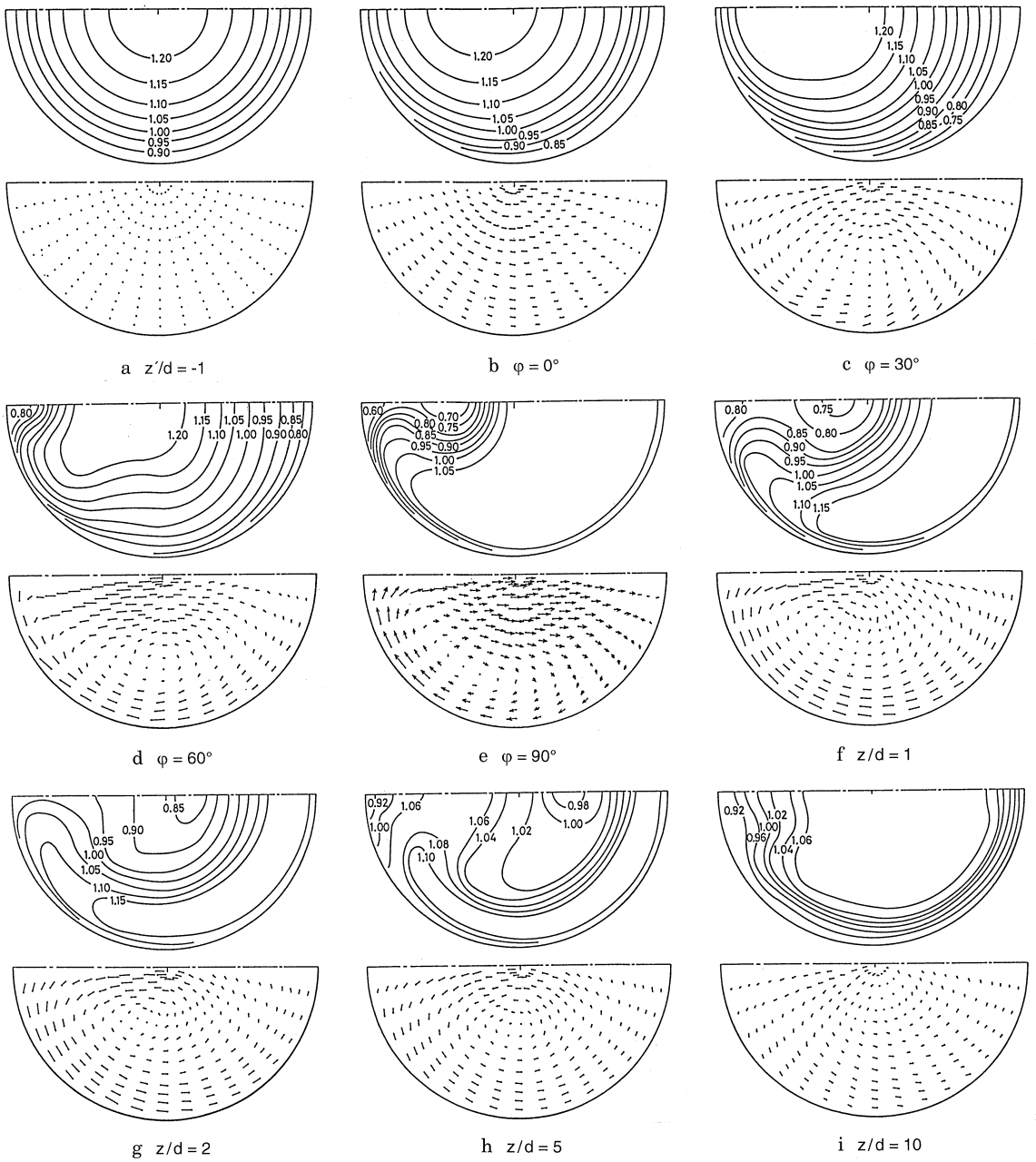

Figure 1.15: Reynolds-averaged velocities over different cross section. (Top figure: Axial velocity contours, where numerical values stand for W/Wb. Bottom figure: secondary flow velocity vectors. The left and right sides of each figure are the inside and outside walls in the bend, respectively). (From Sudo et al. [8])

Thereafter, the fast fluid in the primary flow (longitudinal one) moves

further towards the outer wall r_o along the symmetric horizontal plane of the bend pushed by the intense secondary flow. From $\varphi = 75°$ to $\varphi = 90°$ (Fig. 1.15e), the fast fluid previously conveyed to the outer wall is an other time carried towards the inner wall by the secondary flow moving inwards along the wall. From z/d=2 to 5 (Figs. 1.15g,h), the low velocity region moves farther towards the outer wall, and the secondary flow decays gradually. Further downstream, at z/d=10 the vortexes making up the secondary flow break down and the longitudinal velocity profile gets smoother without unevenness (Fig. 1.15i).

1.3.8 Sudo et al. $\Phi = 180°$ [9]

After the study on the $\Phi = 90°$ bend, Sudo et al. [9] investigated a $\Phi = 180°$ bend too. This case will be object of a numerical investigation in chapter 3. The geometry, flow conditions and coordinate system are exactly the same of the experiment in a 90° bend.

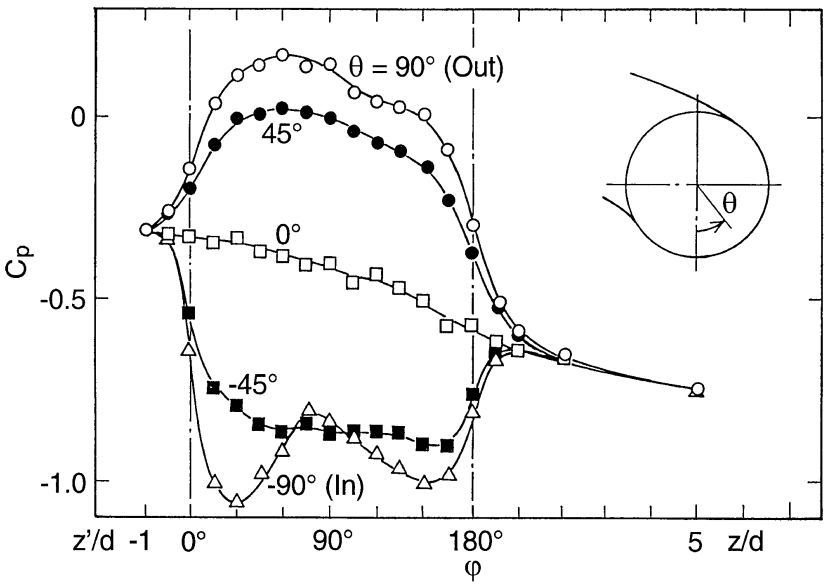

Figure 1.16: Coefficient of wall static pressure C_p measured for r azimuths: $\theta = 0°$, 45°, 90°, −45°, −90°, . From Sudo et al. [9]

The measurements employing a rotating probe with an inclined hot-wire proved the symmetry of the flow, so all analysis were made on half pipe section. The authors examined the pipe flow throughout measurements of the wall static pressure (Fig. 1.16), axial velocity (Fig. 1.17) alongside the curvilinear abscissa, as well as secondary flow, contour lines of in the half

cross section of the pipe for $\varphi = 0°,\ 30°,\ 60°,\ 90°,\ 105°,\ 120°,\ 150°,\ 180°,$ and for $z/D = 1\ 3.5\ 5\ 10$. (Fig. 1.18)

Measurements of fluctuating velocities as well as Reynolds stresses were carried out at various cross sections along and downstream the bend (Fig. 1.19).

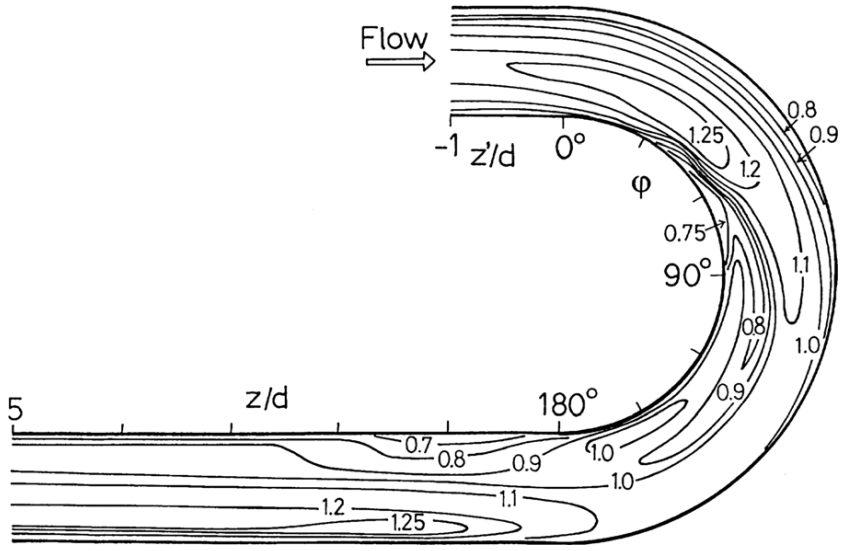

Figure 1.17: Contours of longitudinal mean velocity W/W_b on the horizontal plane

The case of $\Phi = 180°$ is not as different as the one of $\Phi = 90°$ bend flow for $\varphi = 60°$ which has been discussed in the previous paragraph 1.3.7. Downstream $\varphi = 75°$ the highvelocity region of the axial velocity observed in the central part of the cross section does not get as close to the r_o wall as much it occurs in the $\Phi = 90°$ case. From $\varphi = 90°$, the pick axial velocity is drifted towards the r_i side of the wall by the secondary flow moving inward. Starting from $\varphi = 105°$ (Fig. 1.17) the highest axial velocity points towards the inner-wall, and to the upper and lower walls as well (as the symmetry suggests). In this way, the strong secondary flow causes a deformation of the contours of W/W_b, (Fig. 1.18) and the contours show, at $\varphi = 120°$, the higher level near the upper and lower walls and the lower one in the central part of the bend. The reduction of the longitudinal velocity in the central region weakens the outward secondary motion in that region, at $\varphi = 150°$ the stagnant region of the secondary flow is between the bend center and the outer wall. Downstream the bend, the pressure close to the r_o side of the pipe wall decreases with the longitudinal distance z while the pressure at the inner wall increases with z. As velocity an pressured are strictly related, the fluid flowing near the outer wall is accelerated and the high-velocity region of the axial velocity moves on the horizontal plane near the r_o side (Fig. 1.17).

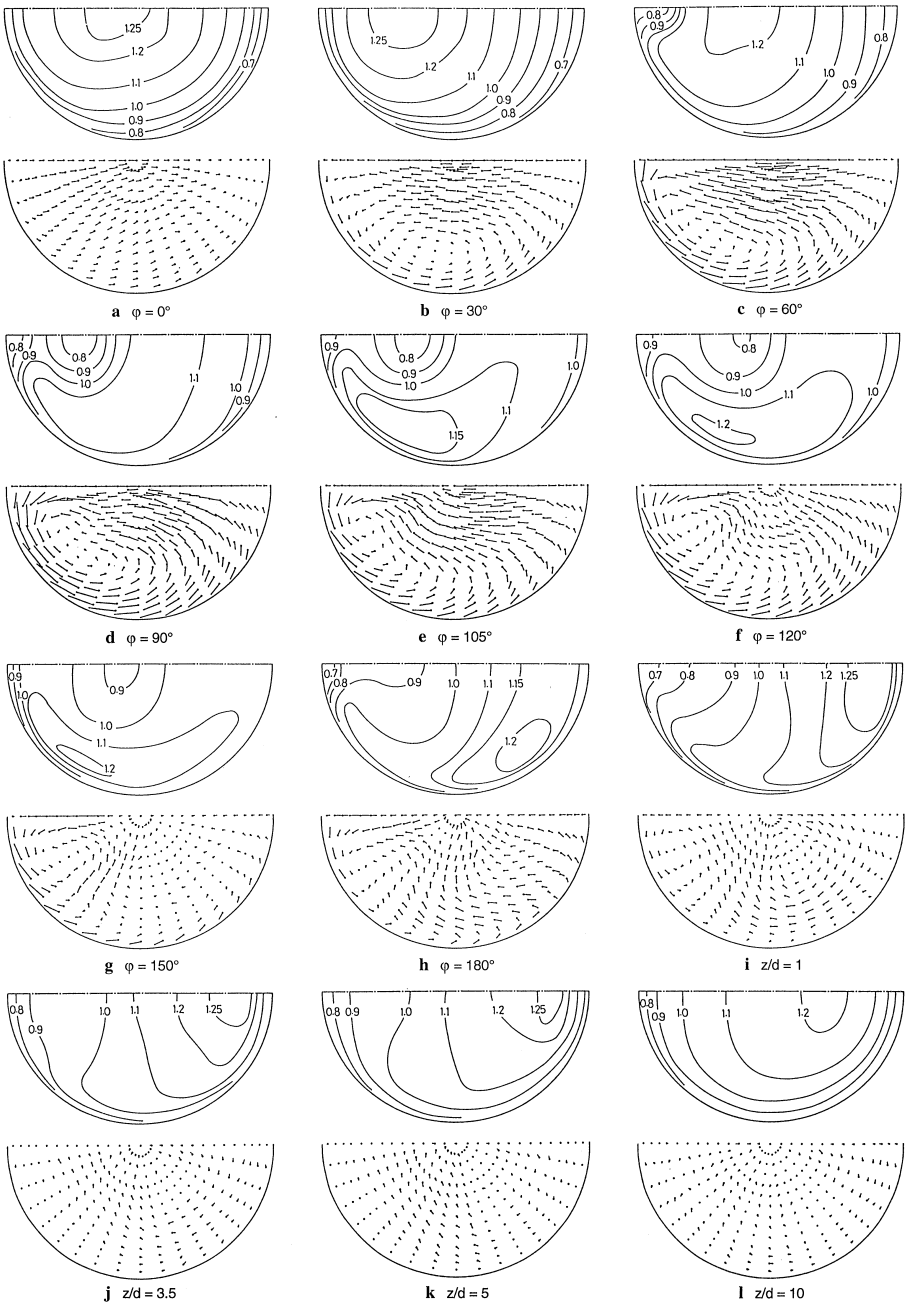

Figure 1.18: Experimental measurements by Sudo et al. [9] for each section is indicated the position in the pipe either with φ or with z/D and in the top picture is represented the distribution of W/W_b by isotachs in the half section an in the bottom picture represent the local cross-section velocities components. The left and right sides of each figure are the inside and outside walls in the bend, respectively.

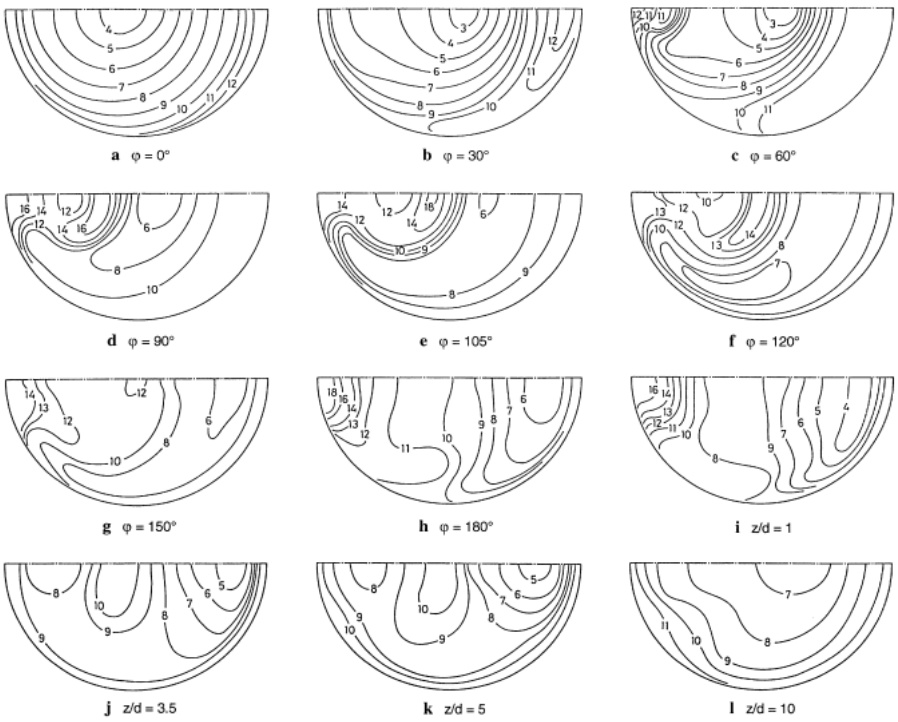

Figure 1.19: Experimental measurements by Sudo et al. [9] for each section is indicated the position in the pipe either with φ or with z/D for the fluctuating velocity w'/W_b. The left and right sides of each figure are the inside and outside walls in the bend, respectively.

This causes the outward secondary-flow to increase temporarily in the outer half of the pipe cross section (Fig. 1.18.h).

Chapter 2

Computational Fluid Dynamics of turbulent flow in pipe bends

2.1 The Reynolds-Averaged Navier-Stokes equations and commonly used turbulence models

2.1.1 The Navier-Stokes equations [15]

The Navier-Stokes equations govern the motion of fluids with Newtonian behavior. They consist of a scalar mass conservation equation and a vectorial momentum conservation equation. For the general case of compressible flow, these equations in cartesian coordinates have the following form:

$$\frac{\partial \rho}{\partial t} + \nabla \cdot (\rho \vec{v}) = 0 \tag{2.1}$$

$$\rho \left(\frac{\partial \vec{v}}{\partial t} + \vec{v} \cdot \nabla \vec{v} \right) = -\nabla p + \nabla \cdot \left(\mu \left(\nabla \vec{v} + (\nabla \vec{v})^T \right) - \frac{2}{3} \mu (\nabla \cdot \vec{v}) \mathbf{I} \right) + \rho \mathbf{F} \tag{2.2}$$

where $\vec{v}$ is the fluid velocity vector, p is the fluid pressure, ρ is the fluid density, and μ is the fluid dynamic viscosity. Each of the terms present in the momentum equation has a precise physical meaning, in fact, the terms in the left-hand side correspond to the inertial forces, whereas those in the right-hand side are pressure forces, viscous forces, and the external forces applied to the fluid. The vectorial momentum equation can be rewritten in terms of the three scalar velocity components u, v, and w.

Solution of Eqs. 2.1 and 2.2 with proper boundary conditions (such as inlets, outlets, and walls) and initial conditions (if the problem is not stationary) allows calculating the fluid velocity and the pressure at every spatial point in a given geometry domain at every instant of time. The Navier-Stokes equations show a high level of complexity, and they admit analytical solution for a limited number of cases in the laminar flow regime. For the laminar flow problems where an analytical solution cannot be found, and for all turbulent flow problems, the Navier-Stokes equations must be resolved numerically.

The fluid dynamic parameter that helps distinguish the laminar and turbulent flow regimes is the bulk Reynolds number already defined. The bulk Reynolds number $Re = \rho UL/\mu$, where U is a characteristic macro-scale velocity, and L a characteristic macro-scale length, represents the ratio of inertial forces and viscous forces. This parameter is related with the amount of turbulence present in the flux. In fact, low Reynolds numbers indicate a laminar regime, whereas higher Reynolds numbers indicate that the flow is in the turbulent regime.

Another significant dimensionless number is the Mach number, defined as: $M = U/c$. It represents the ratio of the characteristic macro-scale velocity of the flow, U, and the speed of sound in the fluid medium, c. The Mach number measures the extent of flow compressibility, and, in particular, if $M < 0.3$ the flow is usually considered incompressible. In such a case the continuity equation (Eq. 2.1) has a simpler form shown here:

$$\nabla \cdot \vec{v} = 0 \tag{2.3}$$

When the incopressible continuity equation (Eq. 2.3) is valid the Navier-Stokes (Eq. 2.2) loses a term resulting in the incompressible version (Eq. 2.4):

$$\rho \left(\frac{\partial \vec{v}}{\partial t} + \vec{v} \cdot \nabla \vec{v} \right) = -\nabla p + \nabla \cdot \left(\mu \left(\nabla \vec{v} + (\nabla \vec{v})^T \right) \right) + \rho \mathbf{F} \tag{2.4}$$

This is the case of the flows of interest in this thesis, and, therefore, hereafter reference will be made only to the incompressible formulation of the Navier-Stokes equations.

Coming back to Re, this parameter is often high in most engineering applications, entailing that the inertial forces are way greater than the viscous forces. In nature turbulence is a typical non-stationary, small-scale phenomenon. As mentioned before, for turbulent flows the Navier-Stokes equations do not have an analytical solution. When solving the Navier-Stokes equations numerically, the size of the computational cells and the time step of the time discretization must be fine enough to resolve the size and duration of the smallest eddies present in the flow, called Kolmogorov scales.

For the high Reynolds number flows usually encountered in industrial applications, such approach, referred to as direct numerical simulation (DNS), is beyond the computational capabilities of most of current computers and supercomputers.

2.1.2 The Reynolds Averaged Navier-Stokes equations

An alternative, more effective approach consists of solving the time averaged formulation of the Navier-Stokes equations, or Reynolds-Averaged Navier-Stokes (RANS) equations. The core idea of such approach is to solve only for the time-averaged velocity and pressure fields. As a result, no time discretization is required, and the spatial mesh resolution is dictated by the need to resolve only the integral scales of turbulence, thus drastically reducing the computing effort.

The concept at the basis of the transformation of Navier–Stokes into the Reynolds Averaged Navier-Stokes (RANS) equations is the Reynolds decomposition, already mentioned in paragraph 1.1.The Reynolds decomposition consists in expressing the generic flow variable, $\psi(x, y, z, t)$, which depends on space and time, into the locally time-averaged component, $\langle\Psi(x, y, z)\rangle$, which depends on space only, and the fluctuating component, $\psi'(x, y, z, t)$, which depends on time and space. In summary,

$$\psi(x, y, z, t) = \langle\Psi(x, y, z)\rangle + \psi'(x, y, z, t) \tag{2.5}$$

The meaning of the Reynolds-averaging operator is to average $\langle\psi(x, y, z, t)\rangle$ over a time interval that is long enough for the mean value to be independent of it, or, formally speaking

$$\langle\Psi(x, y, z)\rangle = \lim_{T\to\infty}\frac{1}{T}\int_0^T \psi(x, y, z, t)\mathrm{dt} \tag{2.6}$$

The rationale behind Eq. 2.6 is shown in Fig. 2.1.

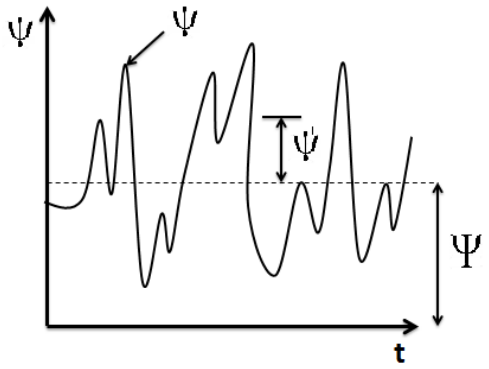

Figure 2.1: Reynolds-averaging of the generic fluid dynamic variable ψ.

The Reynolds decomposition of the pressure and the three velocity components yields:

$$\mathrm{u} = U + u', \quad \mathrm{v} = V + v', \quad \mathrm{w} = W + w' \quad \mathrm{p} = P + p' \tag{2.7}$$

Application of the Reynolds averaging operator to the continuity eaquation and Navier-Stokes (Eq. 2.4) yields the Reynolds-Averaged Navier-Stokes equations (RANS), which, for incompressible flow, are:

$$\begin{aligned} &\nabla \cdot \langle \vec{V} \rangle = 0 \\ &\rho(\langle \vec{V} \rangle \cdot \nabla)\langle \vec{V} \rangle = \rho \mathbf{F} - \nabla \langle p \rangle + \mu \Delta \langle \vec{V} \rangle - \nabla \cdot \mathbf{\Phi}^{\mathrm{Re}} \end{aligned} \tag{2.8}$$

where the tensor $\mathbf{\Phi}^{\mathrm{Re}}$ is :

$$\mathbf{\Phi}^{\mathrm{Re}} = - \begin{bmatrix} \rho \langle u'u' \rangle & \rho \langle v'u' \rangle & \rho \langle w'u' \rangle \\ \rho \langle u'v' \rangle & \rho \langle v'v' \rangle & \rho \langle w'v' \rangle \\ \rho \langle u'w' \rangle & \rho \langle v'w' \rangle & \rho \langle w'w' \rangle \end{bmatrix} \tag{2.9}$$

The primary unknowns of the RANS equations are the locally-averaged pressure, P, and the locally-averaged velocity vector, $\vec{V} = (U, V, W)$. However, additional unknowns appear in Eq.2.8, namely the six independent components of the Reynolds stresses tensor. These terms just appear as a consequence of having applied the Reynolds-averaging operation to the convection term of the Navier-Stokes equations. In order to close the system of equations, it is necessary to add closure laws for the Reynolds stresses, called turbulence models .

2.1.3 RANS-based turbulence models

Broadly speaking, turbulence models group into two main categories, namely, those based on the eddy viscosity assumption of Boussinesq and the Reynolds stresses models.

Regarding the first type of models, Boussinesq's work was based on the observation that the momentum transfer in a turbulent flow is dominated by large energetic turbulent eddies. He formulated the assumption that the turbulent shear stress depends linearly on the mean rate of strain. The amplification parameter is called eddy viscosity. The Boussinesq's assumption for Reynolds averaged incompressible flow can be translated in mathematical terms as:

$$\tau_{ij}^{\mathrm{R}} = -\rho u_i' u_j' = 2\mu_{\mathrm{T}} D_{ij} - \frac{2}{3}\rho k \delta ij \tag{2.10}$$

where D_{ij} is the Reynolds-averaged strain-rate tensor:

$$D_{ij} = \frac{1}{2}\left(\frac{\partial V_i}{\partial x_j} + \frac{\partial V_j}{\partial x_i}\right) \tag{2.11}$$

and k is the turbulent kinetic energy, that is, half the sum of the normal stresses divided by the fluid density, namely.

$$K = \frac{1}{2} u_i' u_i' = \frac{1}{2}[(u')^2 + (v')^2 + (w')^2] \tag{2.12}$$

The parameter μ_{T} (in Eq.2.10) is the eddy viscosity, which, unlike the molecular viscosity, μ, represents no physical characteristic of the fluid, but it is a function of the local flow conditions.

The eddy-viscosity assumption of Boussinesq is very appealing from an engineering prospective very appealing, since it just requires the assessment of a single scalar parameter μ_T to model all Reynolds stresses. This explain why eddy viscosity based models are so commonly used in Computational Fluid Dynamics applications.

However, there are situations in which Boussinesq's assumption is no longer valid, such as (i) flows with sudden change of mean strain rate, (ii) flows with significant streamline curvature (iii) flows with rotation and stratification (iv) secondary flows in ducts and in turbomachinery, and (v) flows with boundary layer separation. Such limitations arise from the isotropic behaviour of turbulence that the eddy viscosity assumption implies. Improvements might be made through the employment of non-linear eddy-viscosity turbulent models [2], but the most commonly practice is to use the Reynolds stresses models, which introduce transport equations for each of the six independent components of the Reynolds stresses tensor.

In the remainder of the section, the turbulence models used in this thesis will be briefly described, making reference to the formulation implemented in the PHOENICS code.

2.1.3.1 $k-\varepsilon$ standard turbulence model [6]

The $k-\varepsilon$ standard model is based on the assumption that $\mu_T = C_\mu k^2/\varepsilon$, where C_μ is an empirical constants, k is the already defined turbulent kinetic energy of the fluid, and ε is the turbulence dissipation rate. Transport equations for k and ε are added, as follows

$$\frac{\partial \rho k}{\partial t} + \nabla \cdot \left(\rho \vec{V} k - \frac{\mu_T}{\sigma_k} \nabla k \right) = \rho \left(P_k - \varepsilon \right) \tag{2.13}$$

$$\frac{\partial \rho \varepsilon}{\partial t} + \nabla \cdot \left(\rho \vec{V} \varepsilon - \frac{\mu_T}{\sigma_\varepsilon} \nabla \varepsilon \right) = \rho \frac{\varepsilon}{k} \left(C_1 P_k - C_2 \varepsilon \right) \tag{2.14}$$

where $P_k = 2\mu_T \mathsf{D} : \nabla \vec{V}$ represents the production of turbulent kinetic energy. The default values of the empirical constants are as follows: $C_\mu = 0.09$, $C_1 = 1.44$, $C_2 = 1.92$, $\sigma_k = 1.0$, $\sigma_\varepsilon = 1.3$.

2.1.3.2 $k-\varepsilon$ RNG turbulence model [13]

The RNG model takes its name from Re-Normalisation Group (RNG) methods to renormalise the Navier-Stokes equations, so that these equations to effects of smaller scales of motion. In the standard $k-\varepsilon$ model the eddy viscosity is computed only by one. In reality all scales of motion give their contribution to the turbulent diffusion. The RNG $k-\varepsilon$ models differ from the $k-\varepsilon$ model because modifies the production term in order to take into account the different scales of motion.

$$\frac{\partial}{\partial t}(\rho k) + \nabla \cdot \left(\rho k \vec{V} \right) = \nabla \cdot \left[\left(\mu + \frac{\mu_T}{\sigma_k} \right) \nabla k \right] + P_k - \rho \varepsilon \tag{2.15}$$

$$\frac{\partial}{\partial t}(\rho \varepsilon) + \nabla \cdot \left(\rho \varepsilon \vec{V} \right) = \nabla \cdot \left[\left(\mu + \frac{\mu_T}{\sigma_\varepsilon} \right) \nabla \varepsilon \partial x_j \right] + C_{1\varepsilon} \frac{\varepsilon}{k} P_k - C^*_{2\varepsilon} \rho \frac{\varepsilon^2}{k} \tag{2.16}$$

where:

$$C^*_{2\varepsilon} = C_{2\varepsilon} + \frac{C_\mu \eta^3 \left(1 - \eta/\eta_0 \right)}{1 + \beta \eta^3} \tag{2.17}$$

and $\eta = Dk/\varepsilon$; C_μ=0.0845; $\sigma_k = 0.7194$; $\sigma_\varepsilon = 0.7194$;
$C_{\varepsilon 1} = 1.42$; $C_{\varepsilon 2} = 1.68$; $\eta_0 = 4.38$; $\beta = 0.012$.
The RNG model offers improved accuracy in rotating flows, but it doesn't have any advantage on the other models concerning the ability to reproduce vortex evolution.

2.1.3.3 $k-\varepsilon$ Realizable turbulence model [14]

The Realisable $k-\varepsilon$ shows improvements in the performances in respect to the $k-\varepsilon$ model when applied to flows involving boundary layers in strong adverse pressure gradients, streamwise curvature, separation and recirculation zones. The model is a two-equation high-Reynolds-number turbulence model that differs from the standard $k-\varepsilon$ model firstly from the formulation of the transport equation for the dissipation rate that is derived from the transport equation for the mean-square vorticity fluctuations and secondly because the model uses a different eddy-viscosity formulation which is based on several realisability constraints for the turbulent Reynolds stresses.

$$\frac{\partial}{\partial t}(\rho k) + \nabla \cdot \left(\rho k \vec{V}\right) = \nabla \cdot \left[\left(\mu + \frac{\mu_T}{\sigma_k}\right) \nabla k\right] + \rho(P_k - \varepsilon) \tag{2.18}$$

$$\frac{\partial}{\partial t}(\rho \varepsilon) + \nabla \cdot \left(\rho \varepsilon \vec{V}\right) = \nabla \cdot \left[\left(\mu + \frac{\mu_T}{\sigma_e}\right) \nabla \varepsilon\right] + \rho C_1 D\varepsilon - \rho C_2 \frac{\varepsilon^2}{k + \sqrt{\nu\varepsilon}} \tag{2.19}$$

where:
$\eta = Dk/\varepsilon$;
$C_1 = \max\left[0.43, \frac{\eta}{\eta+5}\right]$;
$\mu_T = \rho C_\mu \frac{k^2}{\varepsilon}$;
$C_\mu = \frac{1}{A_0 + A_s \frac{kU^*}{\epsilon}}$;
$U^* = \sqrt{D_{ij}D_{ij} + \Omega_{ij}\Omega}_{ij}$;
$\Omega_{ij} = 0.5\left(\frac{\partial u_j}{\partial x_i} - \frac{\partial u_i}{\partial x_j}\right)$;
$A_s = \sqrt{6}\cos\phi$;
$\phi = \frac{1}{3}\cos^{-1}(max(-1, min(\sqrt{6}W, 1)))$;
$W = \frac{D_{ij}D_{jk}D_{ki}}{\tilde{D}^3}$;
$\tilde{D} = \sqrt{D_{ij}D_{ij}}$;
ν=cinematic viscosity; $C_2 = 1.9$, $\sigma_k = 1.0$, $\sigma_\varepsilon = 1.2$; P_k represents the generation of turbulence kinetic energy due to the mean velocity gradients.

2.1.3.4 $k-\omega$ Wilcox (1988) turbulence model [14]

This is a two-equation turbulence model based on the transport equations for the turbulent kinetic energy k and the turbulence frequency ω. $k-\omega$ models aren't as notables as the $k-\varepsilon$, but can have several advantages as a better performance when adverse pressure gradients are present. The model

is numerically very stable which means that it would converge quicker than the $k-\varepsilon$.

$$\frac{\partial}{\partial t}(\rho k)+\nabla\cdot\left(\rho k\vec{V}\right)=\nabla\cdot\left[\rho\left(\mu+\frac{\mu_T}{\sigma_k}\right)\nabla k\right]+\rho(P_k-f_2\varepsilon) \tag{2.20}$$

$$\frac{\partial}{\partial t}(\rho\omega)+\nabla\cdot\left(\rho\omega\vec{V}\right)=\nabla\cdot\left[\rho\left(\mu+\frac{\mu_T}{\sigma_\omega}\right)\nabla\omega\right]+\rho C_1 D\varepsilon+ \tag{2.21}$$

$$-\rho C_2\omega\left(f_1 C_{1\omega}\frac{P_k}{k}-C_{2\omega}\omega\right) \tag{2.22}$$

where:
$\mu_T=f_\mu k/\omega$;
$P_k=\mu_T\left(\frac{\partial U_j}{\partial x_i}-\frac{\partial U_i}{\partial x_j}\right)\frac{\partial U_j}{\partial x_i}$;
$\varepsilon=C_D\omega k$;
$f_\mu=(1/40+R_T/R_K)/(1+R_T/R_K)$;
$f_1=(1/f_\mu)(0.1+R_T/R_W)/(1+R_T/R_W)$;
$f_2=(5/18+(R_T/R_B)^4)/(1+(R_T/R_B)^4$;
$R_T=k/(\omega\mu)$;
$C_D=0.09\quad\sigma_k=2.0\quad\sigma_\omega=2\quad C_{1\omega}=5/9\quad C_{2\omega}=3/40\quad R_B=8$
$R_K=6\quad R_W=2.7$
R_T is the turbulence Raynolds number.

2.1.3.5 $k-\omega$ SST turbulence model[14]

The $k-\omega$ SST (Shear Stress Transport) is a two-equation turbulence model based on the transport equations for the turbulent kinetic energy k and the turbulent shear stress. It offers improved predictions of flow separation under adverse pressure gradients.

$$\frac{\partial}{\partial t}(\rho k)+\nabla\cdot\left(\rho k\vec{V}\right)=\nabla\cdot\left[\rho\left(\mu+\mu_T\sigma_k\right)\nabla k\right]+\rho(P_k-\varepsilon) \tag{2.23}$$

$$\frac{\partial}{\partial t}(\rho\omega)+\nabla\cdot\left(\rho\omega\vec{V}\right)=\nabla\cdot\left[\rho\left(\mu+\mu_T\sigma_\omega\right)\nabla\omega\right]+\rho\omega\left(\gamma\frac{P_k}{k}-\beta\omega\right)+$$
$$+2(1-F_1)(\rho\sigma_{\omega 2}/\omega)\nabla k\nabla\omega \tag{2.24}$$

where:

$\mu_T = (a_1 k)/max[a_1\omega, DF_2]$;
$P_k = \mu_T(\nabla\vec{V} + (\nabla\vec{V})^T):\nabla\vec{V}$;
$\varepsilon = C_D\omega k \; F_1 = tanh(A_1^4)$;
$A1 = min[max(\sqrt{k/(C_D\omega\delta)}, 500\nu/(\omega\delta^2)), 4k\sigma_{\omega 2}/(D_\omega\delta^2)]$;
$D_\omega = max[2(\sigma_{\omega 2}/\omega)\nabla k\nabla\omega, 10^{-10}]$;
$F_2 = tanh(A_2^4)$;
$A_2 = max(\sqrt{k/(C_D\omega\delta)}, 500\nu/(\omega\delta^2))$;
where δ is the distance to the nearest wall
$\sigma_{k1} = 0.5 \quad \sigma_{\omega 1} = 0.5 \quad \beta_1 = 0.075$;
$\sigma_{k2} = 1 \quad \sigma_{\omega 2} = 0.856 \quad \beta_2 = 0.0828$;
$C_D = 0.09 \quad C_{1\omega} = 5/9 \quad C_{2\omega} = 3/40$;

2.2 Strategies and best practices in Computational Fluid Dynamics

The term "Computational Fluid Dynamics" (CFD) refers to the application of numerical techniques to solve the fluid flow equations. On the grounds of what stated before, in the case of turbulent flows an engineering-effective approach consists of solving the Reynolds Averaged formulation of the Navier-Stokes equations (RANS), coupled with a turbulence model.

A CFD model is approximated in nature, and, therefore, the reliability of CFD predictions is highly dependent on the numerical method employed. CFD codes, such as Ansys Fluent, Ansys CFX, PHOENICS, STAR CCM+, Open Foam etc, use specific algorithms and numerical techniques to solve fluid flow problems. In all cases, the flow domain is discretized in fluid elements called cells, where the fluid dynamic parameters, such as the mean pressure, the mean velocity, and turbulence variables are calculated. In order to solve the flow equations, the boundary conditions must be specified. Common types of boundary conditions used in CFD are inlet with imposed flow-rate, outlet with fixed pressure and zero-normal gradient of all other variables, solid walls, and symmetry. The computation then consists in the application of the conservation principle of mass, momentum and energy to each cell with consideration of the neighboring cells. In mathematics terms, this is carried out through a system of algebraic equations with the variables representing each cell's characteristics.

Since several, strongly coupled algebraic equations need to be solved over grids with a considerable number of nodes, proper solution algorithms needs to be used. Generally, iterative methods are used, in which, starting from an initial guess, the solution is reached, where the term "solution" means the

value of all parameters in each cell of the domain [12].

The more relevant steps of a CFD analysis can be gathered into three categories, namely, pre-processing, processing, and post-processing.

In the *Pre Processing* it's chosen the coordinate reference system that best suit the case in order to modellize the geometry of the specific case of interest. Through the choice of the turbulent model are chosen the mathematical equations making up the physical model. Each model has its parameters and variables. Additionally the user has to set up a grid to discretize the computational domain. In the end the boundary condition ought to be chosen, and is it is not a stationary problem the initial condition too.

In the *Processing* phase are chosen the mathematical resolution method, the maximum running time for the simulation, the maximum number of iteration to be performed, the convergent criterion and the computation, meanwhile the user can monitor the evolution of the symulation.

In the *Post Processing* of the solution of the numerical simulation is analysed, the results are being manipulated, they are displayed and a report can be composed.

The numerical techniques employed in CFD can be grouped into three main categories, namely finite difference method, finite volume method, and finite element method. Among them, the most widely used one is the finite volume method. As already mentioned, the method relies on a spatial discretization of the domain in cells and it employs an iterative algorithm to solve the discretized formulation of the NS/RANS equations. The user has to define the geometry of the domain, the boundary conditions, and the computational mesh. Mandatory requirements for achieving a reliable CFD solution are convergence and grid independence.

Here the term "convergence" is related with the iterative nature of the solution algorithm. Every step of the algorithm updates all fluid dynamic parameters in each cell, and the new values differ by a certain quantity from the previous ones. This quantity is called residual. Hence convergence is reached when the residuals get very small. Residuals might be used to asses whether a sufficient level of convergence has been reached [10]. Residuals, in fact, measure the imbalances or, in other words, the errors in the equations in each step of the algorithm. Residual under no circumstances can be exactly zero in CFD computations. Nonetheless, the lower the residual value is, the more numerically accurate the solution. This said, each CFD code employs its own procedure for normalized the solution residuals and, therefore, usually reference is made to the normalized whole-field residuals, i.e. scalar quantities representing how each solved variable varies "on average" between one iteration and the subsequent one. According to [10] , normalized residual levels of the order of 10^{-4} are considered to be loosely converged,

levels of the order of 10^{-5} are considered to be well converged, and levels of the order of 10^{-6} are considered to be tightly converged. For complex flows, however, it is not always possible to achieve normalized residual levels as low as 10^{-5} or even 10^{-6}. The algorithm follows iterative calculations for each cell of the discretized domain until either convergence a maximum number of iterations are reached. In the former case, the algorithm will stop when all normalized whole-field residuals fall below a prescribed value or when the number of iterations is equal to the maximum allowable number of iterations. In the latter case the degree of convergence of the solution might be assessed by inspecting the whole-field residuals related to the last iteration.

As far as the error induced by the domain discretization is concerned, effective grid design relies largely on an insight into the expected properties of the flow. Many times, simulations are firstly run on coarse meshes with the only purpose of detecting the general characteristics of the solution. In order to reduce or avoid errors associated with a too coarse domain discretization, a grid independence study is needed, which is a procedure of successive refinement of an initially coarse grid until certain parameters of interest for the problem under consideration do not change significantly. If this occurs, the solution is called grid independent.

As a final note, it is remarked, that, thanks to the increase in computer power, CFD has become a practical very useful tool for studying fluid dynamic problems. Compared with laboratory and field experiments, CFD (i) is much cheaper, (ii) provides the user comprehensive three-dimensional flow field, thus the interpretation of flows much easier and more detailed, and (ii) makes it relatively simple to perform sensitivity analyses. Conversely CFD models are intrinsically approximated. Moreover when the flow is turbulent the solution provided by the software is strictly dependent on the choice of the turbulence model. So far, it does not exist a turbulence model that in whichever case always performs better than others. For this reason the CDF simulations need to be sustained by experimental simulation that give the possibility to validate the model. Only when the CFD model is experimentally validated at least for a significant number of variables, it can be used as a powerful inference model.

2.3 Previous CFD studies on turbulent flows in pipe bends

Unlike experiments, CFD provide the user the comprehensive three-dimensional flow field and the values of each relevant fluid dynamic para-

meter in the whole domain volume. Due to its low computational cost, it is not surprising to realize that several numerical investigations of turbulent flows in pipe bends were made following the RANS approach. Of course, this choice was made being aware the limits of such approach in representing the instantaneous nature of turbulence.

The purpose of the first studies was essentially to validate the capabilities of RANS-based CFD models to capture the essential features of turbulent flows in pipe bends. Conversely, the focus of the most recent investigations was to examine whether the secondary flow in a curved pipe is driven by the turbulence and, therefore, several turbulence models were employed and their predictions compared. As already discussed in section 2.1.2, RANS-based turbulence models can be distinguished in two main categories, namely those based on the eddy-viscosity assumption, and those based on the transport of the Reynolds stresses. The second family of models might appear more suitable to describe the anisotropic behaviour of turbulence occurring inside a pipe bend. Conversely, the Boussinesq assumption of isotropic turbulence and, therefore, would appear less appropriate for application to pipe bend flows. Both numerical and experimental simulations hinted that in the cross-stream half plane are present actually three distinguished cells taking place for turbulent flow: a Dean cell, a second cell formed near the pipe center as a consequence of a local imbalance of centrifugal force together with radial pressure gradient (as pointed out in paragraph 1.3.5), as well as a third one. The last cell is expected to be purely driven by turbulence itself. Finally, it is noted that, although much research efforts have been devoted to this topic in the last decades, the actual capability of RANS-based CFD models (either based on the eddy viscosity or solving for each components of the Reynolds stresses tensor) to investigate flows in bend pipes where secondary flows takes place is still unclear. [5]

In the remainder of the section, an overview of relevant previous RANS-based numerical investigations is provided 2.1.

Author and year	model	γ [-]	Φ [°]	Quantities measured
Patankar 1975 [5]	standard $k-\varepsilon$	0.042	180	U, V, W
Azolla 1986 [1]	standard $k-\varepsilon$	0.15	180	W, U
Al Rafai 1990 [11]	standard $k-\varepsilon$	0.07 0.14	90	uRMS, W, U, V
Pruvost 2004 [7]	Low-Re $k-\varepsilon$	0.25 0.077	90/180	W, P_{tot}

Table 2.1: Summary of main numerical simulations

2.3.1 Patankar et al. (from [5])

Patankar and co-workers were the first researchers to make an attempt to use the $k - \varepsilon$ standard turbulence model to simulate the flow passing through a bend. In particular, they reproduced the experiments of Rowe for a developing flow in a $\Phi = 180°$ elbow, as reported in Table 1.1. In the light of the rather small $\gamma = 0.042$, the authors made the assumption of parabolic flow, which gave appreciable results over most of the bend. However, the parabolic solver was unable to represent accurately the cross-section pressure gradient.

2.3.2 Azzola et al. [1]

Azzola et al. [1] numerically reproduced their own experiments, previously described in paragraph 1.3.4 The numerical procedure relied on a semi-elliptic discretization of the equations expressed in toroidal coordinates, since it specifically focused on the bend domain. In order to make the computation process more efficient, they employed different grids for different variables because, for example, the rate of space variation of the velocity is different from that of the pressure. The authors used the $k - \varepsilon$ standard model for reason of computational speed, and they defined a very fine near-wall grid discretization to capture the entire boundary layer, including the viscous sublayer. Taking advantage of the symmetry of the mean flow field, the authors simulated only half of the physical domain. Firstly, 53 pipe diameters were simulated upstream the bend to guarantee that the flow entering the elbow was fully developed. Afterwards, the authors used the downstream profiles of the variables as an inlet profile just 2 pipe diameters before the U-bend. The domain was extended 8 pipe diameters downstream of the bend, where zero-streamwise gradient constraints were applied to all variables except for pressure. The mesh used had a 28 cells for the radial non-uniform discretization, and 24 uniformly-spaced circumferential cells mapping the semi-circular and 160 axial planes, for a total amount of 107520 elements. The authors proved that this discretization guarantees the solution being grid independent.

The validation of the CFD simulations performed by Azzola et al. [1] is presented in Figs. 2.2 and 2.3 in terms of longitudinal (W/W_b) and circumferential (V/W_b) velocity components (normalized by the bulk velocity) and their respective turbulence intensities (w'/W_b), (v'/W_b) (once again, normalized by the bulk velocity). Having used the $k-\varepsilon$ standard turbulence model, in the calculations, $u' = v' = (2k/3)^{1/2} = uRMS$. Although Figs. 2.2 and 2.3 refer to a bulk Reynolds number $Re = 57400$, the authors claimed that

the dimensionless profiles are not at all significantly different from those obtained with $Re = 110000$. The profile of the longitudinal velocity component W and its related RMS value measured upstream the bend at $z'/D = -2$ are compliant with the fully developed flow in a straight pipe. Inside the bend, the plots indicate that the flow is accelerated toward the inner radius of the pipe, in agreement with the conclusions drown by authors of many other studies concerning the same kind of flow. The W-profiles prove that the flow near the inner wall (r_i) accelerates in the first half of the bend ($\varphi =$ from 3° to 90 °). Additionally, the V-profiles (radial velocity) prove the presence of the development of a strong secondary flow. As already mentioned, this secondary flow is caused by the imbalance between the centrifugal force and the pressure gradient set up between the outer r_o and inner r_i wall regions of the bend. It's interesting to point out that, close to the wall, the cross-section secondary flow becomes relatively intense. In fact, V becomes as high as $0.30W_b$ at $\varphi = 45°$. Surprisingly, between φ= 45° and 135° the V-profiles reveal a striking of the flow being directed towards the inner part of the bend r_i. The occurrence of a second cross-stream flow (second cell) after φ= 90° supports the concept proposed by Rowe (section 1.3.2), according to which this is a smaller and weaker structure, mainly confined in the core ($r < R/2$), whose presence was attributed to the raise of transverse pressure gradient opposite in sign in respect to that measured for smaller φ.

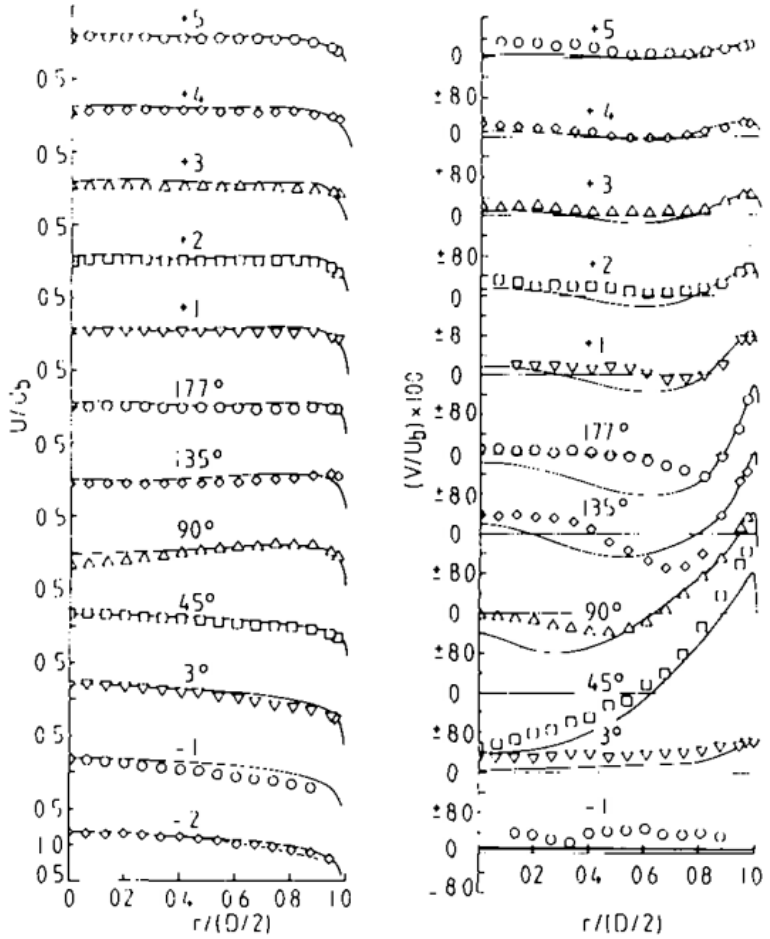

Figure 2.2: Measurements (points) and calculations (continuous lines) of the dimensionless longitudinal W/W_b (left) and circumferential U/W_b (right). The mesurements are made for the section $z/D = -2\ -1\ \varphi = 3°,\ 45°,\ 90°,\ 135°,\ 177°$ and $z/D = 1,\ 2,\ 3,\ 4,\ 5$. From Azzola et al. [1]

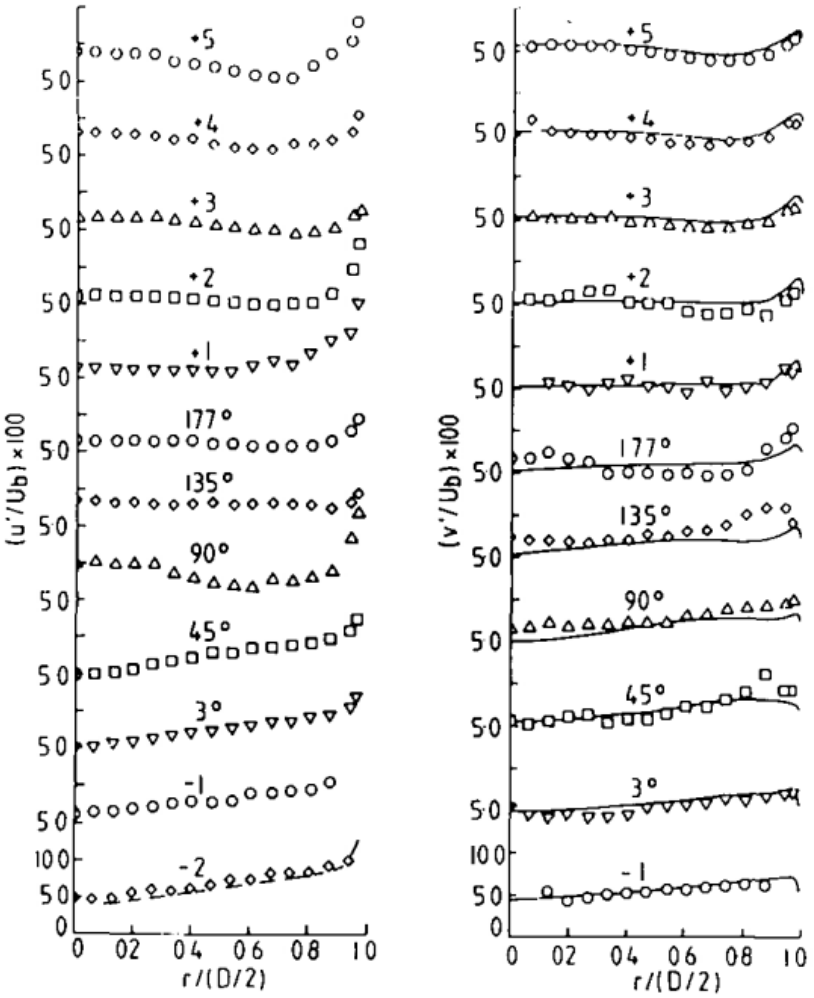

Figure 2.3: Measurements (points) and calculations (continuous lines) of the dimensionless longitudinal turbulence intensity w'/W_b (left) and circumferential turbulence intensity u'/W_b (right). The measurements are made for the section $z/D = -2 \; -1$ $\varphi = 3°,\ 45°,\ 90°,\ 135°,\ 177°$ and $z/D = 1,\ 2,\ 3,\ 4,\ 5$. From Azzola et al. [1]

In conclusion, the numerical simulations performed by Azzola et al. [1] were able to reproduce with a gratifying degree of fidelity the measured evolution of the flow. This led the authors claim that "*the $k - \varepsilon$ standard model does better in simulating really complex flows, such as those found within the 180° bend, than it does in less strongly perturbed flows*".

2.3.3 Al Rafai et al.[11]

Al-Rafai et al. after investigating the turbulent flow through curved pipes $\Phi = 90°$ with an experimental simulation (paragraph 1.3.6) They also

performed numerical simulations with a $k - \varepsilon$ turbulence model and a mesh of $N\theta = 14$ $Nr = 15; Nz = 32$ in the bend. The comparison between the experimental and numerical results were not enough satisfying as visible in Fig. 2.4

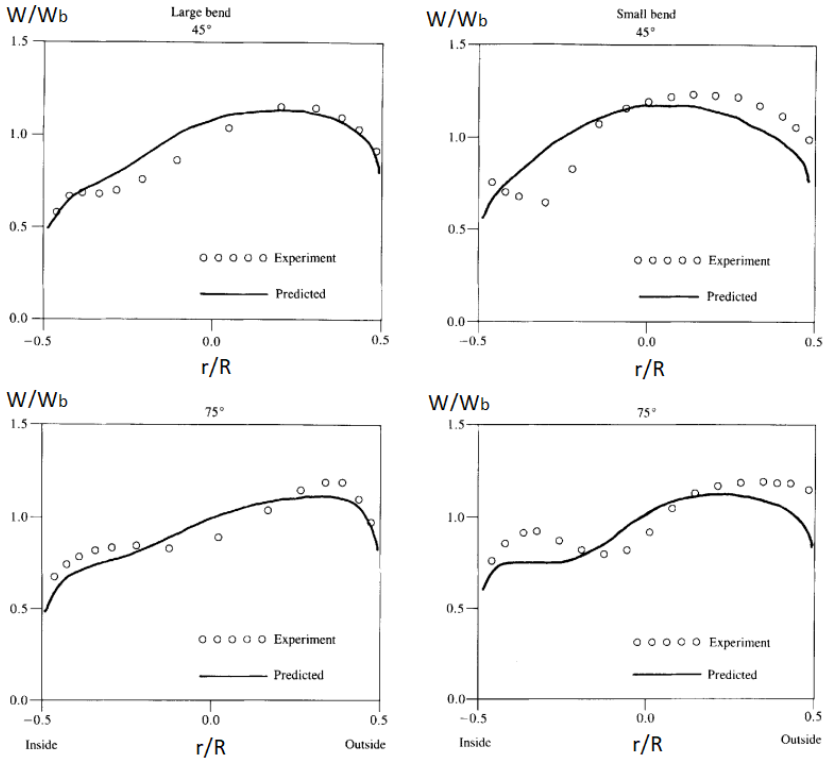

Figure 2.4: Profile of the dimensionless longitudinal velocity W/W_b for $\varphi = 45°$, $75°$ in the first bend with $R_c = 0.58$m (left) and the second bend with $R_c = 0.29$m (right) by Al Rafai et al. [11]

Moreover the authors Al Rafai et al. [11] plotted for four section the numerical results of the simulation $\varphi = 0°$, $15°$, $45°$, $90°$. The secondary flow is represented by the vectors and adimensional W/W_b is represented by the contour lines (Fig. 2.5).

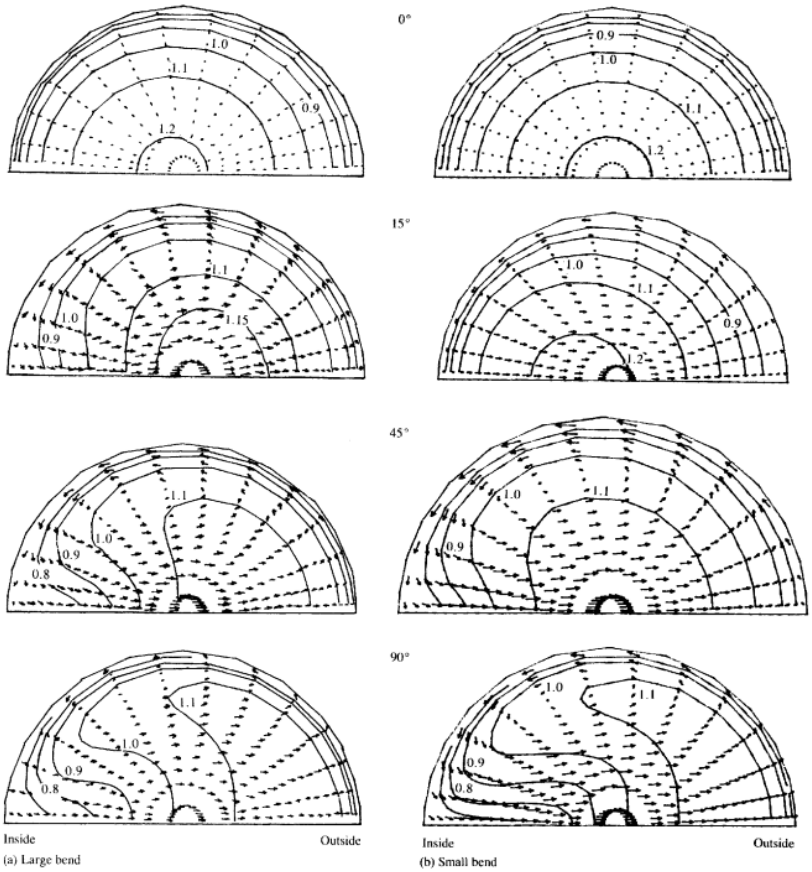

Figure 2.5: Contour plots of dimensionless longitudinal velocity W/W_b and secondary flow velocity components for sections $\varphi = 0°,\ 15°,\ 45°,\ 90°$ in the first bend with $R_c = 0.58$m (left) and the second bend with $R_c = 0.29$m (right) by Al Rafai et al. [11]

2.3.4 Pruvost et al. [7]

Pruvost et al. [7] performed numerical simulations to reproduce experiments by Anwer and So regarding the turbulent air flow in a $\Phi = 180°$ pipe bend with $D = 0.0762$ $R_c = 0.495$ $\gamma = 0.077$, and $Re = 50000$, focusing on the influence of adding a swirl at the entrance of the bend.

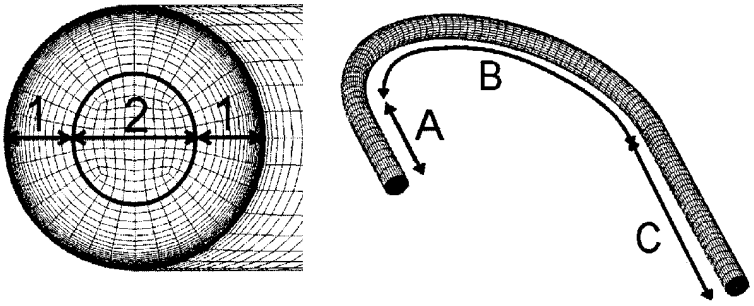

Figure 2.6: Non uniform mesh in the axial and radial directions

The authors ensured that the flow entering the bend was fully-developed. In this work, different grid refinement where applied for different parts of the domain to reduce the computational effort as well as to detect thorough changes where it was needed. In particular the domain was divided in three regions along the axial direction and in two regions along the radial direction (Fig. 2.6). The grid spacing was not uniform throughout the different regions. In the radial direction, the grid was finer near the wall. In the bend, the axial grid spacing was made uniformly fine, whereas, in the upstream and downstream parts, it was non uniformly distributed, being finer close to the bend and coarser further from the curve part of the duct. The results obtained where being ensured to be independent from the grid since different refinement of the grid were employed to asses the sensibility of the solution to different sizes of the cells. The computational domain was eventually subdivided into 50244 cells.

In their study, Pruvost et al. [7] deeply analyzed the influence of the turbulence model on the CFD predictions. Three years before, Wang and Shirazi [7] compared the standard $k-\varepsilon$ model with wall functions and the low-Re $k-\varepsilon$ model, when reproducing the flow in a curved pipe of Φ =180° bend. Although two methods gave an acceptable degree of conformity with the experimental data, none of them stood up for representing the experimental information better then the other. As a result, the $k-\varepsilon$ model was preferred between the two due to its higher degree of simplicity. In addition to those two option, Pruvost et al. [7] considered two other $k-\varepsilon$ variants, and a Reynolds stresses model. Figure 2.7 shows the results of several simulations

on the 180 ° case employing different models with no swirl addition at the inlet.

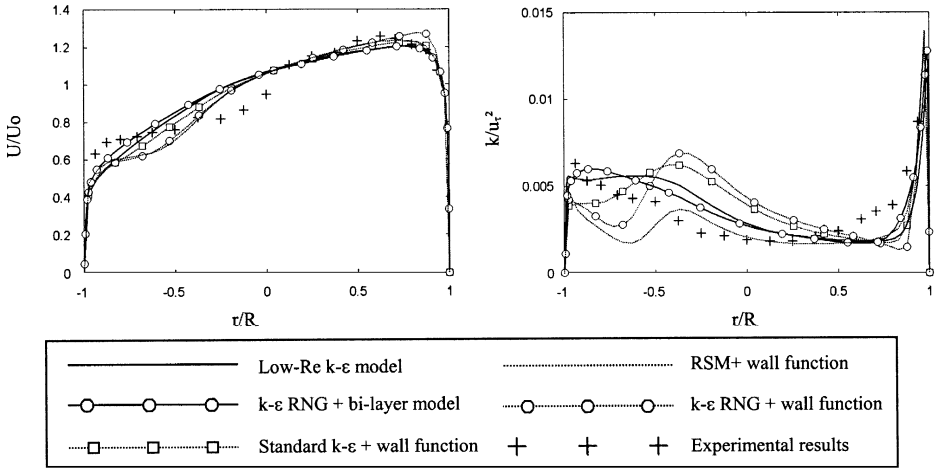

Figure 2.7: Results obtained with different numerical models $\Phi = 180°$ at $z/D = 1$, here the author called U the the axial velocity W. From [7].

In the Fig. 2.7, u_τ that represent the wall friction velocity value, here set to $u_\tau = 0.323$ m/s. The authors noted that, in section z/D=1, the models do not provide dramatically different solutions, especially in terms of mean axial velocity. The situation changes if swirl is added at the inlet as, in this case, the turbulence models give more different results (Fig. 2.8). The authors concluded that the low-Re $k - \varepsilon$ model better represented the experimental data nonetheless the standard version of the $k - \varepsilon$ model didn't performed bad either. Therefore, in spite of the formal incapability of eddy viscosity based models to predict anisotropy turbulence in flows, the low-Re $k - \varepsilon$ model appear rather effective. However, it is noted that the sensitivity analysis was not comprehensive, as it was restricted to a specific case and to few fluid dynamic parameters.

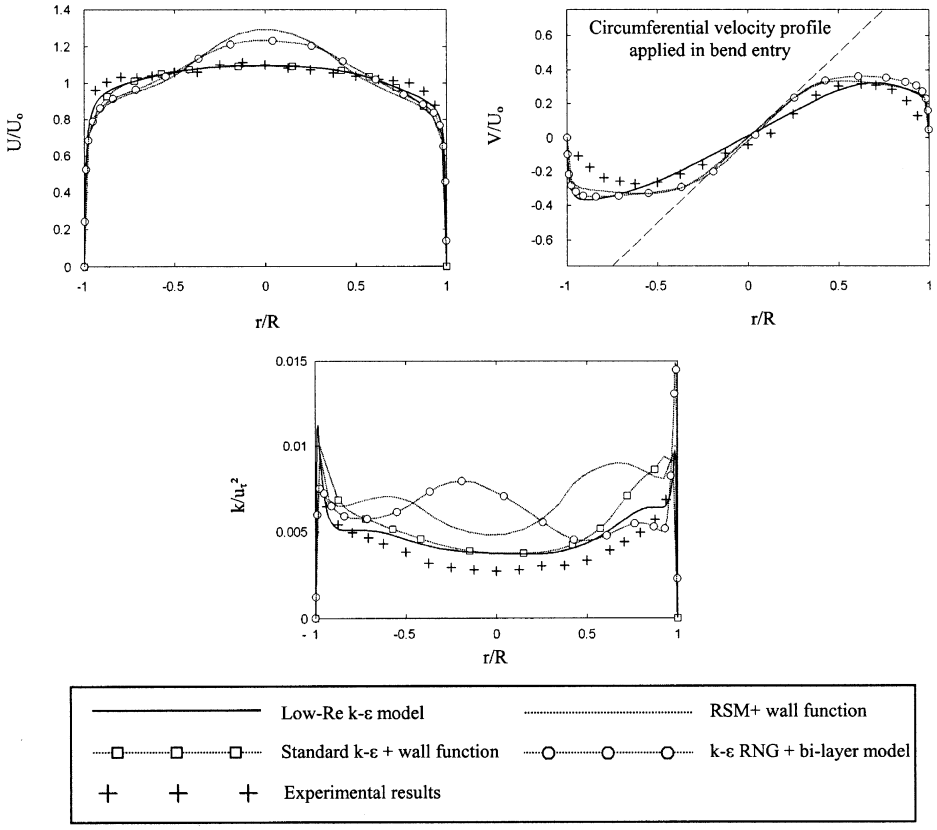

Figure 2.8: Results obtained with different numerical models for $\Phi = 180°$ at $z/D = 1$ with swirl at the inlet.

Chapter 3

Numerical simulation of the experiments by Sudo et al. [9]

This chapter will focus on the numerical simulations related to the experimental case of Sudo concerning a 180° pipe bend. The software used was PHOENICS version 2018 by CHAM Limited. The software allows to perform steady and unsteady CFD simulations using either RANS-based or LES-based CFD models. In this thesis, use was made of steady-state, RANS-based models.

3.1 Implementation of the numerical setup

The pre-processing stage of a PHOENICS simulation follows the panels in the main menu window of the code (Fig. 3.1).

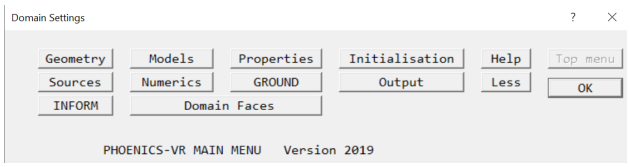

Figure 3.1: Main menu of PHOENICS

Firstly, in the "Geometry" panel, the user must define the geometry of the case study, including the coordinate system, and its discretization through the computational mesh. As previously mentioned when discussing the experimental results, the mean flow is symmetric in respect to the horizontal plane that divides the domain into two specular parts. Taking advantage of such symmetry considerations, the CFD simulations are performed over one half of the pipe section, thus broadly halving the computational effort. A

mixed cylindrical-polar and toroidal coordinate system was chosen to set up the flow domain, consisting of a straight upstream pipe segment, a 180° pipe bend, and, finally, another straight pipe segment. This was achieved through the "body fitted coordinates" option. The first and the third sub-domains (namely, the upstream and downstream pipes) use a cylindrical-polar coordinate system, where each cell is individuated by the azimuthal coordinate, the radial coordinate and the axial coordinate, referred to as X,Y, and Z in PHOENICS. In the second sub-domain, representing the 180° pipe bend, a toroidal coordinate system is used.

From an operative point of view, the user starts by defining a cylindrical-polar coordinate to create a straight pipe segment whose length is equal to the entire length of flow domain. In the tool window of PHOENICS (Fig.3.2) the user inserts the size of the domain along the azimuthal, radial, and axial directions, which are $X = \pi$, $Y = D/2 = 0.052$ m, and $Z = 140D = 14.56$ m, respectively. At the same time, the user must set the number of subdivisions along the three coordinates, which, in this examples, are 40 in the angular and radial directions and 564 in the axial one. The result is as shown in Fig. 3.3.

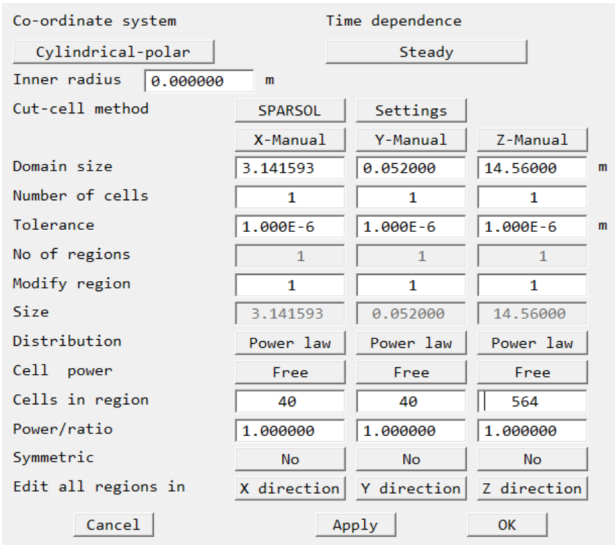

Figure 3.2: Definition of the upstream pipe domain

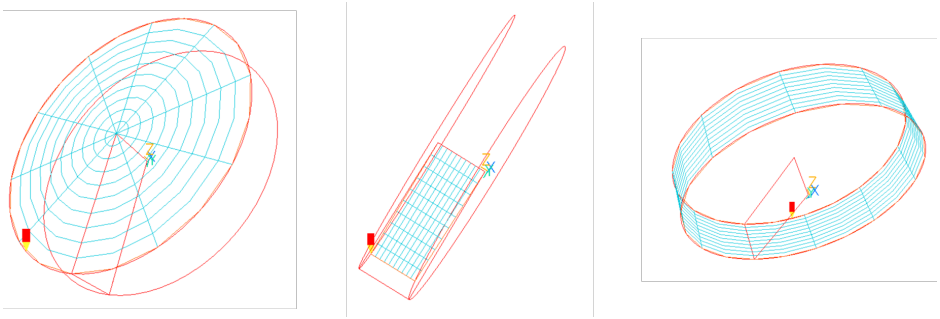

Figure 3.3: A typical discretization using cylindrical-polar coordinates

Afterward, the pipe bend sub-domain is built using the Body Fitted Coordinates (BFC) option. Up to this point, the three-dimensional domain is a half straight pipe discretized in cylindrical-polar coordinates. As it is visible in Fig. 3.4, the tool "revolve" allows bending a portion of the domain along the coordinate Z, which now becomes a curvilinear abscissa. Since the bend is positioned from the 61^{th} slab of cells up to the 301^{th} one, and brings an overall revolution of 180° with the double of curvature radius $R_c = 0.208$ m. Since the upstream pipe segment is $100D = 10.4$ m long, the revolution starts in the 61^{th} plane which is situated at a distance 10.4m from the origin. This happens because cylindrical coordinates are employed upstream and downstream the bend, whereas toroidal coordinates are used inside the bend. The power ratio was set to a unit value inside the bend to produce a uniform discretization. In the case the slabs were to be densified close to the bend entrance, the power ratio of the bend sub-domain would have been smaller than 1. Conversely, the slabs were not uniformly distributed in the upstream and downstream pipes, where they were densified close to the interface with the bend subdomain. Figure 3.5 exemplifies the use of power ratio of -2.4 in the inlet straight pipe segment and a power ratio of 2.4 in the downstream part of the pipe starting from $5D$ downstream of the bend.

Then, in the "Model" panel, the user must define the fluid dynamic equations solved and, in the case of RANS-based modelling, the turbulence model employed. The software provides several turbulence models. Initially, the $k-\varepsilon$ standard turbulence model is used. Other simulations were performed using RNG $k-\varepsilon$, Relizable $k-\varepsilon$, $k-\omega$, and SST $k-\omega$.

In the experiment carried out by Sudo and co-workers the working fluid was air, thus the fluid properties defined in the "Properties" panel were those of air at 20°C, with a density $\rho = 1.189\text{kg/m}^3$ and $\mu = 1.81 \cdot 10^{-5}\text{Pa·s}$.

At this point, the boundary conditions must be defined. These are inlet, outlet, solid wall (plate in PHOENICS), and symmetry. The inlet covers the entire first slab of cells; at this boundary, the three mean velocity components

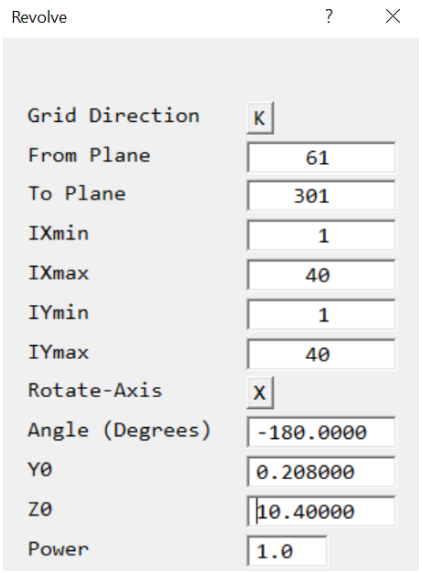

Figure 3.4: Definition of the bend geometry using Body Fitted Coordinates (BFC)

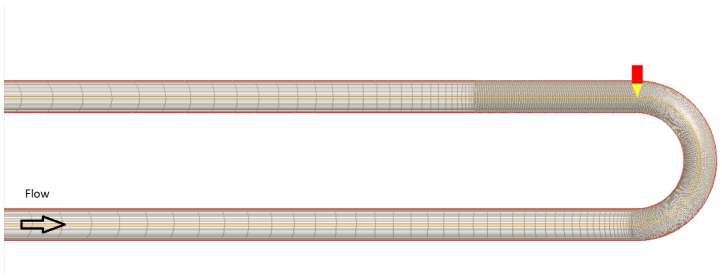

Figure 3.5: Example of use of power ratio of -2.4 upstream the bend and 2.4 starting from $5D$ downstream of the bend

and the turbulence variables are specified. The radial and the azimuthal velocity components are set to zero, whereas the streamwise velocity was $w_0 = 8.7$ m/s, as in the experiments. Regarding the turbulent parameters k, ε, ω are set autonomously by the software PHOENICS. The outlet is placed in the last slab and, at this boundary, the pressure is imposed equal to the atmospheric pressure, and the normal gradient of all other variables is set to zero. The wall (plate) boundary condition represents a hydraulically smooth impermeable surface, that is placed externally over the cells that have the radial coordinate equal to the pipe radius $r = R$. The remaining boundary surface coincides with the symmetry plane, which is an impermeable surface over which the angular velocity and the fluid wall shear stress are zero.

The panel "Initialization", shown in Fig.3.1, allows attributing constant initial values to one or more variables such as U, V or W etc. Generally, a

suitable initialization speeds up the velocity at which convergence is reached. Setting the initial value of W in the whole domain equal to the inlet value gives as a result a quicker convergence, especially when fine meshes are used.

Finally, in the panel "Numerics", the user can set the maximum number of iterations to perform during a simulation, as well as define the global convergence criterion based on a threshold value of the whole-scale residuals. The global convergence criterion relates with the desired degree of accuracy of the solution. In fact, when the threshold residual is reached for all calculated variables, the solution is considered to be convergent.

The computational domain used for the numerical simulations is visible in Fig. 3.6. Note the presence of the monitoring probe at the end of the bend; the probe is the sensor that the user can move in any domain's cell to measure the value of the variables (pressure, velocity) in the desired cell. The numerical setup accurately represents the experimental setup of Sudo and co-workers, both in terms of geometry (length of upstream and downstream pipes equal to $100D$ and $80D$, respectively, bend angle 180° and $\gamma = 0.25$) and in terms of fluid dynamic conditions (air flow with inlet velocity of $w =$ 8.7 m/s)

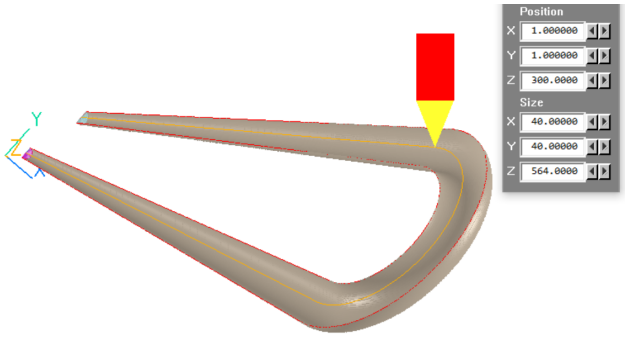

Figure 3.6: Overall view of the numerical setup.

3.2 Considerations of the development of flow upstream the bend

Sudo et al. claimed that the length of the upstream pipe in their setup, equal to $100D$, was sufficient to produce fully-developed flow at the entrance of the bend. In order to assess whether this occurred also in the numerical simulations, the development of the flow in the upstream sub-domain was investigated, making reference to the following variables, $uRMS$, W, and longitudinal pressure gradient in the position identified by the arrow in Fig.

3.7. The three physical quantities are plotted for the 100 diameters of the inlet straight segment in Fig. 3.8 where it is evident that they reach a stable value after approximately $50D$.

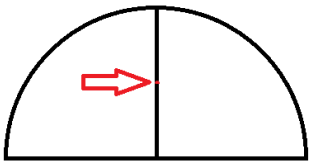

Figure 3.7: Position where the three variables were computed in any section of the inlet straight segment.

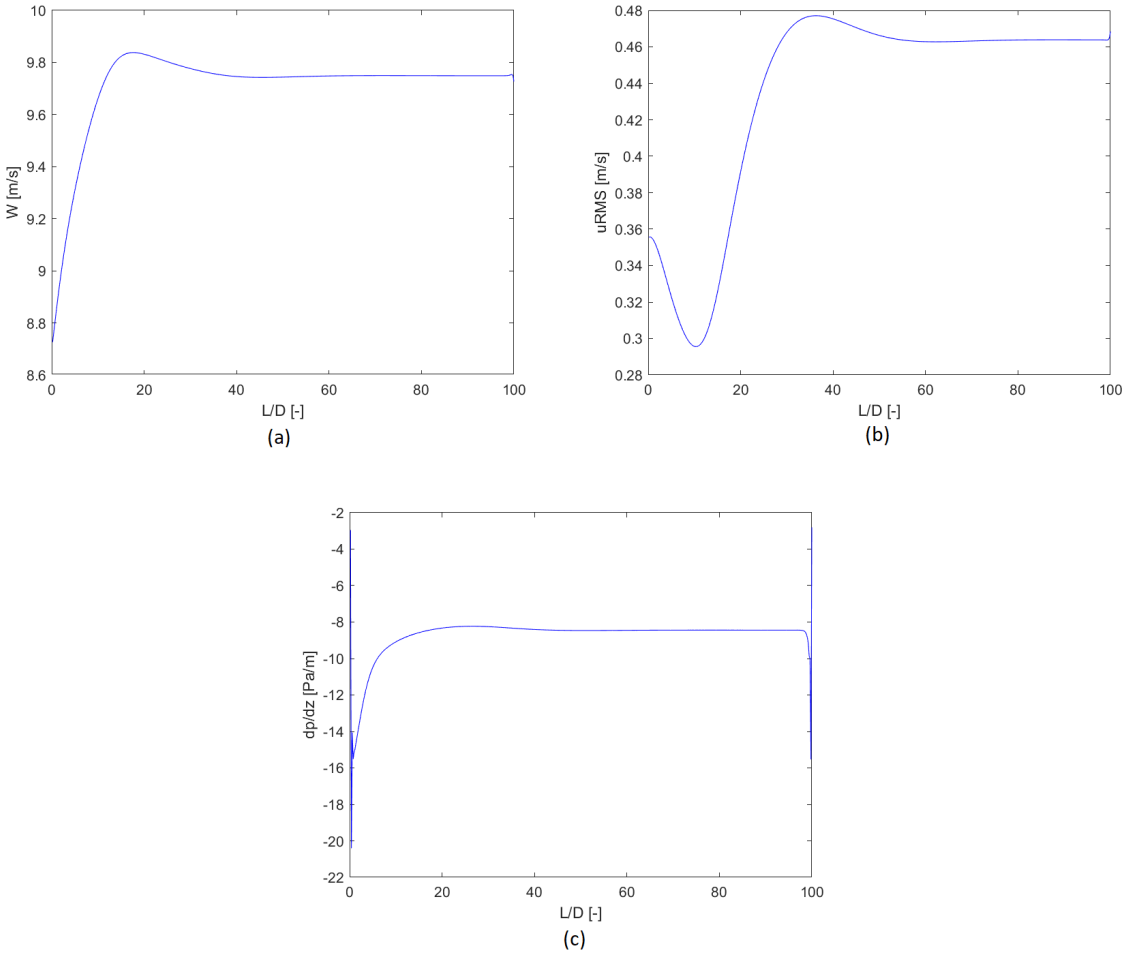

Figure 3.8: Analysis of flow development in the upstream pipe for the axial velocity W "a", $uRMS$ "b" and pressure gradient dp/dz "c"

The fact that the flow is fully developed ensures the independence of the solution inside the bend and downstream of it from the shape of the distribution of the fluid dynamic variables at the inlet section (z=0), here taken as rectangular. Noticing that the flow is fully developed also allows shortening the domain, producing two advantages. On the one hand, it makes it possible to reduce the reduce the number of cells keeping the same mesh refinement level, thereby reducing the computational effort. On the other, it allows increasing the mesh refinement level without increasing the overall number of cells, and, therefore, the computational burden. The second strategy was useful in the grid independence study, as described in Section 3.3.

3.3 Numerical convergence of the solution

In general terms, "numerical convergence" indicates that the approximate solution must approach the analytical one, which is unknown. In CFD, two inter-related aspects relate with the numerical convergence, namely, the iterative solution algorithm and the computational mesh.

3.3.1 Iterative solution algorithm

Whenever a job is launched, the software starts computing the fluid dynamic variables in all computational cells in an iterative process, which proceeds until either the maximum number of iterations or a threshold percentage residual is reached. Figure 3.9 shows an example of the PHOENICS windows that appears when the computation is running.

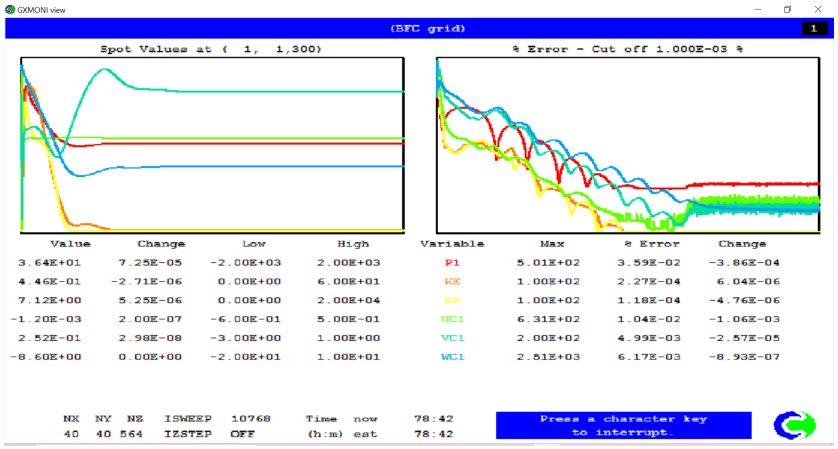

Figure 3.9: Communication window of PHOENICS when the simulation is running

In the bottom-left corner, the total number of cells NX NY NZ of the three directions are indicated. It is also possible to see the number of the current iteration next to the variable name ISWEEP, which is useful to realize how fast the computation proceeds in relation to the time of computation, which is also visible. In the top-left corner of the windows, the location of the monitoring probe, visible in Fig. 3.6, is indicated. The curves in the left-hand side plot are the values, at every iteration of the solution algorithm, of the fluid dynamic variables at probe position. The right chart represents the evolution of the residuals of all parameters. On top of this last graph there is the given convergence criterion value, so when all normalized residuals are lower or equal to this value the convergence is reached and the simulation is stopped. This two graphs are useful because they can help understanding in real time how the simulation is going. When the simulation is converging, on the left chart the values are becoming more stable on a given value, whereas on the right one the residuals are lowering more and more during the integration process. In the communication window presented here, which refers to the computational mesh called "Fine Grid" in the next sub-section, the convergence with the global convergence criterion was not reached because the residuals stop their diminishing trend and started oscillating close to a certain value. This is a typical behavior in CFD simulations, especially when either the flow or the geometry are relatively complex. In spite of this the simulation was successfully ended, since the residuals reached a sufficiently low value. Each row of the table provides the values, at the current iterations, of different parameters related with the same fluid dynamic variable. These parameters are indicated in the title of each column.

3.3.2 Grid sensitivity

In addition to verifying the convergence with respect to the iterations of the solution algorithm, it must be proved that the computational mesh chosen by the user is able to produce convergence towards a unique solution. This is achieved through a grid-independence study, aimed at demonstrating that the solution on a given mesh does not significantly change after further mesh refinement.

For this analysis, 4 different grids where employed. First of all, the domain is divided into four parts alongside the longitudinal coordinate, referred to as "a", "b", "c", d" in Fig. 3.10. This was made to achieve more flexibility in the definition of the mesh, by considering that different level of mesh refinement are needed according to the spatial rate of change of the physical variables, the higher the rate the finer the grid.

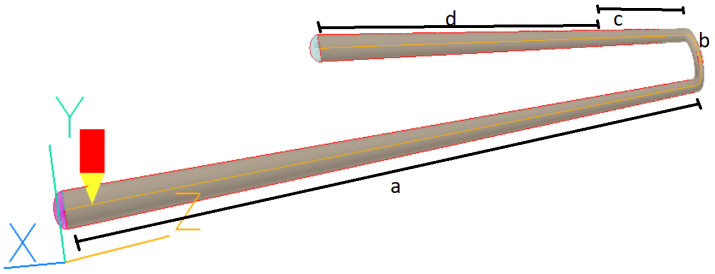

Figure 3.10: Identification of the four mesh regions

The region denominated as "a" corresponds the upstream straight segment and has a variable power ratio , which depends on the simulation. Region "b" includes the bend and it was always discretized with a uniform mesh (power ratio = 1). The same holds for region "c", which extends $10D$ downstream of the bend. The remaining part of the domain is included in zone "d" that has variable power ratio, which, in absolute terms, is always equal to that in zone "a". The topological characteristics of the meshes employed for the grid independence analysis are summarised in Table 3.1:

Grid refinement	**Nθ**	**Nr**	**Na**	**Nb**	**Nc**	**Nd**	**Nz**	**Ntot**	**P**	**Time [hours]**
Coarse grid	10	10	80	60	52	80	272	27200	1	2
Medium-coarse grid	20	20	140	120	100	140	500	200000	1	7.3
Medium-fine grid	30	30	40	180	160	40	420	378000	2.3	44
Fine grid	40	40	60	240	214	50	564	902400	2.3	62

Table 3.1: Characteristics of the different meshes for the grid independence analysis and approximate time of computation. The variable N indicates the number of subdivisions along direction θ, r, and z in each regions "a", "b", "c", d" in Fig. 3.10. The power P applies to region a and d, and it is negative in the former case, and positive in the latter one.

In order to analyze the grid independence of the solution, one needs to compare the same feature of the solution calculated on different meshes. If the value changes from one refinement to another, then the solution is grid dependent. When the difference of values from one grid to another is very small, that brings to state that this feature of the solution is not much sensitive to grid refinement and either of the two grids can be used for the computations without significant errors induced by the grid. The variable used to detect the sensitivity of the solution to the mesh are $URMS$, P, W and V. The position chosen is the diameter lying on the symmetry plane of the pipe, as shown in Fig. 3.11. The analysis has been made for three slabs along the streamwise direction, namely, at the entrance of the bend ($\varphi = 0°$), at half of the bend ($\varphi = 90°$), and at the exit of the bend ($\varphi = 180°$). The corresponding results are displayed in Figs. 3.12, 3.13, and 3.14, respectively.

Figure 3.11: The position where the physical quantities are computed is highlighted in red, intrados r_i (left), extrados r_o (right).

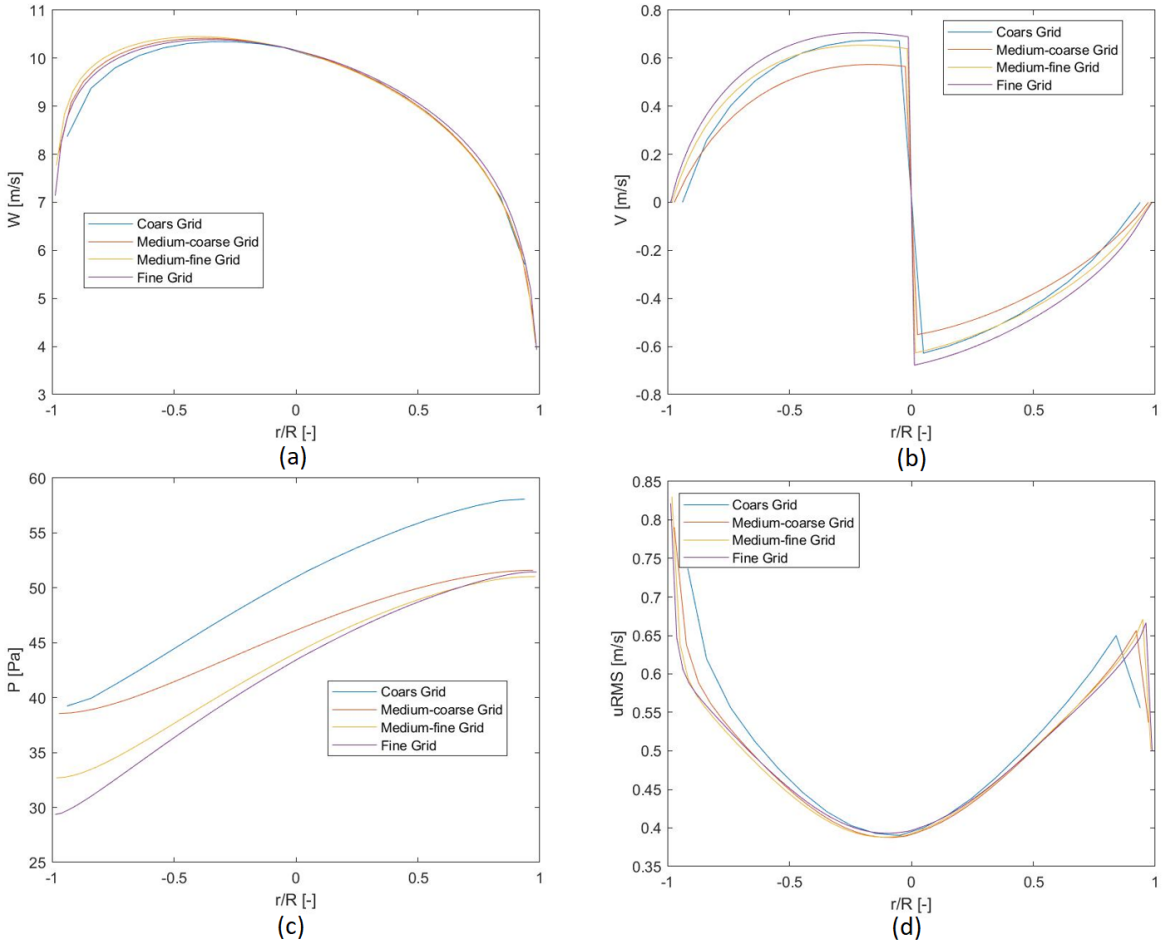

Figure 3.12: Grid independence study of "a" axial velocity W,"b" radial velocity V, "c" pressure P and "d" $uRMS$ on the symmetry segment of the pipe section (Fig. 3.11) at position $\varphi = 0°$

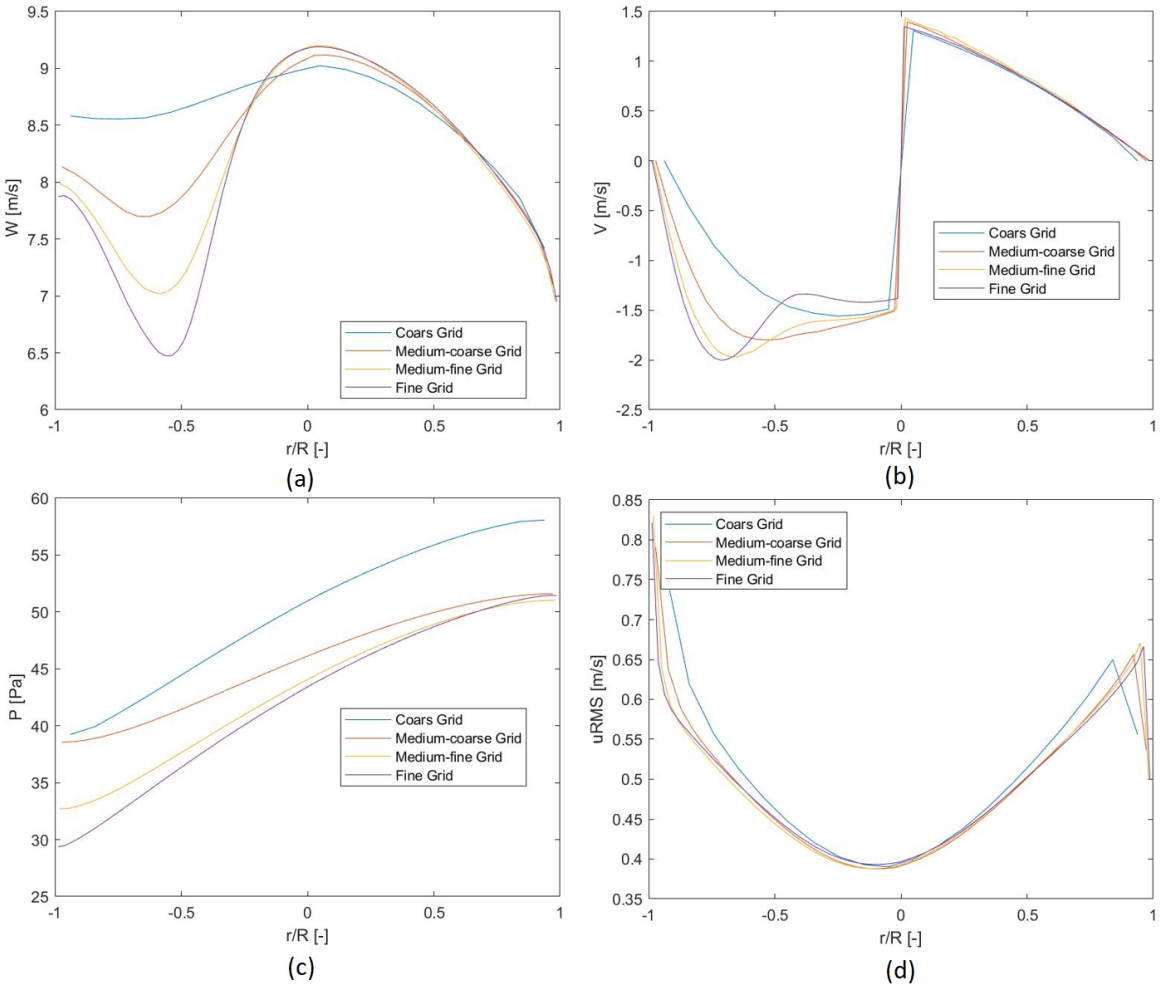

Figure 3.13: Grid independence study of "a" axial velocity W,"b" radial velocity V, "c" pressure P and "d" $uRMS$ on the symmetry segment of the pipe section (Fig. 3.11) at position $\varphi = 90°$

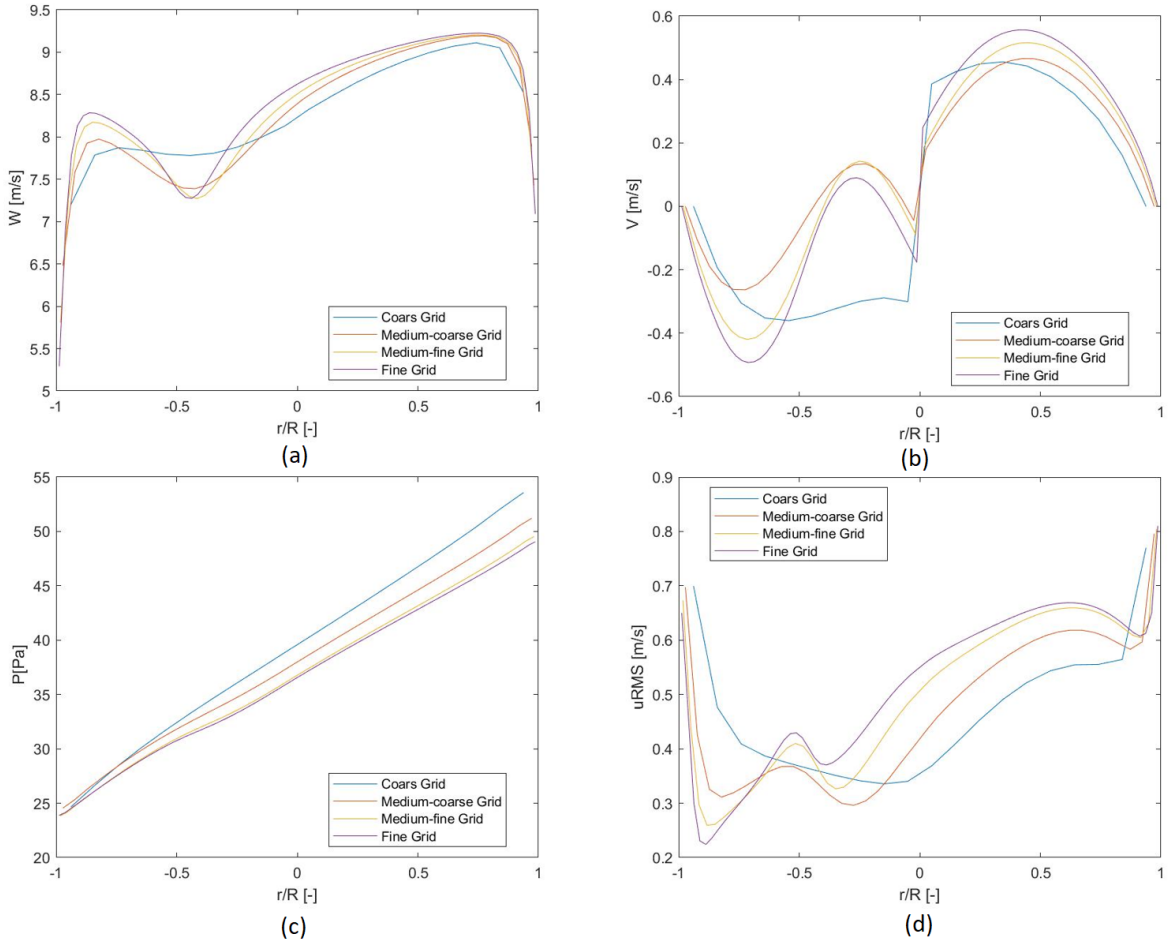

Figure 3.14: Grid independence study of "a" axial velocity W,"b" radial velocity V, "c" pressure P and "d" $uRMS$ on the symmetry segment of the pipe section (Fig. 3.11) at position $\varphi = 180°$

By looking at the plots, it is possible to draw a few consideration. In all the three slabs, the coarse grid gives values that are far too much different form those provided by the other grids and, thus, appears to be totally inadequate. The other three grids show a clear tendency towards grid-independence. In particular, the values computed employing the middle-fine grid and fine grid are generally rather close to each other, and non-negligible differences are observed only for the streamwise velocity W at $\varphi = 90°$. Considering that further mesh refinement was not possible owing to computational limitations, and that there is an difference of about 18 hours of calculation time between the two finest meshes, the remainder of the simulations were performed using the middle-fine grid, as this was judged a good

compromise between accuracy and computational burden.

3.4 Experimental validation

The validation of a CFD model consists in assessing the degree of agreement between the numerical solution and the experimental evidence for a certain case and limited to some measurable features of the flow. This section is dedicated to the comparison of CFD results obtained with the standard $k-\varepsilon$ model and the experimental data available from the study conducted by Sudo et al. [9]. On the grounds of the grid sensitivity study previously described, the numerical data used for the validation are those calculated on the medium-fine grid in Tab. 3.1. Since Sudo et al. [9] did not provide the measured variables in tabular format, it was necessary to infer these quantities from the graphs and figures provided by the authors.

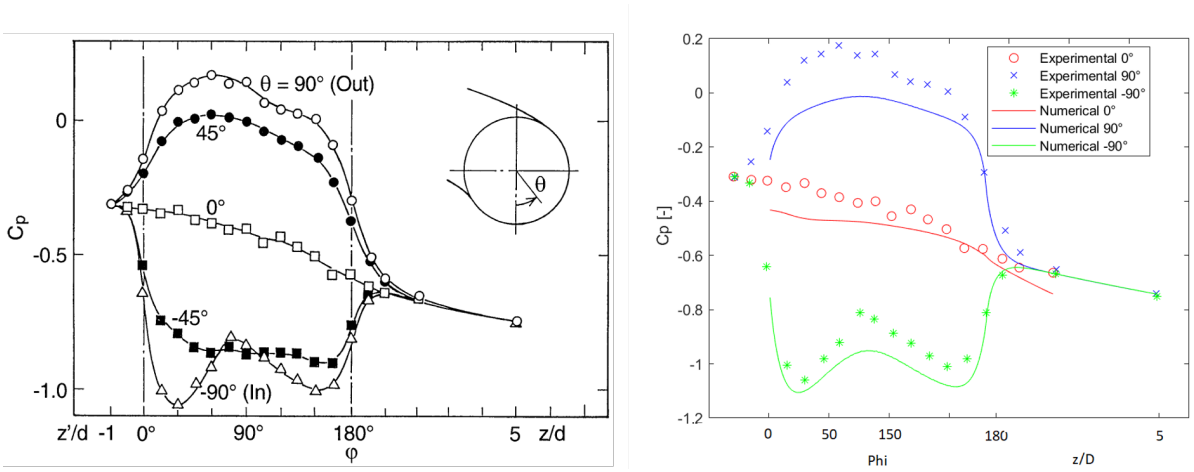

Figure 3.15: Wall static pressure coefficient C_p: experimental data measured by Sudo et al. [9] (left); numerical data with the superimposition of experimental data for three azimuthal positions (right).

Firstly, the wall static pressure was analyzed, referring to the pressure coefficient C_p (Eq. 1.3). The comparison was carried out form the entrance section of the bend $\varphi = 0$ pipe up to 5D after downstream of the bend for three azimuthal positions (that is, three values of θ) and $r = R$. The position $\theta = 90$ corresponds to the outer side (r_o), whereas the position $\theta = -90$ individuates the inner one (r_i). The curve for $\theta = 0$ is as displayed in the left plot in Fig. 3.15. Indeed, experimental data are available even 1D upstream of the bend, but, since the grid in that region was not uniformly distributed, an accurate comparison with experimental data was not possible

owing to the difficulties in estimating C_p in a specific axial location using the MATLAB post-processing routines available. For the same reason, it was not possible to find P_{ref} as the value at $\theta = 90°$ $17.6D$ upstream of the bend, as the experimenters did. Therefore, in the numerical simulations P_{ref} was tuned to have a perfect match between the numerical and experimental data $5D$ downstream of the bend at $\theta = 90°$. Generally, the three experimental curves agree quite well with with the experiments, although there is not a perfect overlap in the right plot in Fig. 3.15. Numerical data appear shifted downwards in respect to the numerical one, and this might also be attributed to the arbitrary choice of P_{ref} that operate a vertical translation on numerical data. Obviously, pressure is higher at the outer wall, so that a radial pressure gradient opposes to the centrifugal force. Additionally, looking at the curve for $\theta = 0°$, it is evident that both numerical and experimental individuate a decreasing trend, compliant with the fact that there is a loss of energy in the bend.

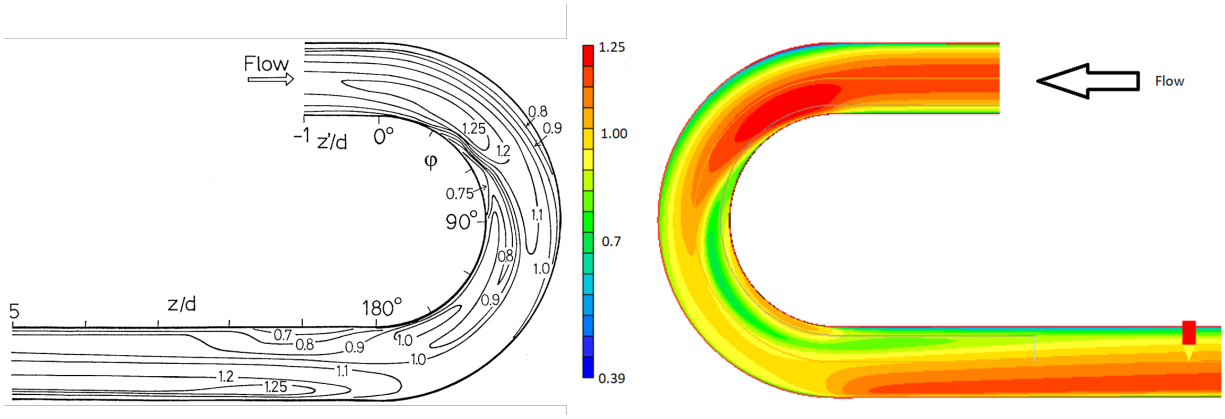

Figure 3.16: Contour plot of W/W_b in the symmetry plane of the system: experimental data measured by Sudo et al. [9] (left) on and numerical data calculated with PHOENICS (right).

Afterwards, a qualitatively comparison was made in terms of the longitudinal velocity W/W_b on the symmetry plane of the system. This was made starting from one pipe diameter upstream of the bend, where the flow is approximately fully developed and it does not practically perceive the influence of the bend, up to $5D$ upstream of the bend, where the monitoring probe is located, see Fig. 3.16. It is possible to observe that the flow is initially accelerating near the r_i side of the pipe from $\varphi = 0°$ until about $\varphi = 20°$. Afterwards, after that it starts heading towards the r_o side of the bend, though the highest velocity is still in the inner region of the bend. The numerical model predicts a low velocity close to the bend center-line from $\varphi = 90°$ and

$\varphi = 180°$ and faster velocities close to both external sides r_i and r_o. Once again, there is a good agreement between experimental and numerical.

It is convenient to analyse the flow in the bend through the joint analysis of Fig. 3.15 and Fig. 3.16. In fact, for $\theta = -90°$ (that is, the r_i side) and $0 < \varphi < 20°$, as the velocity is accelerating the pressure is dropping. Conversely, for larger φ the velocity close to the r_i side decreases, entailing a pressure increase until $\varphi = 90°$, where the W starts increasing again and the pressure decreases. This phenomenon is clearly visible from the "W" shape of the C_p for $\theta = -90°$ as a consequence of what previously aforementioned. Analogous considerations can be made for the velocity and pressure for $\theta = 90°$ in the r_o side of the bend.

Further comparison between experimental and numerical axial velocity data can be done by referring to three equally spaced cross-sections of the bend ($\varphi = 30°, 90°, 150°$). Experimental data taken from Sudo et al. [9] are depicted on the left side of Fig. 3.17, whereas the numerical data for the corresponding sections are shown on the right side are. All half pipe sections in these pictures have the left side corresponding to the inner side of the bend r_i and the r_o located on the right side. For pictures "a" and "b" ($\varphi = 30°$) there is a clear agreement between the measurements and the prediction of the numerical model. Both approaches well represent that, at this location, the flow velocity is accelerated close to r_i, and, as a matter of facts, the highest velocities are on the left side of the plots. Although the qualitative behaviour of the W/W_b map is in agreement with the experiments also for plot "c" and "d" ($\varphi = 90°$), the calculated distribution of W/W_b shows smoother variations and lower magnitude compared with the evidence. This might be due to the fact that the anisotropic nature of turbulence inside of the bend cannot be well captured by a turbulence model based on the Boussinesq assumption. Nonetheless, there is an other consideration that ought to be made, in that the experimental measurement are collected over a grid mesh that is finer close to the wall to better detect the changes in velocity in that region (Fig. 1.13). Conversely, the CFD simulations employed a uniform grid and, therefore, the abrupt changes in velocity close to the wall might be not accurately captured by the numerical model owing to the relatively coarse grid in that region. Analogous considerations can be made for the section at ($\varphi = 150°$) by inspecting plots "e" and "f" in Fig. 3.17.

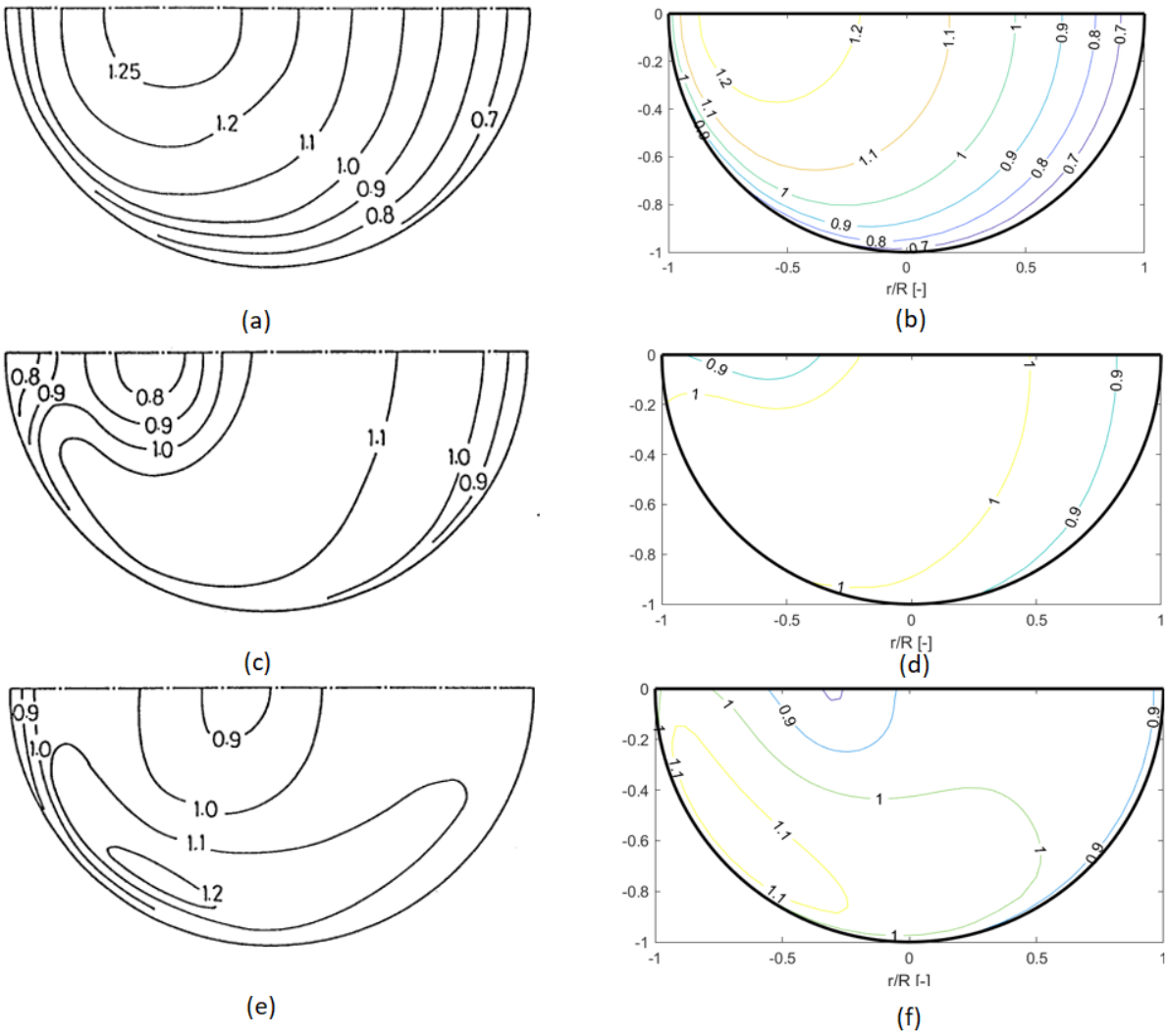

Figure 3.17: Contours of W/W_b over three cross-sections of the bend: experimental data measured by Sudo et al. [9] (a,c,d) and numerical data (b,d,f). The left sides of each section correspond to the inner wall r_i , and "a" and "b" stand for section $\varphi = 30°$; "b" and "c" stand for section $\varphi = 90°$; "d" and "e" stand for section $\varphi = 150°$.

Attention was then turned to other fluid dynamic characteristics related with the velocity field, namely, the time-averaged secondary flows and the velocity fluctuations. In a first stage of the work, reference was made to the cross-section averaged parameters I_s and k_a, already defined in paragraph 1.1. The calculated and measured streamwise profiles of these variables are shown in Fig. 3.18. The first parameter is an indicator of the intensity of the secondary flow of the whole section. The CFD model underestimates I_s, but the trend is qualitatively the same of the experimental data, exclud-

ing the small peak observed numerically at the end of the bend which is worthy of further investigation, and it might be due to some post-processing issues. The parameter k_a represents the average level of turbulence in a given section. From a qualitative point of view, the numerical and experimental results evidence a similar trend. However, the CFD model underestimates the turbulence level and its pick is located a bit further downstream from the inlet section compared to the experimental observation. The underestimation of k_a produced by the standard $k - \varepsilon$ turbulence model might be produced by the fact that this model relies on the assumption of isotropic turbulence when in reality turbulence in the bend is strongly anisotropic.

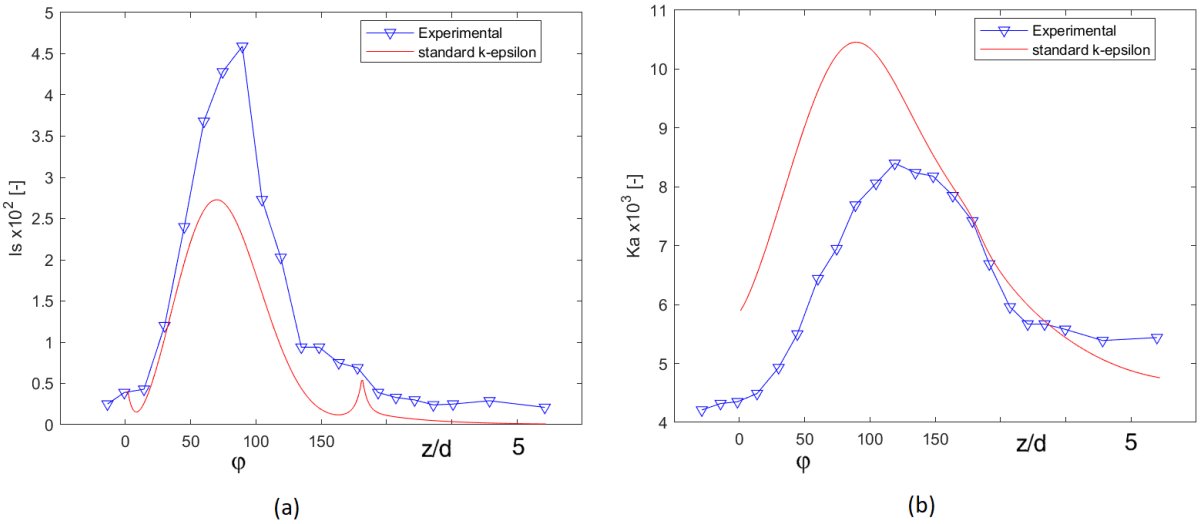

Figure 3.18: Graphs "a" and "b" represent the profiles of I_s and k_a, as experimentally determined by Sudo et al. [9] and calculated from the CFD simulation.

The parameter I_s provides information on the magnitude of the secondary flow phenomenon, but it does not provide any information of the spatial distribution cross-section velocities U and V. In order to have a better idea of the direction of U and V, reference could be made to Fig. 3.19, which is the analogous of Fig. 3.17 for the cross-plane mean velocity vectors. From a qualitative point of view, plot "b" qualitatively well represents the direction of the secondary flow but, due to the absence of any legend giving information on the magnitude of the velocities in plot "a", no quantitative conclusion can be obtained. The same consideration can be made for plots "c" and "d", where the in-plane vortex is well developed and clearly visible. Instead in picture "f", it is possible to see a second vortex close to the symmetry pipe plane and slightly on the left side of the pipe center-line. The existence of

such second vortex has been mentioned in Paragraph 1.3.5 by Anwer et al. [5], but this is not visible in the experimental measurement of of Sudo et al. [9] (picture "e"), probably also because the resolution of the experimental grid is too coarse.

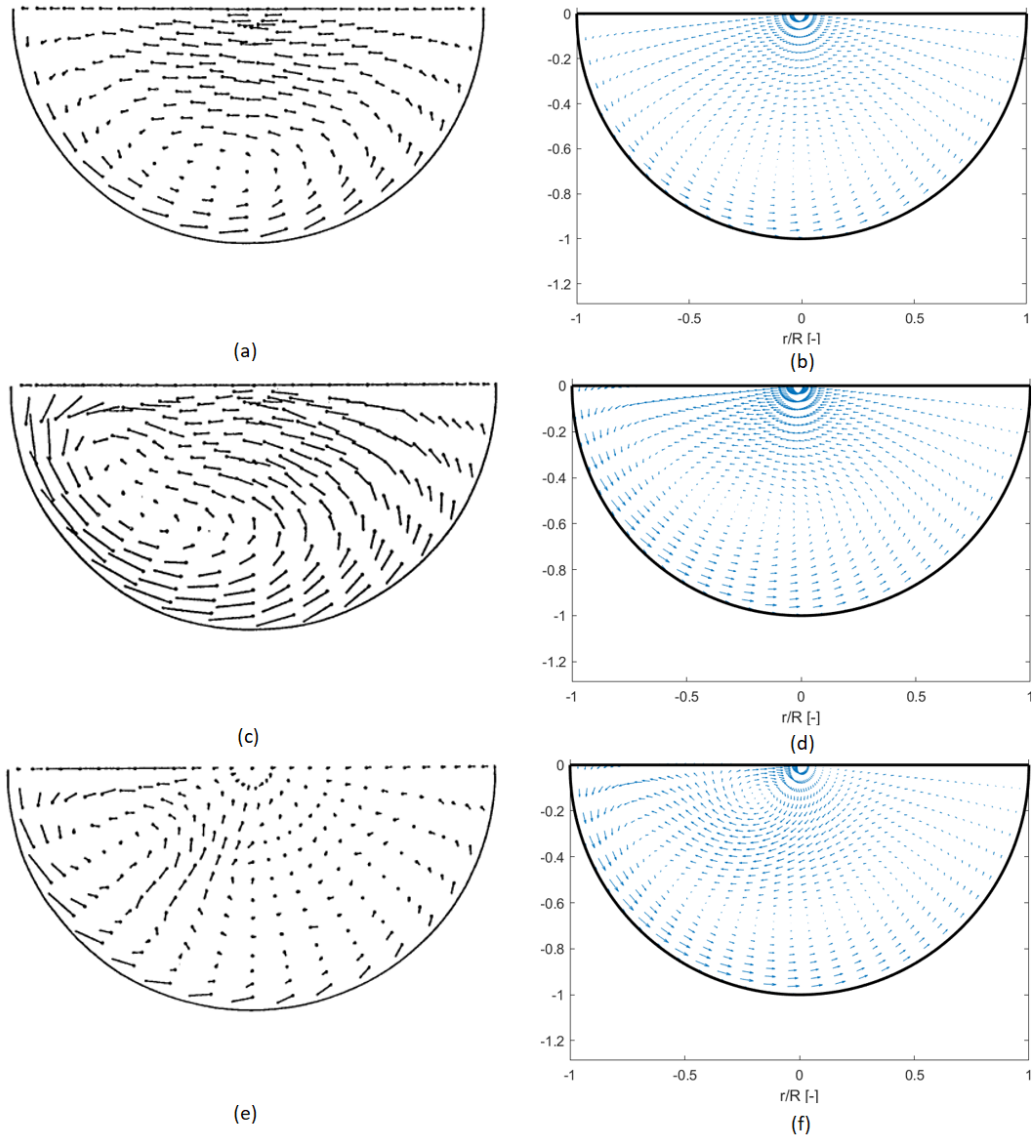

Figure 3.19: The same as Fig. 3.17 for the in-plane velocity vectors.

Finally, Fig. 3.20 is the analogous of Figs. 3.17 and 3.19 for the longitudinal fluctuating velocity. Note that the plots in the right-hand side show the $uRMS/W_b$ ratio. This is a consequence of the use of the $k-\varepsilon$ turbu-

lence model and its underlying assumption of isotropic turbulence. Although the qualitative map of the iso-lines show similarities between experiments an computations, there is a rather poor agreement between the measurements and the numerical data. In particular, the CFD model fails in capturing the existence of a high turbulence region close to the inner wall. Such poor agreement, interpreted as a consequence of the use of the $k - \varepsilon$ turbulence model, has correspondence with the fact that, as already observed, also the cross-averaged parameter k_a was underestimated.

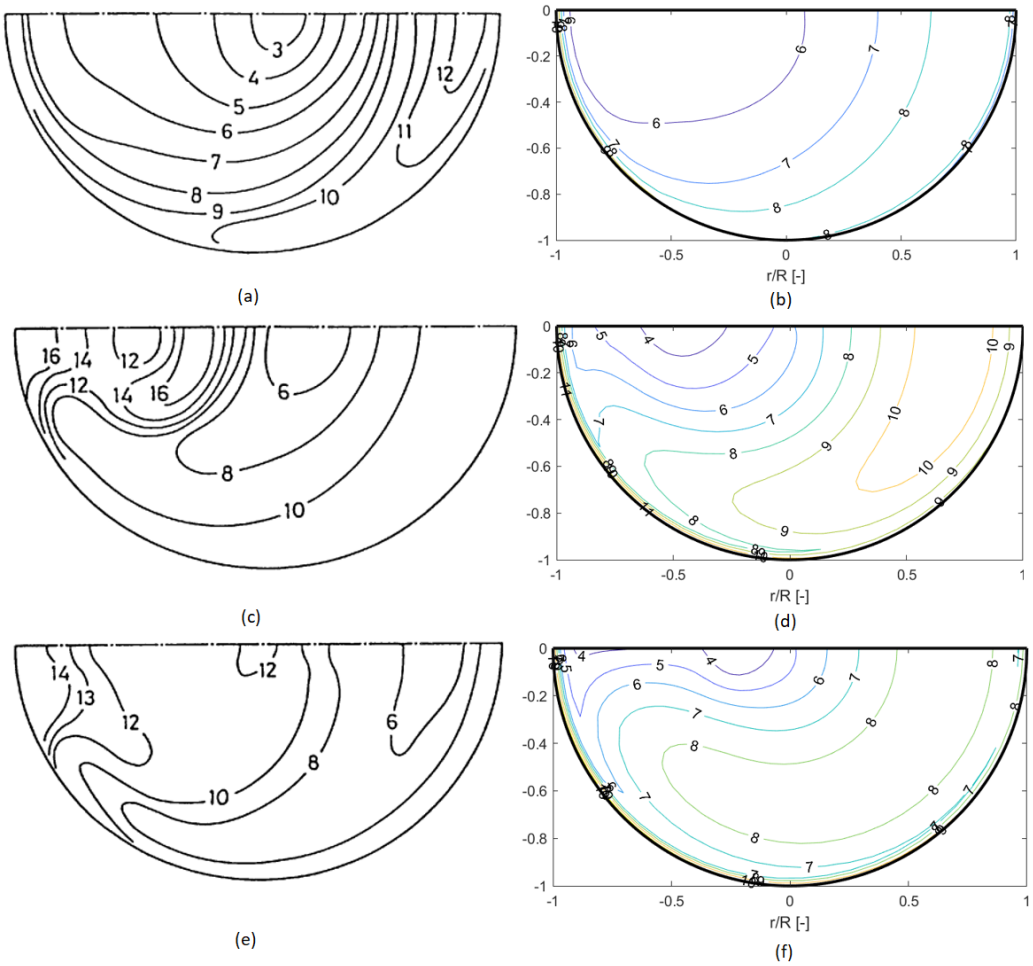

Figure 3.20: The same as Fig. 3.17 for the normalized fluctuating velocity, directly provided by Sudo et al. [8] and estimated as $uRMS/W_b$ in the numerical calculations.

3.5 Optimization of the computational domain

The duration of a CFD simulations depends on many factors including the extension of the domain, the choice of the grid, and the number of solved variables in each element of the domain. It is evident that, if the number of grid cells increases, the computational time for each iteration will accordingly rise. However, a less intuitive behavior was also observed, that is, when simulating two cases which differ from each other because one has an additional part added to the geometry, the case with a larger domain size took much more time to converge, even if the number of cells are the same. The time to reach convergence is also dependent upon the choice of the turbulence model: the convergence, in fact, may take less or more time because one model is more appropriate than the other as well as because one model has more parameters to compute than another.

In the experiment of Sudo et al. [9], the length of the pipe upstream of the bend was $100D$. Such a size guarantees a fully developed flow $1D$ before the bend entrance. From the findings in Section 3.2, it is evident that flow is already fully developed about $50D$ downstream of the inlet section, so there is no convenience in keeping an upstream length of $100D$. Based on the considerations drawn above, the numerical setup could be improved from the point of view of the computational cost by halving the first straight segment from its original dimension.

To have the certainty of acting right, further testing was carried out to ensure that the shortening in the length of the upstream pipe would bring benefits in terms of computational time without altering the behaviour of the fluid at the entrance of the pipe. Two different runs were compared. They have the exact same number of grid cells and the same turbulence model ($k-\varepsilon$ standard), but the first simulates $100D$ upstream of the bend whereas the other only $50D$. The values of the $uRMS$, P, W and V, over the red segment showed in Fig. 3.11 in the slab at φ=0° are compared. The characteristics of the meshes used in the two simulations are reported in Table 3.2 and the graphs of the four variables taken into consideration are displayed in Fig. 3.21

Lz	**Nteta**	**Nr**	**Na**	**Nb**	**Nc**	**Nd**	**Nz**	**Ntot**	**P.**	**Time [hours]**
100 D	30	30	40	180	160	40	420	378000	2	≈ 25
50 D	30	30	40	180	160	40	420	378000	2.3	≈ 10

Table 3.2: The simulation grid features

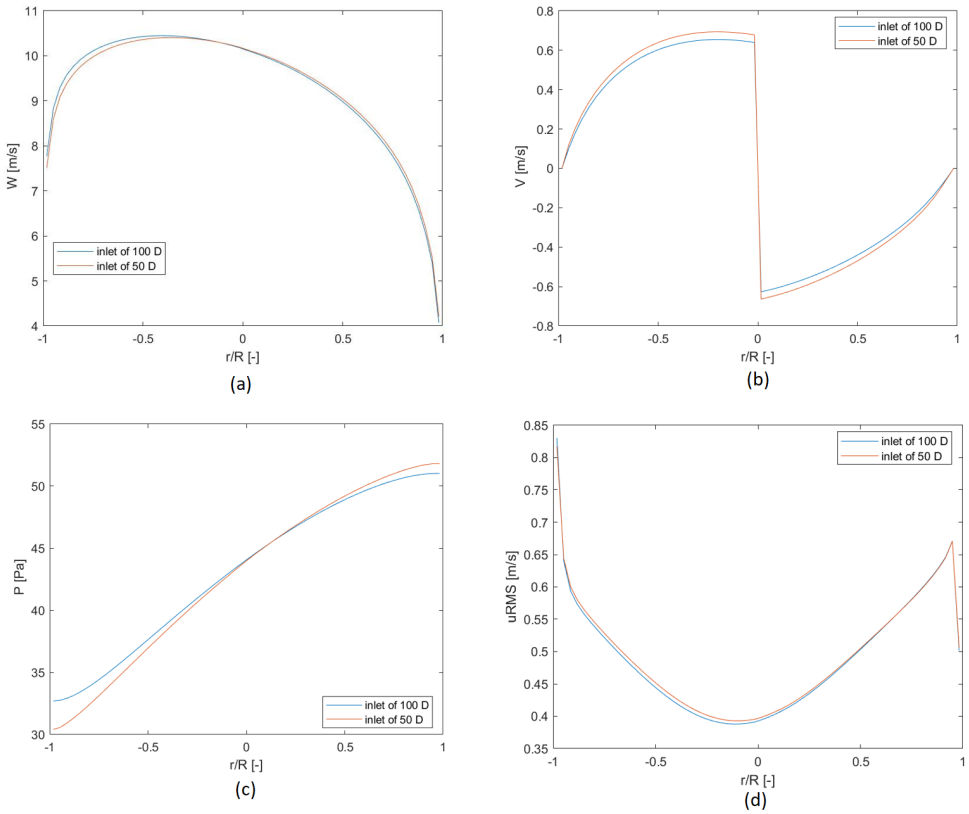

Figure 3.21: Comparison of the values of "a" W, "b" V, "c" P and $uRMS$o n the symmetry segment of the pipe section in position $\varphi = 0°$

The plots in Fig. 3.21 confirm that the solutions obtained with $100D$ and $50D$ length of the inlet straight segment are very similar to each other. The relative small differences may be attributed to the different mesh power ratio rather then to the different length of the upstream pipe. In fact, the section with $\varphi = 0°$ already perceives the presence of the bend and the cells just upstream to that section have different sizes in the z direction, thus probably giving rise to the small differences observed in the solution.

The advantage of using a smaller domain is very evident from the considerable reduction in the computational time. This was very surprising, since the number of cells is exactly the same between the two cases. A possible interpretation was that a higher mesh power ratio allows for a more gradual change of the mesh size across the inlet section of the bend and this, in turn, helps to reach the convergence faster. Another possible interpretation is that the under-relaxation factors sets automatically by PHOENICS, which have a direct impact on the convergence speed, do depend on some features of the computational mesh such as the physical size of the cells and their aspect

ratio. Both interpretations are worthy of further investigation, but this was demanded to future work. At present, it was simply decided to run all subsequent simulations with $50D$ of straight pipe upstream the bend and power ratios $|power|>2.2$.

3.6 Sensitivity upon the turbulence model

Focus of this paragraph is the sensitivity of the numerical solution upon the choice of the turbulence model. Reference was made to four other turbulence models: RNG $k-\varepsilon$, Realisable $k-\varepsilon$, $k-\omega$ Wilcox 1988, $k-\omega$ SST.

The computational mesh is the same as previously defined. No additional grid sensitivity analyses were made, but on the grounds of the grid independence study performed when using the $k-\varepsilon$ standard model, using a grid analogous to the "fine" (Tab. 3.1) one appeared a choice on the safe-side. The only exception was made for the $k-\omega$ SST, which did not converge with the fine grid. In that case, the medium fine grid was used. The characteristics of the grids employed for each model are summarized in Table 3.3.

Turbulence model	**Nθ**	**Nr**	**Na**	**Nb**	**Nc**	**Nd**	**Nz**	**Ntot**	**P.**
RNG $k-\varepsilon$	40	40	60	240	214	50	564	902400	2.3
Realisable $k-\varepsilon$	40	40	60	240	214	50	564	902400	2.3
$k-\omega$ Wilcox (1988)	40	40	60	240	214	50	564	902400	2.4
$k-\omega$ SST	30	30	70	180	160	49	459	413100	2.4

Table 3.3: Characteristics of the grids used in the simulation with different turbulence models

The first parameter subject of investigation was the dimensionless pressure coefficient C_p, calculated as explained in paragraph 3.4. As shown in Fig. 3.22, the results with the four models differ from each other only very slightly. The green line in Fig. 3.22, corresponding to the RNG $k-\varepsilon$, is the closest to the experimental data for both $\theta = 90°$ and $\theta = -90°$.

In Fig. 3.23, the countours of the streamwise velocity, normalized by the bulk-mean velocity, are shown on the symmetry plane of the pipe, in order to detect macroscopic differences among the predictions of the 4 turbulence models in respect to the experimental data of Fig. 3.16. In plots "a","b" and "d", the dimensionless maximum velocity reaches 1.24, which is quite close to the experimental 1.25. In particular, in picture "a" (RNG $k-\varepsilon$), downstream of the bend the W distribution is very similar to the experimental

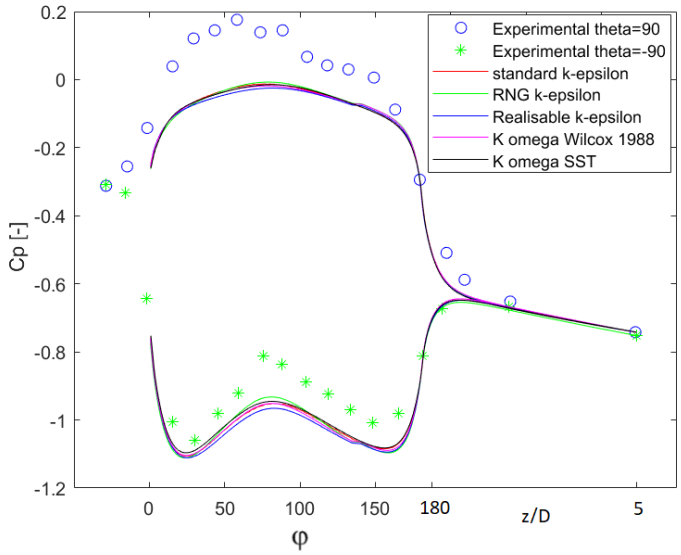

Figure 3.22: Comparison of 5 turbulence models with the experimental data of Sudo et al. [9] analysing the static wall pressure expressed in terms of pressure coefficients C_p.

one, whereas, in picture "b" (Realizable $k-\varepsilon$), the velocity is underestimated in that region. In picture "d" ($k-\omega$ Wilcox 1988), the high velocity region undergoes expansion downstream of the bend, in contradiction with experimental data. Keeping as a benchmark Fig. 3.16 among the four and picture "a" (RNG $k-\varepsilon$) best represent the experimental data.

The attention was then turned to the secondary flows, and, initially, reference was made to the cross-section average parameter I_s. The experimental data in Fig. 3.24 indicate a stronger intensity of secondary flow compared to all numerical predictions. All turbulence models not only underestimate the intensity of the secondary flow, but also the location where the pick occurs. They all predict a smaller pick at $\varphi = 75°$, whereas the experimental data show a higher pick at $\varphi = 90°$. Starting from $\varphi = 0°$, all models predict a slight decrease in the intensity of secondary flow until about $\varphi = 20°$; I_s starts increasing again afterwards. Although no validation can be made regarding this behavior, since no experimental data are available between $\varphi = 0°$ and $\varphi = 30°$, some interpretation can be argued by looking at pictures "a" and "b" of Fig. 1.18, which represent the experimentally-determined in-plane velocity vectors. At $\varphi = 0°$, all vectors are pointing towards the r_o side of the bend, whereas, at $\varphi = 30°$ the vectors are pointing towards the r_i side. The inversion of direction ought to be gradual between $\varphi = 0°$ and $\varphi = 30°$, hence, at $\varphi = 20°$ the secondary flow is very weak. As to the second smaller pick of I_s close to $\varphi = 180°$ finds a numerical interpretation and contradicts the ex-

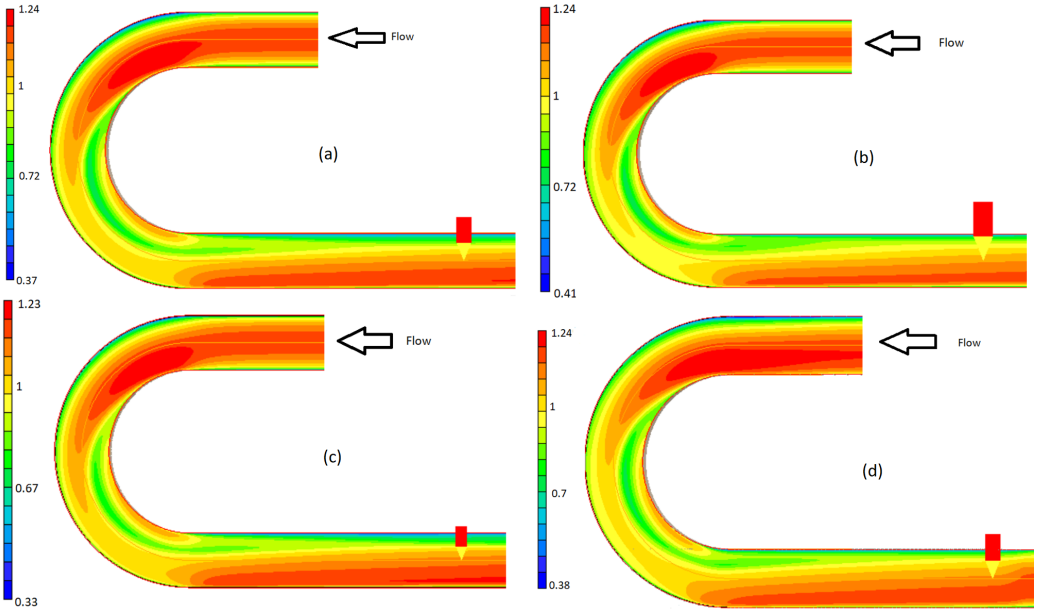

Figure 3.23: W/W_b dimensionless velocity on the pipe symmetry plane for the following turbulence models: "a" RNG $k-\varepsilon$; "b" Realisable $k-\varepsilon$; "c" $k-\omega$ SST ; "d" $k-\omega$ Wilcox 1988; The probe is positioned 5D downstream of the bend.

perimental data that show a constant drop of the I_s. The numerical solution of the secondary flow measured by I_s from section $\varphi = 130°$ diminishes until $\varphi = 160°$, where the in-plane velocities are small, and then increases again as the cross section velocities increase their modulus until $\varphi = 180°$, see Fig. 3.25. The cusp shape of the pick and the position corresponding to change from toroidal and cylindrical coordinates suggest that the problem may be either of the numerical solution (numerical instability), a physical solution would have a smoother shape. Once again, the RNG $k-\varepsilon$ is the turbulence model that produces the closest agreement with the experimental data.

The last parameter subject of investigation is k_a, which quantifies the cross-section averaged turbulence intensity. None of the models is able to reproduce accurately the trend of k_a detected experimentally by of Sudo et al. [9]. Nonetheless, there is agreement with experiments in terms of the order of magnitude of k_a and the qualitative behavior of the curve, in which an initial increase is followed by a decrease, with just one maximum. All turbulence models predict a higher intensity of turbulence compared with the experimental data starting from the $\varphi = 0°$ (Fig. 3.26). All models overestimate the decay of turbulence intensity downstream of the bend. The model that performs better than the others, and gives a solution with similarities with the experimental data is the RNG $k-\varepsilon$. Note that all turbulence models

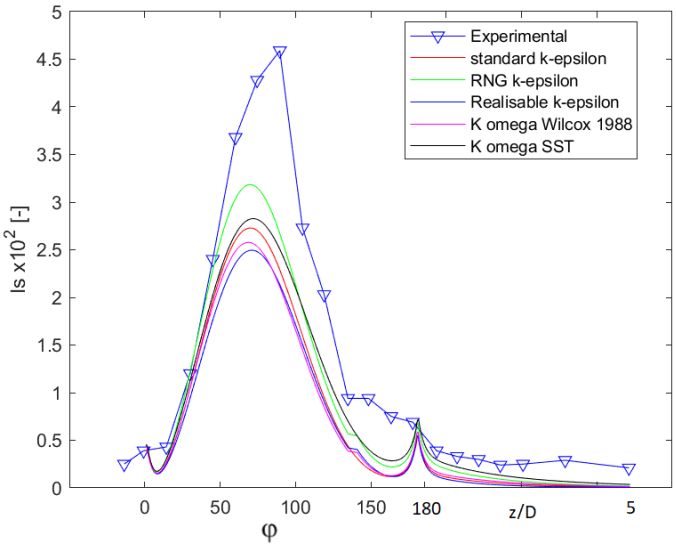

Figure 3.24: Comparison of 5 turbulence models with experimental data from Sudo et al. [9]: analysis of the intensity of the secondary flow by referring to the I_s parameter.

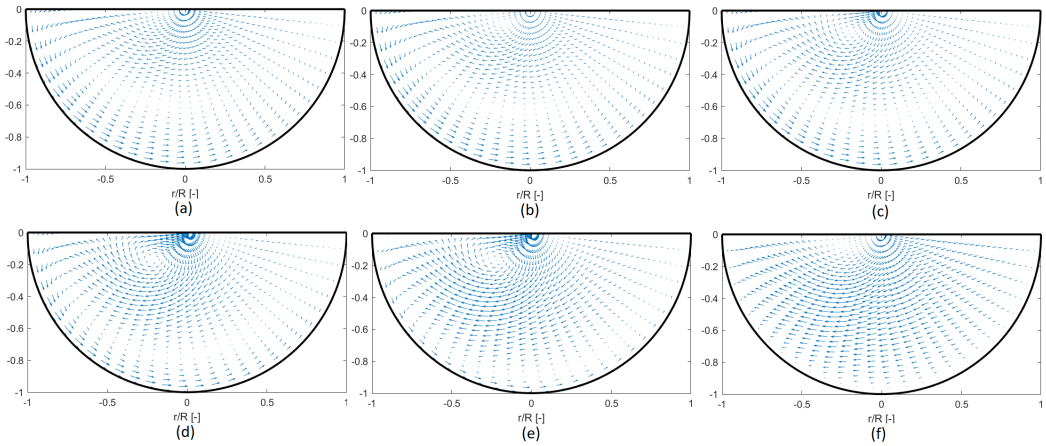

Figure 3.25: Cross section velocities from the simulation with standard $k-\varepsilon$ turbulence model and middle fine grid for section: "a" $\varphi = 130$; "b" $\varphi = 140$; "c" $\varphi = 150$; "d" $\varphi = 160$; "e" $\varphi = 170$; "f" $\varphi = 180$;

used in this study rely on the Boussinesq assumption, which is not suitable to model the anisotropic behaviour of turbulence which occurs inside of a bend and downstream of it. Therefore, it is not surprising to see that no perfect agreement between experiments and computations was obtained.

In the next chapter, the validation will be extended to other experiments. Based on the findings of the sensitivity analysis presented here, use will be

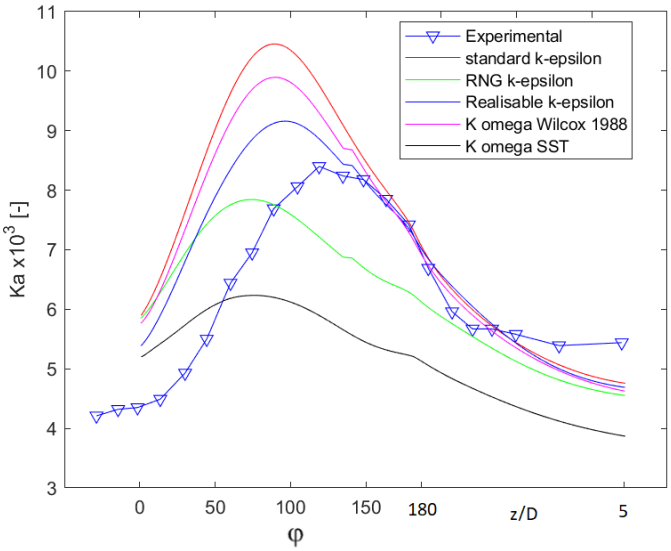

Figure 3.26: Comparison of 5 turbulence models with experimental data of Sudo et al. [9]: a analysis of the intensity of turbulence by referring to the k_a parameter.

made of the RNG $k-\varepsilon$ turbulence model, to further assess whether, in spite of its simple assumptions, this model allows capturing the main features of turbulence flows in pipe bends.

Chapter 4

Extension of the validation to other experimental conditions

In this chapter, the validation was extended to two other experimental tests available in literature and both referred to pipe bends with $\Phi = 90°$. The first set of experimental data was acquired by Sudo et al. [8]. The second is reported in a paper written by Enayet et al. [3]. The numerical simulations were carried out taking into account all the expertise acquired in Chapter 3.

4.1 Numerical simulation of the experiment by Sudo et al. [8]

Sudo et al. [8] performed an experiment on a bend with $\Phi = 90°$ having the same R, γ, and upstream and downstream pipe lengths of the case already considered in Chapter 3. As a result, there was no need to make any additional simulation to find the minimum upstream length that guaranties the condition of fully developed flow. The upstream straight pipe length was set to 50D because it guarantees a fully developed flow. All other parameters used in the numerical simulation were kept the same as reported in the paper of Sudo et al. [8]. For the definition of the grid, the pipe was subdivided in 4 parts along the streamwise direction (50D of straight pipe, 90° bend, 5D of straight pipe, and additional 35D of straight pipe). These partitions are indicated by the letters "a","b","c","d", respectively.The topological characteristics of the meshes employed are summarised in Table 4.1. The power ratio is applied only in regions "a" and "b", and limited to the longitudinal direction. The turbulence model chosen to carry out the simulation was the RNG $k - \varepsilon$, as this was found to provide the best agreement with the

experimental data for the case treated in Chapter 3.

Nθ	**Nr**	**Na**	**Nb**	**Nc**	**Nd**	**Nz**	**Ntot**	**|P.|**
40	40	90	120	214	72	496	793600	2.2

Table 4.1: The same as Tab. 3.1 for the experiment of Sudo et al. [8]

The wall static pressure numerical predictions along the regions "b" and "c" (covering the 90° bend and 5D of straight pipe downstream of it) are displayed in the right part of Fig. 4.1 and the experimental data are present on the left. Reference was made to the dimensionless pressure coefficient C_p, and, in this case, P_{ref} was determined in such a way to have perfect superposition between experimental and numerical solutions in the point individuated by the coordinates: $r = R$, $\theta = 0°$, and $\varphi = 90°$.

Good agreement between the predicted and measured solutions was found inside the bend, whereas, just downstream of it, the numerical solution underestimates the pressure losses occurring because of the secondary flow vortexes. As it will be further discussed later in this section (plot "a" in Fig. 4.3), in region "c" the intensity of secondary flow predicted by the model is weaker than the experimental one.

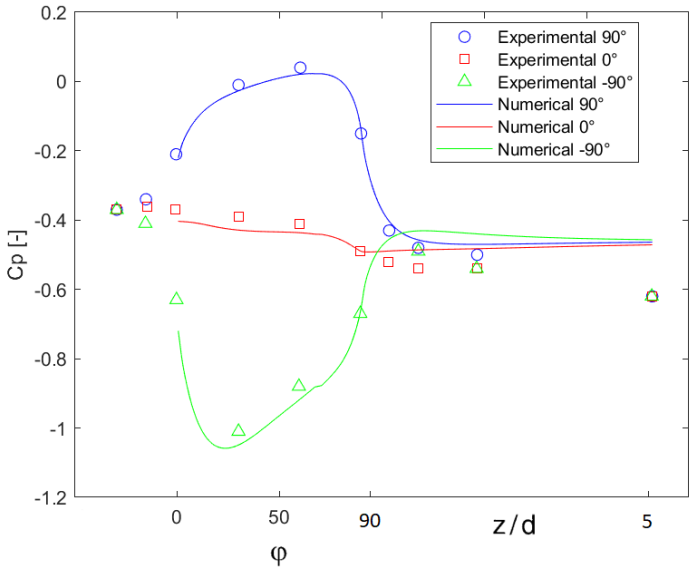

Figure 4.1: Wall static pressure coefficient C_p: experimental data measured by Sudo et al. [8] superimposed with numerical data for three azimuthal positions.

The normalized axial velocity W/W_b contour lines in the half section of the pipe are also considered for the comparison between the experimental

data (left) and numerical one (right) in Fig. 4.2. There is a very good agreement between the isotaches displayed in plot "a" and "b" ($\varphi = 30°$). Such agreement slightly worsen in the two downstream section ($\varphi = 60°, 90°$) "c" ,"d", "e" and "f", even if the numerical solution well matches the experiment from a qualitative point of view. In particular, in the numerical solution, the changes in axial velocity magnitude are less abrupt and more gradual, as it can be inferred from the fact that the contour lines are smoother in the sections on the right (Fig. 4.2).

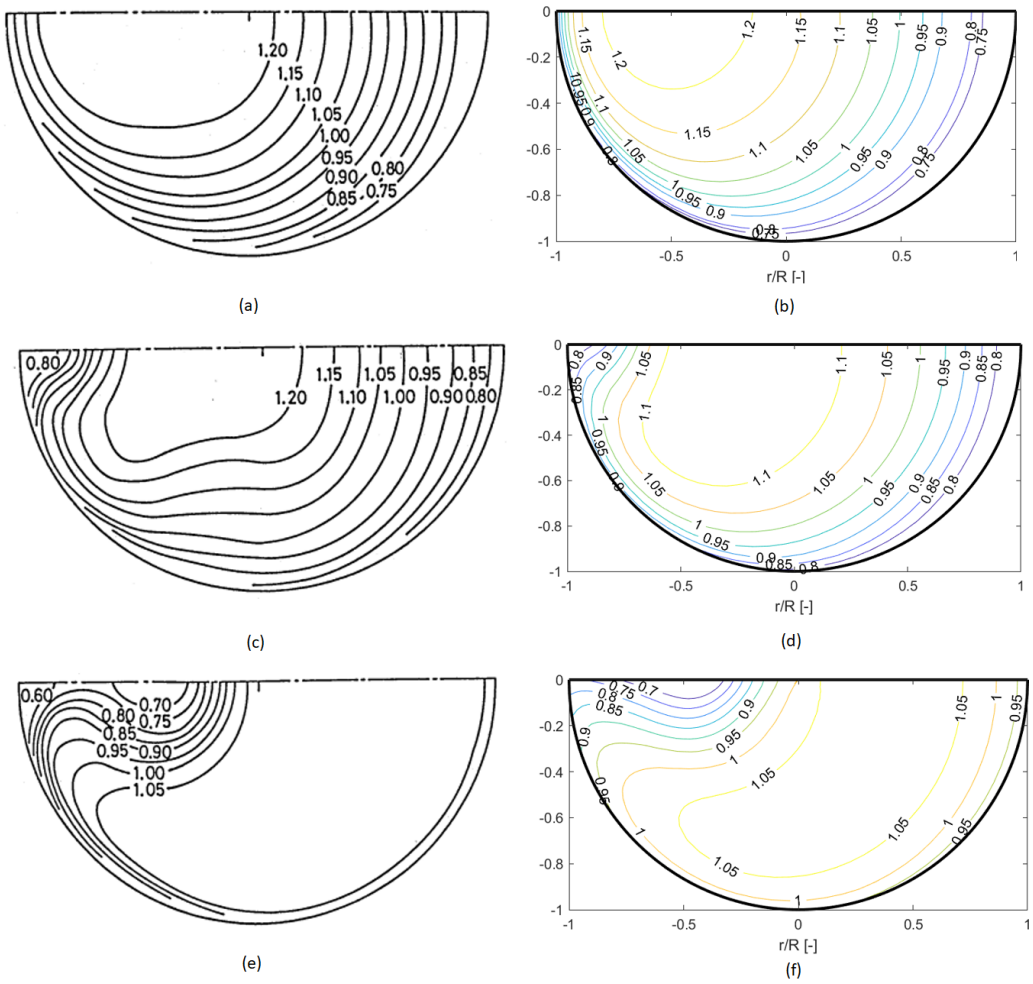

Figure 4.2: Contours of W/W_b over three cross-section of the bend: experimental data measured by Sudo et al [8] (a,c,d) and numerical data (b,d,f). the left sides of each section correspond to the inner wall r_i, and "a" and "b" for section $\varphi = 30°$; "b" and "c" stand for section $\varphi = 60°$; "d" and "e" stand for section $\varphi = 90°$.

The integral, non-dimensional parameters that measure the intensity of

secondary (I_s) and the intensity of the turbulence (k_a) show qualitatively similar behaviors for the numerical and the experimental data, although evident deviations are observed from a quantitative point of view. The spatial evolution of I_s predicted by the the $RNG\ k-\varepsilon$ turbulence model underestimates the experimental data. In the first part ($0° < \varphi < 60°$), the behavior of I_s is very similar to the one calculated for the $\Phi = 180°$ bend (Fig. 3.18), with an initial decrease of I_s followed by its subsequent increase. As in the case $\Phi = 180°$, just close to the bend exit I_s shows a small cusp. The cusp was detected in the numerical data only. Although the resolution of the experimental point is not fine enough to prove its existence, the cusp seems to be a spurious consequence of the numerical setup and the post-processing of the CFD solution. The cusp is detected exactly where the grid changes its topological features (from toroidal to cylindrical polar). Also for the parameter k_a, the numerical solution appears to anticipate trend observed experimentally, showing the same pattern discussed in Chapter 3 for the $\Phi = 180°$ bend.

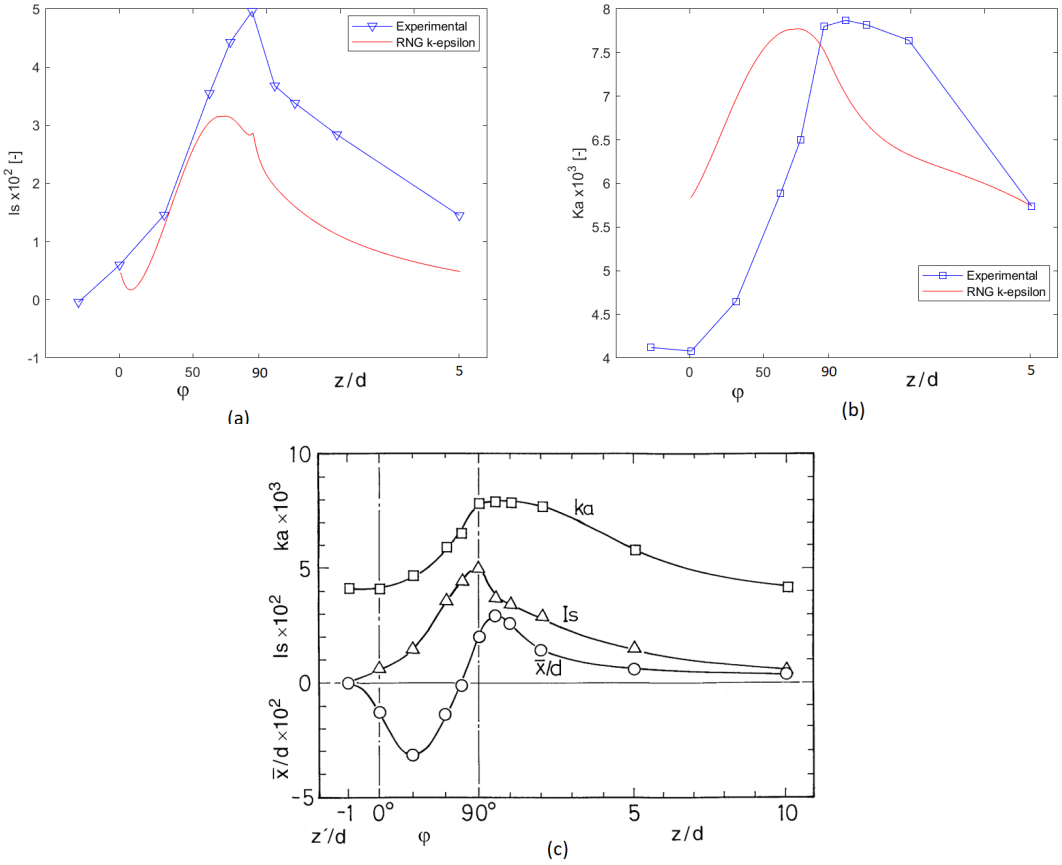

Figure 4.3: The graphs at the top "a" and "b" represent the profiles of k_a and I_a, as experimentally determined by Sudo et al. [8] and calculated from the CFD simulation. the bottom plot "c" is the original figure from the paper by Sudo et al. [8]

The plane view of the secondary flows taking place in the bend is represented by the aid of the cross-plane mean velocity vectors in Fig. 4.4. The first two pictures "b" and "d" form the numerical simulation show a nice agreement with the experimental measurements in pictures "a" and "b". Conversely, picture "e" shows a clockwise vortex, whereas picture "f" shows a counter-clockwise vortex with the same topology and magnitude. This deviation was completely unexpected, and, after careful thinking, it could not be excluded that it arose from an editorial mistake. In fact: (i) the paper by Sudo et al. [8] contains nine cross-plane velocity maps, and picture "e" is the only one in which the vortex is clockwise; (ii) if a local change in the direction of rotation of the vortex were actually present, its existence would have some effect on the curves of k_a and I_a; (iii) in the 180° bend case, the vortex is counter-clockwise in the section at 90°. In conclusion, apart from this unclear aspect regarding picture "e", the agreement between numerical

and experimental data is very good.

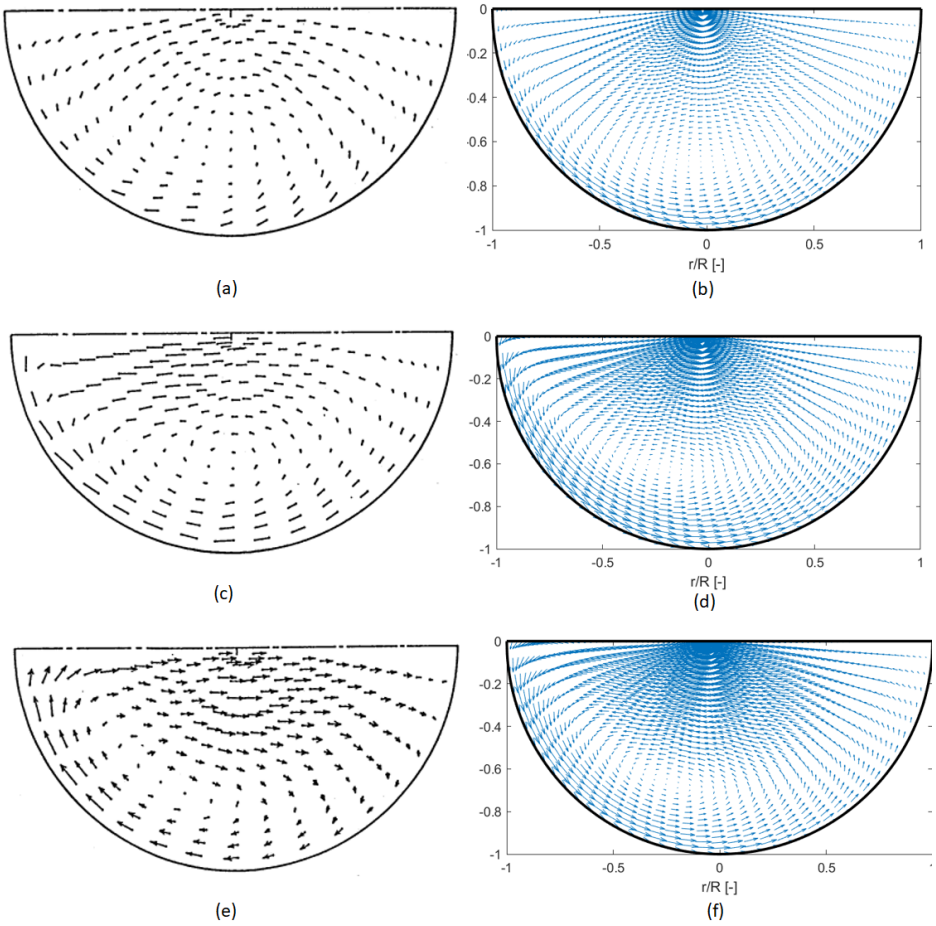

Figure 4.4: The same as Fig. 4.2 for the in-plane velocity vectors.

Finally, the comparison in terms of fluctuating velocity shows the same behaviour already observed in Chapter 3 for the 180° bend. In summary, isotropic, eddy viscosity models do not perform very well on the r_i side of the bend, yielding a strong underestimation of the turbulence level. Note that, in the experiments, the fluctuating axial velocity is reported, whereas, in the CFD simulations, only the $uRMS$ value could be calculated.

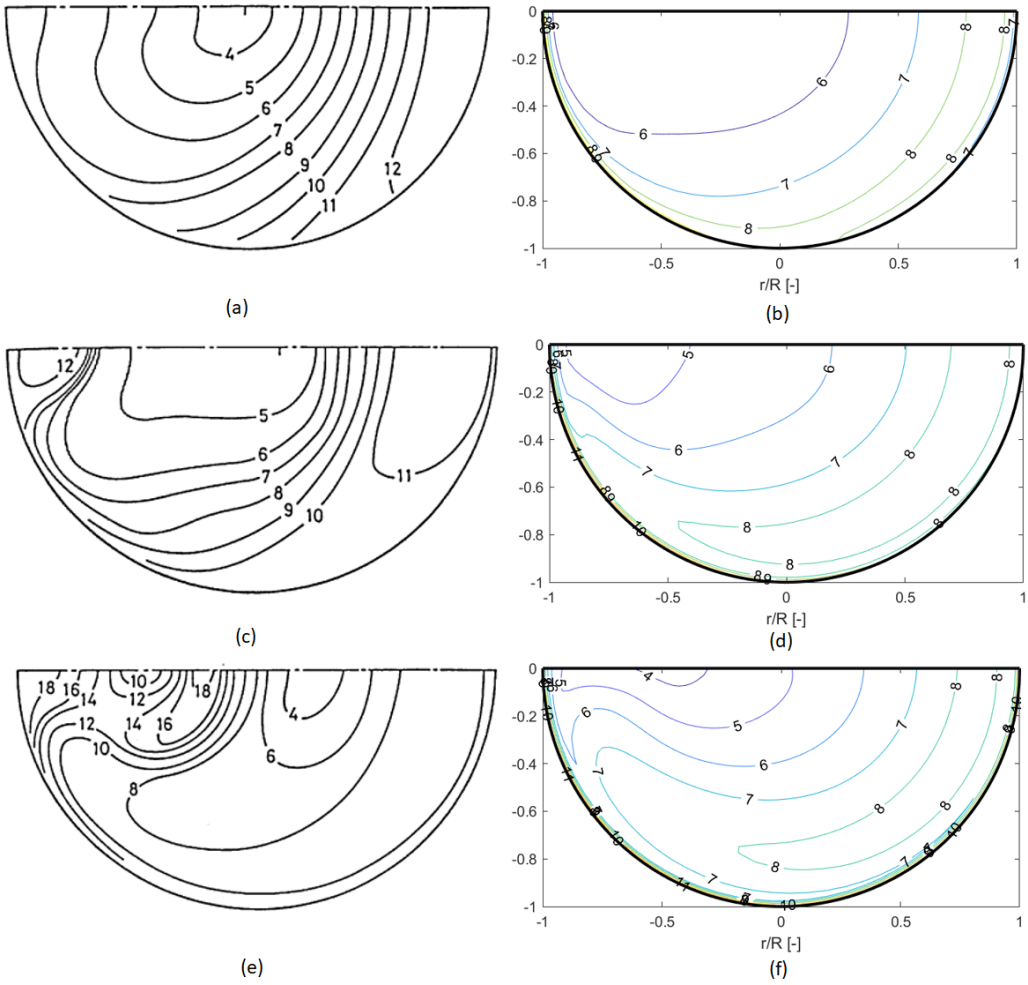

Figure 4.5: The same as Fig. 4.2 for the normalized fluctuating velocity, directly provided by Sudo et al. [8] and estimated as $uRMS/W_b$ in the numerical calculations.

4.2 Numerical simulation of the experiment by Enayet et al. [3]

This paragraph is dedicated to the simulations of the experiments by Enayet et al. [3] summarised in paragraph 1.3.3. Once again, the turbulence model used for these simulations is the RNG $k-\varepsilon$. Unlike Sudo et al. [8] and [9], these authors used water and not air as working fluid. The bend is a $\Phi = 90°$ one, as in the study of Sudo et al. [8], but all the other geometrical parameters are different. In particular, the upstream pipe is only 5D long, and it does not allow the flow to reach a fully developed state.

Due to these differences, a quick mesh sensitivity was carried out by considering two meshes. The flow domain was divided into four parts: "a" is the upstream straight segment pf length 5D, "b" is the 90° bend, "c" includes the first 2D of straight pipe downstream of the bend, and "d" the remaining 8D. Only for the grid sensitivity analysis, parts "c" and "d" were merged together. The characteristic of the different grids are summarised in Tab. 4.2. The power ratio employed in the upstream tangent ("a") was $P = -1.5$ and in the last part was $P = 1.3$. The power ratio were chosen in order avoid abrupt changes in cell size at the interfaces between zone "a" and "b", and between zone "c" and "d", respectively. The sensitivity analysis was carried out by considering the profiles of the variables $uRMS$, pressure, radial velocity and axial velocity along the symmetry diameter in the section at $\varphi = 45°$. As seen in Fig. 4.6, the "Middle-fine Grid" and "Fine Grid" show small differences, and, therefore, it was concluded that the "Middle-fine Grid" would be fine enough to produce accurate results. Nonetheless, since the computational effort isn't too demanding for these types of simulations, all subsequent analyses were carried out using the finer "Final Grid", summarised in Tab. 3.1.

Simulation	**Nθ**	**Nr**	**Na**	**Nb**	**Nc**	**Nd**	**Nz**	**Ntot**	**P.**
Medium-fine grid	30	30	50	90	100		240	216000	-1.5 ; 1.3
Fine grid	40	40	60	120	120		300	480000	-1.5 ; 1.3
Final grid	40	40	60	120	86	96	362	579200	-1.5 ; 1.3

Table 4.2: The three grids employed to reproduce the experiment of Enayet et al. [3]. The meaning of the variables reported in the columns is the same as in Tab. 3.1.

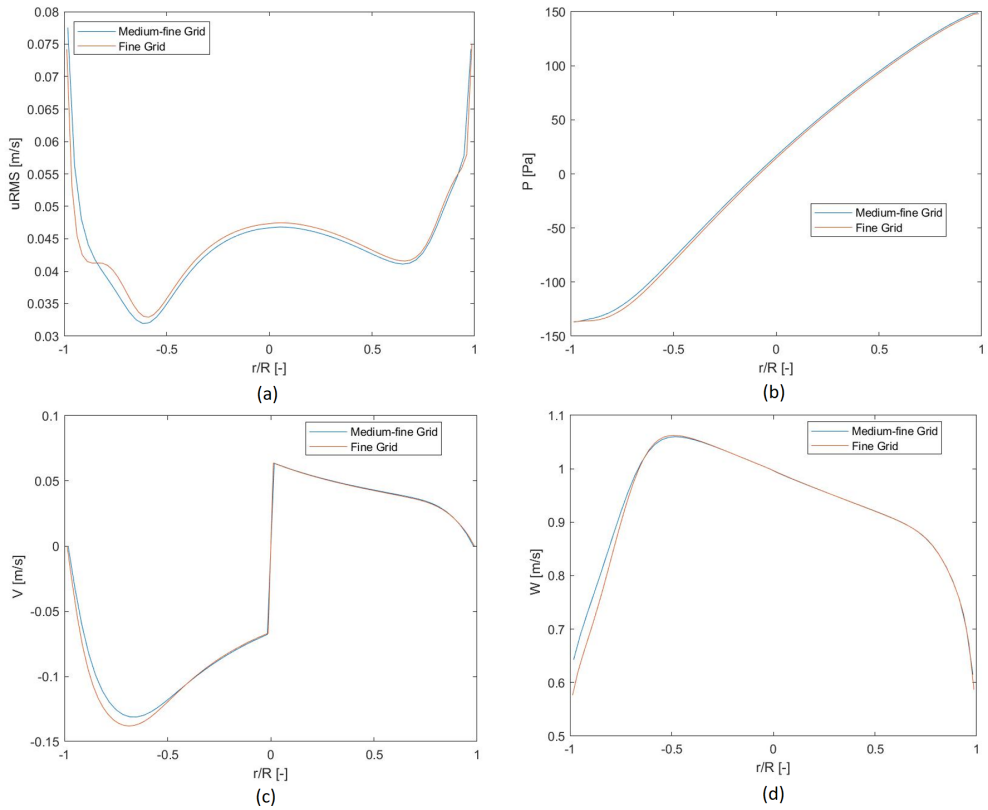

Figure 4.6: Grid sensitivity on the symmetry diameter at $\varphi = 45°$ (Fig.3.11) for the following variables: "a" uRMS ; "b" Pressure ; "c" Radial velocity ; "d" Axial velocity.

Once again, the first non-dimensional parameter used to compare the numerical and experimental data is C_p that is related to the wall static pressure. The trend of C_p along the pipe is considered for three azimuthal angles, individuated by a new reference system visible in the sketch on the bottom left corner of the left graph of Fig. 4.7. In this case, the reference pressure P_{ref} is chosen in order to have perfect superposition between numerical data and experimental data in the point individuated by the coordinates $\theta = 0°$ (reference system in Fig.4.7), $r = R$ and $\varphi = 15°$. The density of water was set to be equal to $\rho_w = 1000\text{Kg/m}^3$ and $W_b = 0.92\text{m/s}$. The agreement between the experimental measurement on the left and numerical prediction is fairly good for the sections inside of the bend. As it happened in the case discussed in paragraph 4.1, the RNG $k - \varepsilon$ models underestimates the pressure loss downstream of the bend.

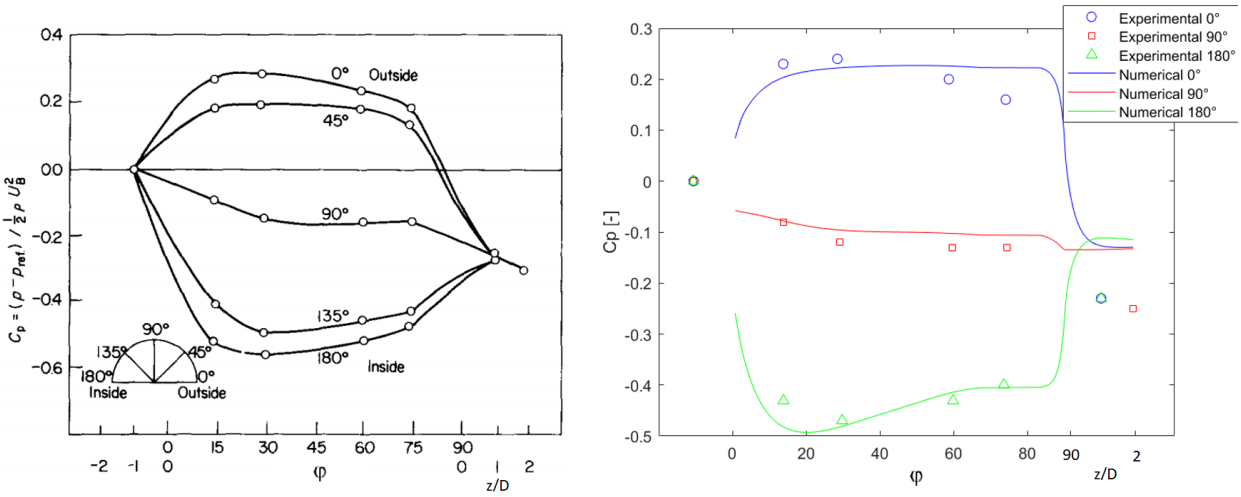

Figure 4.7: Wall static pressure coefficient C_p: experimental data measured by Enayet et al. [3] (left); numerical data with the superposition of experimental data for three azimulthal position (right). The reference system used to identify the azimuthal positions is summarized in bottom left corner of the left plot.

The dimensionless axial velocity is then used to make comparisons between the measurements reported in the paper of Enayet et al. [3] and the simulation results with the RNG $k-\varepsilon$ turbulence model. All pairs of pictures in the same row of Fig. 4.8 show qualitative agreement with each other. The isotaches indicate a peak of W near the inner side of the bend for $\varphi = 30°$ (picture "a" and "b"). Afterwards, because of the secondary flow, the highest axial velocity is drifted towards $r = 0$ (picture "c" and "d") until at $\varphi = 75°$ (picture "e" and "f") show that the pick velocity reached almost the center of the half pipe section. It is interesting to note that this is exactly the same phenomenon described by Sudo et al. [9] [8] in both the $\Phi = 180°$ and the 90° cases. The RNG $k-\varepsilon$ turbulence model underestimates the velocity actually measured by Enayet et al. [3] and the models shows the same flaws previously observed for air flows in pipe bends with different radius and γ.

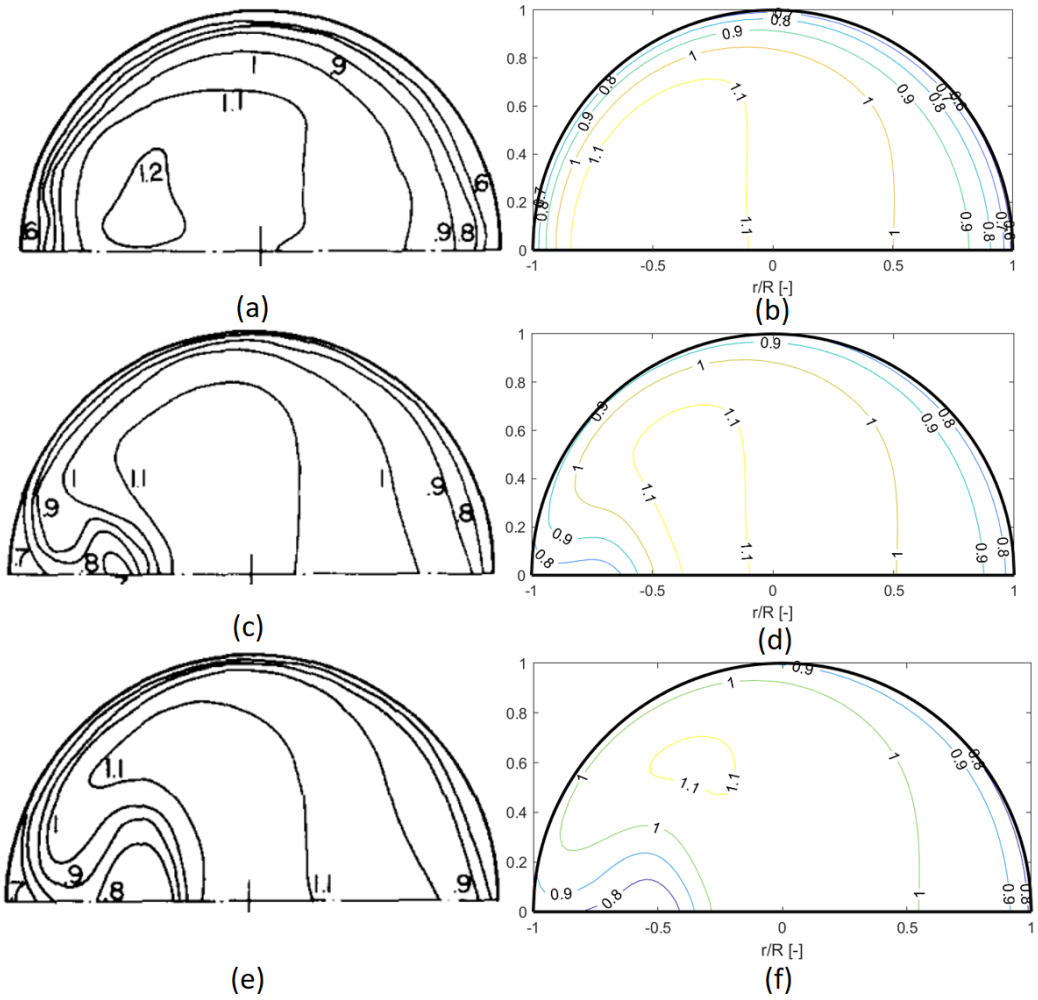

Figure 4.8: Contours of W/W_b over three cross-section of the bend: experimental data measured by Enayet et al [3] (a,c,d) and numerical data (b,d,f). The left sides of each section correspond to the inner wall r_i, and "a" and "b" for section $\varphi = 30°$; "b" and "c" stand for section $\varphi = 60°$; "d" and "e" stand for section $\varphi = 75°$. The left side of each section represent the r_i side of the bend pipe.

In the end, the maps of the normalised fluctuating velocities computed with the PHOENICS are compared those measured by Enayet et al. [3]. Although the plots show some similarities (for instance, in the order ot magnitude of the predictions), in generally, there is a very poor agreement between numerical data and experimental measurements. The disagreement might not to be all attributed to the turbulence model that indeed, as already mentioned, fails in representing the anisotropic turbulent structures inside the bend. In fact, it might be also noticed that Enayet et al. [3] chose to

have an inlet tangent (part "a" of the pipe) of only 5D, and this doesn't allow the flow to be fully developed. The fully developed flow is a state of motion that, for a given flow rate, does not depend on the configuration of the flow at the entrance of the upstream pipe. In these experiments, the length of part "a" is so short that the flow inside the bend is dependent on the inlet condition. In the numerical simulations, the inlet condition in a rectangular velocity distribution with a turbulence intensity of 5%. In the experiments, the fluid dynamic conditions at the entrance of the 5D pipe depend on the configuration of the experimental setup upstream of it, which is unknown. Therefore, it might be reasonably argued that the rectangular shape of the flow variables imposed at the inlet in the numerical simulation might be different from the actual distributions in the experiment carried out by the Enayet et al. [3], contributing to explaining why the agreement is so poor in terms of the turbulence parameters.

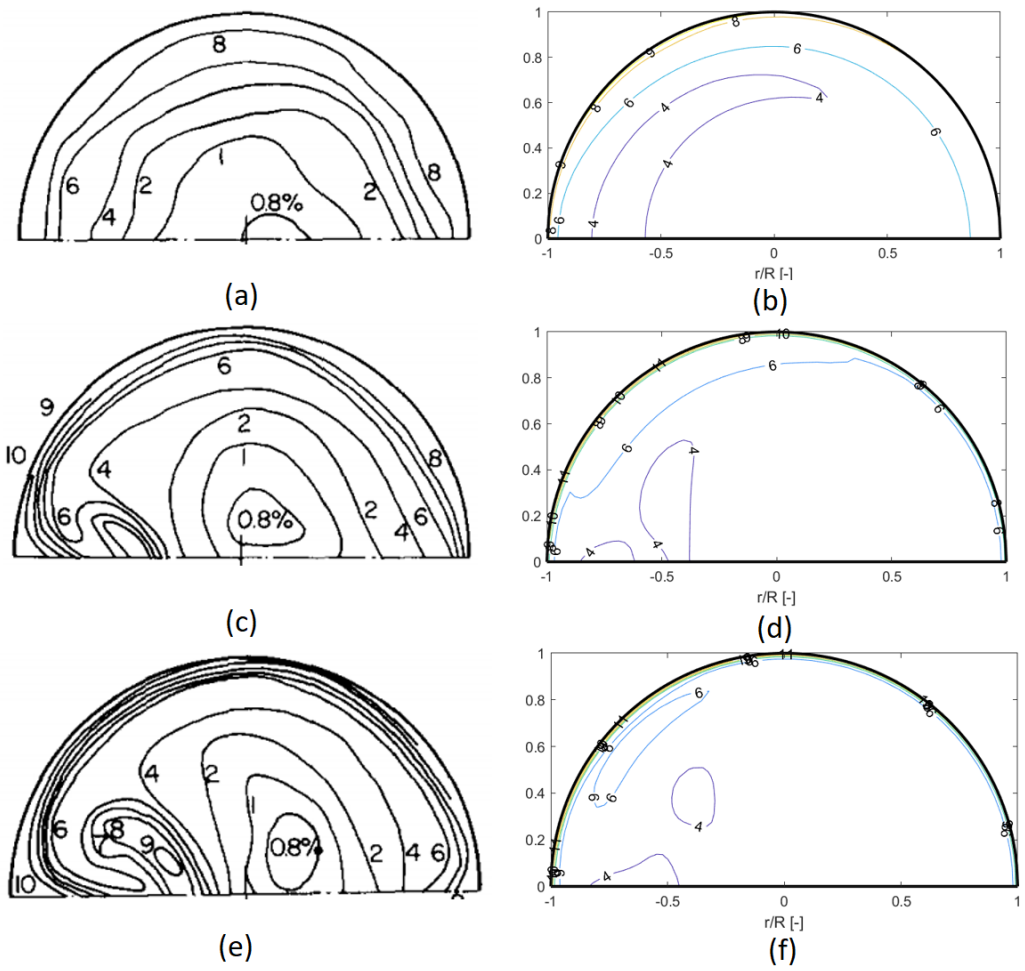

Figure 4.9: The same as Fig. 4.8 for the normalized fluctuating velocity, provided by Enayet et al. [3] (left) and the predicted $uRMS/W_b$ in the numerical simulation (right), > both multiplied by 100.

Conclusions

In order to assess the capability of RANS models based on the eddy viscosity assumption to reproduce the main features of turbulent flows in pipe bends, in this thesis previous numerical and experimental studies have been jointly analyzed and complemented by original simulations with the PHOENICS code.

Five different turbulence models were employed (standard $k-\varepsilon$, RNG $k-\varepsilon$, Relizable $k-\varepsilon$, $k-\omega$, and SST $k-\omega$). All turbulence models, especially the RNG $k-\varepsilon$, reproduced with satisfying degree of accuracy the experimental data in terms of static pressure, longitudinal velocity component, and cross section velocity components.

The study did not only allow providing recommendations for building a suitable CFD model, but it also allowed understading how the characteristics of the turbulent flow inside of a pipe bend. The flow perceives the influence of the bend about one pipe diameter upstream of it, as it was inferred by the fact that, at this location, the longitudinal velocity distribution was no longer axi-symmetrical. At $\varphi = 0°$, the axial velocity starts accelerating towards the inner side of the curve, r_i, due to a very favorable pressure gradient. On the outer side, r_o, the flow is decelerated due to a positive pressure gradient. The imbalance between centrifugal force and lateral pressure gradient force generates an in plane cross-sectional flow which, in the mid plane, is directed from the r_i side to the r_o one. In this context two symmetrical counter rotating vortexes are well visible starting from $\varphi = 30°$ in both the numerical and the experimental data. As a result, the axial momentum is dragged towards the outside of the bend by the secondary flows. For the cases with $\Phi = 90°$, the flow in the exit section of the bend has its pick axial velocity (numerical solution) shifted towards the r_o for the water flow studied by Enalyet et al. [3] as well as for the air flow studied by Sudo et al. [8]. From the experimental and numerical results of the $\Phi = 180°$ case, it can be inferred that the fluid dynamic behaviour of the $\Phi = 90°$ bend qualitatively coincides with

that of the first half of the $\Phi = 180°$ case. Afterwards, for $\varphi = 150° - 180°$, the maximum axial velocity is shifted towards the pipe wall, resulting in a "U" shaped axial velocity profile in the half pipe cross section. This shape is justified by the presence of the secondary flow vortexes that operate together with the centrifugal force.In conclusion if there was a perfect balance between the pressure force and the centrifugal force there would be no secondary flows. The imbalance is created due to a small pressure force, for this reason, there is a secondary flow towards the outside. Furthermore, the outward flow in the median plane is balanced by an inward flow along the wall, so that mass continuity holds.

All eddy-viscosity based turbulence models employed in the thesis are able to reproduce quite well the pressure distribution, quantified through the dimensionless pressure coefficient C_p. The RNG $k - \varepsilon$ showed the best performance in terms axial velocity W, cross-sectional averaged turbulence intensity k_a, and cross-sectional averaged intensity of secondary flows I_s, in addition to the already mentioned wall static pressure coefficient, C_p. At the same time, all these models showed inaccuracies in the modelling of the axial Reynolds stress. This is not surprising, since the behaviour of the turbulence inside of bend is strongly anisotropic. The standard $k - \varepsilon$, RNG $k - \varepsilon$, Relizable $k - \varepsilon$, $k - \omega$, SST $k - \omega$ turbulence model are all based on the eddy viscosity assumption, which requires isotropic turbulence. The advantage of employing the aforementioned turbulence models lies in the relative easiness to a reach convergence with low computational burden. However, the choice was made always being aware, that, on the other hand, these models might be not able to producing accurate representation of the turbulence phenomenon in the bend. It is expected that a turbulence Reynolds stress model, that solves a partial differential equation for each component of the Reynolds stress tensor (6 equations), would be able to better model the turbulent flow in bend pipes, but it might open issues from the numerical point of view. All considered, the performance of eddy viscosity based models, especially the RNG $k-\varepsilon$, could be regarded as satisfactory for many engineering purposes.

This work also highlighted the importance of the use a proper grid in numerical simulation. An accurate choice of the grid can also avoid numerical instability for abrupt changes of mesh size. This was experienced when plotting the I_s at the end of the bend for both numerical solutions of the cases $\Phi = 90°$ $180°$ of Sudo et al. [8] and [9]. On the grounds of the results obtained here by conducting numerical simulations with uniform meshes in the radial and azimutal coordinates, it is possible to argue that improvements might be made by refine the mesh close to the walls to better detect the abrupt

changes of velocity and pressure near the wall, in compliance with the type of near-wall modelling approach adopted. In this work is also stressed the importance of ensuring the fully developed flow upstream of the bend (both in the simulations and in the experiments), in order to make the numerical and laboratory results comparable with each other.

Further developments may be carried out with numerical simulations with other, more complex turbulence models. In particular, the already mentioned Reynolds Stresses Models (RSM), that are expected to be able to provide more accurate representation of the anisotropic turbulent flow inside of pipe bends.

Bibliography

[1] J. Azzola, J. A. Humphrey, H. Lacovides, and B. E. Launder. Developing turbulent flow in a u-bend of circular cross-section: Measurement and computation. *Journal of Fluids Engineering, Transactions of the ASME*, 108(2):214–221, 1986.

[2] J. Blazek and J. Blazek. Chapter 7 – Turbulence Modeling. *Computational Fluid Dynamics: Principles and Applications*, :213 252,2015.

[3] M. M. Enayet, M. M. Gibson, A. M. Taylor, and M. Yianneskis. Laser-Doppler measurements of laminar and turbulent flow in a pipe bend. *International Journal of Heat and Fluid Flow*, 3(4):213–219, 1982.

[4] O.-R. Kalpakli, A. and P. Alfredsson. Dean vortices in turbulent flows: rocking or rolling. *Analysis in Fluids*, 1(1):27, 2011.

[5] A. Kalpakli Vester, R. Orlu, and P. H. Alfredsson. Turbulent flows in curved pipes: Recent advances in experiments and simulations. *Applied Mechanics Reviews*, 68(5), 2016.

[6] D. Kuzmin, O. Mierka, and S. Turek. On the implementation of the k ε turbulence model in incompressible flow solvers based on a finite element discretization.

[7] J. Pruvost, J. Legrand, and P. Legentilhomme. Numerical investigation of bend and torus flows, part I : Effect of swirl motion on flow structure in U-bend. *Chemical Engineering Science*, 59(16):3345–3357, 2004.

[8] K. Sudo, M. Sumida, and H. Hibara. Experimental investigation on turbulent flow in a circular-sectioned 90° bend. *Experiments in Fluids*, 25(1):42–49, 1998.

[9] K. Sudo, M. Sumida, and H. Hibara. Experimental investigation on turbulent flow through a circular-sectioned 180° bend. *Experiments in Fluids*, 28(1):51–57, 2001.

[10] H. K. Versteeg and W. Malalasekera. An Introduction to Computational Fluid Dynamics. 2019.

[11] Y. D. W N Al-Rafai, Tridimas and N. H. Woolley. A study of turbulent flows in pipe bends. 204(9):399–408.

[12] B. A. Wills and J. A. Finch. Modeling and Characterization. *Wills' Mineral Processing Technology.*, ,:449 462,2016.

[13] www.cfd online.com.

[14] www.cham.co.uk.

[15] www.comsol.it.